UNIVERSITÀ DEGLI STUDI DI CAGLIARI

DOTTORATO DI RICERCA IN INGEGNERIA INDUSTRIALE

CICLO XXI

Settore scientifico disciplinare di afferenza: ING-IND/32

PREDICTIVE CONTROL OF ELECTRICAL DRIVES

Presentata da: Ing. Alessandro Serpi

Coordinatore Dottorato: Prof. Ing. Roberto Baratti

Relatore: Prof. Ing. Ignazio Marongiu

Esame finale a.a. 2007/2008

UNIVERSITÀ DEGLI STUDI DI CAGLIARI

DOTTORATO DI RICERCA IN INGEGNERIA INDUSTRIALE

CICLO XXI

PREDICTIVE CONTROL OF ELECTRICAL DRIVES

Supervisor

Prof. Ing. Ignazio Marongiu

PhD Student

Ing. Alessandro Serpi

A Papà e Mamma

INDEX

INTRODUCTION

In the past, the electrical drives control systems were made up of analogical devices, which were affected by some drawbacks, such as high noise sensibility and parameters variations due to thermal effects. Furthermore, the analogical boards, which were generally big and high expensive, could be employed for their specific applications only, without chance of updating and upgrading. Hence, all these features prevented the electrical drives from being widely employed.

In the last thirty years, the control system of the electrical drives have been strongly improved due to the significant development of the electronic devices; in fact, this allows the achievement of digital control systems and sensors, which are smaller and cheaper than the analogical ones. Thus, the analogical boards have been progressively replaced by microprocessor units, which guarantee better performances, low noise sensibility and which can easily reject parameters variations due to thermal effects. Furthermore, since the microprocessor units are generally programmable more than once, the digital control systems can be periodically updated, upgraded or re-employed for different applications. As a consequence, the electrical drives spread in many other fields, being employed, as an example, for household appliances, air conditioning, and for peripherals and computers applications (HDD, CD/DVD drives, printers, etc.).

Therefore, since the microprocessor units are able to perform a lot of calculations in few microseconds, they can be successfully employed in wide bandwidth applications. As a consequence, several control techniques have been developed in order to improve the electrical drives operations, like the predictive control technique (PCT) considered in this work. The PCT, which is based upon the discrete time model of the drives, has been firstly proposed about twenty years ago [1]. It gains more and more interest as much as the elaboration units are improved; in particular, in the last five years, the number of scientific publications on the PCT has been strongly increased.

In this work, it is shown how the employment of the predictive control technique allows the achievement of better performances compared to those obtainable by the traditional control ones. Hence, in Chapter I, a brief analysis of the mathematical model of the drives is reported; moreover, the applicability criteria and the basic equations of the predictive control technique are also introduced. Then, several drives

are considered for the application of the PCT, in particular Brushless DC Drive (Chapter II), Synchronous Reluctance Drive (Chapter III) and Asynchronous Drive (Chapter IV). For each of them, the traditional control strategy is briefly resumed, then predictive control algorithms are developed. In order to highlight the better performances obtainable by the proposed algorithms compared to those achieved by the traditional ones, several simulation studies are carried out by employing the Matlab Simulink environment. In conclusion, all the results obtained are summarized in Chapter V: apart from the advantages in employing the predictive control technique, the most important drawbacks are also taken into account, highlighting the possible future developments and improvements.

I. THE PREDICTIVE CONTROL TECHNIQUE

I.1. Mathematical Models of the Electrical Drives

Regardless of the kind of electrical drive considered, its continuous time model can be expressed, in terms of state variables, as in Eq. (I.1):

$$\frac{d\mathbf{x}}{dt} = \mathbf{A}(\mathbf{x})\cdot\mathbf{x} + \mathbf{B}(\mathbf{x})\cdot\mathbf{u} \tag{I.1}$$

where **x** and **u** are the state and the input vector respectively. Hence, being n and r their corresponding size, Eq. (I.2) can be obtained:

$$\begin{aligned} &\mathbf{x} \in \mathbb{C}^{n\times 1} \quad , \quad \mathbf{u} \in \mathbb{C}^{r\times 1} \\ &\mathbf{A} \in \mathbb{C}^{n\times n} \quad , \quad \mathbf{B} \in \mathbb{C}^{n\times r} \end{aligned} \tag{I.2}$$

The state vector is generally made up of both the electrical and mechanical variables, such as winding currents, magnetic linked fluxes, rotor speed and position, whereas the input vector is constituted by the supply voltages. Moreover, the controlled variables vector **y** can be generally assumed as a function of only **x**, so it can be expressed as in Eq. (I.3):

$$\mathbf{y} = \mathbf{f}(\mathbf{x}) \tag{I.3}$$

Now, being T_s the sampling time, the generic $[kT_s,(k+1)T_s]$ sampling time interval is considered in order to obtain the discrete time model of the drive. However, some assumptions are needed in order to successfully apply the discretization procedure, because the drive is characterized by the non linear continuous time model of Eq. (I.1). First of all, the matrixes **A** and **B** are assumed constant in $[kT_s,(k+1)T_s]$, as in Eq. (I.4):

$$\begin{aligned} &\mathbf{A}(\mathbf{x}) \cong \mathbf{A}(\mathbf{x}_k) = \mathbf{A}_k \\ &\mathbf{B}(\mathbf{x}) \cong \mathbf{B}(\mathbf{x}_k) = \mathbf{B}_k \end{aligned} \quad , \quad t \in \left[kT_s,(k+1)T_s\right] \tag{I.4}$$

This assumption can be made only if the sampling time T_s is chosen sufficiently small compared to the time constants of the system. In this way, Eq. (I.1) becomes:

$$\frac{d\mathbf{x}}{dt} \cong \mathbf{A}_k\cdot\mathbf{x} + \mathbf{B}_k\cdot\mathbf{u} \quad , \quad t \in \left[kT_s,(k+1)T_s\right] \tag{I.5}$$

Its solution **x** can be obtained as the sum of the homogeneous solution $\mathbf{x}_0$ (no input) and of a particular solution $\mathbf{x}_p$ of Eq. (I.5), as shown in Eq. (I.6):

$$\mathbf{x}(t) = \mathbf{x}_0(t) + \mathbf{x}_p(t) \qquad , \qquad t \in \left[kT_s, (k+1)T_s \right] \tag{I.6}$$

Therefore, concerning firstly the homogeneous solution, it can be easily obtained by putting **u** equal to zero in Eq. (I.5):

$$\mathbf{u} = 0 \qquad \rightarrow \qquad \frac{d\mathbf{x}_0}{dt} \cong \mathbf{A}_k \cdot \mathbf{x}_0 \tag{I.7}$$

Therefore, the following Eq. (I.8) is obtained:

$$\mathbf{x}_0(t) = e^{\mathbf{A}_k \cdot (t - kT_s)} \cdot x_k \qquad , \qquad t \in \left[kT_s, (k+1)T_s \right] \tag{I.8}$$

Otherwise, the particular solution $\mathbf{x}_p$ is supposed to be in the following form:

$$\mathbf{x}_p(t) = e^{\mathbf{A}_k \cdot (t - kT_s)} \cdot \varsigma(t) \qquad , \qquad t \in \left[kT_s, (k+1)T_s \right] \tag{I.9}$$

where ς can be determined by substituting Eq. (I.9) in Eq. (I.5):

$$\varsigma(t) = \int_{kT_s}^{t} e^{\mathbf{A}_k \cdot (kT_s - \tau)} \cdot \mathbf{B}_k \cdot \mathbf{u}(\tau) d\tau \qquad , \qquad t \in \left[kT_s, (k+1)T_s \right] \tag{I.10}$$

Therefore, substituting Eq. (I.10) in Eq. (I.9), it becomes:

$$\mathbf{x}_p(t) = \int_{kT_s}^{t} e^{\mathbf{A}_k \cdot (t - \tau)} \cdot \mathbf{B}_k \cdot \mathbf{u}(\tau) d\tau \qquad , \qquad t \in \left[kT_s, (k+1)T_s \right] \tag{I.11}$$

Now, substituting Eq. (I.8) and Eq. (I.11) in Eq. (I.6), Eq. (I.12) is achieved:

$$\mathbf{x}(t) = e^{\mathbf{A}_k \cdot (t - kT_s)} \cdot \mathbf{x}_k + \int_{kT_s}^{t} e^{\mathbf{A}_k \cdot (t - \tau)} \cdot \mathbf{B}_k \cdot \mathbf{u}(\tau) d\tau \quad , \quad t \in \left[kT_s, (k+1)T_s \right] \tag{I.12}$$

So, the state vector value in $(k+1)T_s$ is obtained:

$$\mathbf{x}_{k+1} = \mathbf{F}_k \cdot \mathbf{x}_k + \int_{k \cdot T_s}^{(k+1) \cdot T_s} e^{\mathbf{A}_k \cdot ((k+1) \cdot T_s - \tau)} \cdot \mathbf{B}_k \cdot \mathbf{u}(\tau) d\tau \tag{I.13}$$

being:

$$\mathbf{F}_k = e^{\mathbf{A}_k \cdot T_s} \qquad , \qquad \mathbf{F}_k \in \mathbb{C}^{n \times n} \tag{I.14}$$

Finally, since Eq. (I.3) is usually analytic, the **y** vector value in $(k+1)T_s$ is:

$$\mathbf{y}_{k+1} = \mathbf{f}(\mathbf{x}_{k+1}) \tag{I.15}$$

I.2. The Predictive Control Equations

Referring to the generic $[kT_s,(k+1)T_s]$ sampling time interval, the Predictive Control Technique (PCT) consists in the prediction, in kT_s, of the input signals values which must be applied in order to achieve the reference state values in $(k+1)T_s$. Therefore, since the employment of the PCT requires the computation of the input signals values in each sampling time interval, an explicit solution of Eq. (I.13) must be found. However, to do this, some assumptions on the input signal shape are required. Hence, it can be imposed that each component of the input vector **u** is a rectangular shaped pulse, symmetrically spaced with reference to the middle point of the sampling time interval; in this case, Eq. (I.16) can be achieved:

$$\mathbf{x}_{k+1} = \mathbf{F}_k \cdot \mathbf{x}_k + \mathbf{H}_k \cdot \Delta\mathbf{T}_k \qquad , \qquad \mathbf{H}_k \in \mathbb{C}^{n\times r} \tag{I.16}$$

being:

$$\mathbf{H}_k = e^{\mathbf{A}_k \cdot \frac{T_s}{2}} \cdot \mathbf{B}_k \cdot U \qquad , \qquad U \in \mathbb{C}^{r\times r} \tag{I.17}$$

In particular, $\Delta\mathbf{T}_k$ is the input pulse widths vector, whose components are the equivalent pulses widths of the corresponding input signals. Moreover, U is a diagonal matrix, whose elements are the equivalent magnitudes of the input signals. Now, replacing $\mathbf{x}_{k+1}$ in Eq. (I.16) with its reference value and assuming $\mathbf{H}_k$ as a non singular square matrix, $\Delta\mathbf{T}_k$ can be determined by employing the following Eq. (I.18):

$$\mathbf{x}_{k+1} = \mathbf{x}_{ref} \qquad \rightarrow \qquad \Delta\mathbf{T}_k = \mathbf{H}_k^{-1} \cdot \left(\mathbf{x}_{ref} - \mathbf{F}_k \cdot \mathbf{x}_k\right) \tag{I.18}$$

From the previous equations, it can be noticed that the PCT can be employed only if the discrete time model of the controlled system is well known: in this case, the PCT allows the tracking of the reference values better than the traditional control systems. In particular, when either the voltage saturation or the current limitation constraints occur, the knowledge of the discrete time model of the system allows the achievement of the best performance available: this can be done by employing appropriate predictive algorithms, as pointed out in this work.

Now, in order to demonstrate Eq. (I.16), a scalar real input u is firstly considered. Moreover, since u is assumed like the one depicted in Fig. I.1, it can be defined as in Eq. (I.19):

$$u(t)=\begin{cases}0 & \text{for} \quad t\in[kT_s,t_1]\cup[t_2,(k+1)T_s]\\ U & \text{for} \quad t\in[t_1,t_2]\end{cases} \tag{I.19}$$

Hence, applying Eq. (I.13), Eq. (I.20) is achieved:

$$\mathbf{x}_{k+1}=\mathbf{F}_k\cdot\mathbf{x}_k-e^{\mathbf{A}_k\cdot(k+1)\cdot T_s}\cdot\mathbf{A}_k^{-1}\cdot\left(e^{-\mathbf{A}_k\cdot t_2}-e^{-\mathbf{A}_k\cdot t_1}\right)\cdot\mathbf{B}_k\cdot U \tag{I.20}$$

Now, considering that u is symmetrically spaced with reference to the middle point of the sampling time interval:

$$t_1-k\cdot T_s=(k+1)\cdot T_s-t_2 \quad\rightarrow\quad t_1+t_2=(2k+1)\cdot T_s \tag{I.21}$$

Moreover, the pulse width ΔT_k is defined by the following Eq. (I.22):

$$t_2-t_1=\Delta T_k \tag{I.22}$$

Therefore, t_1 and t_2 can be expressed as follow:

$$t_1=\frac{(2k+1)\cdot T_s-\Delta T_k}{2} \quad , \quad t_2=\frac{(2k+1)\cdot T_s+\Delta T_k}{2} \tag{I.23}$$

Hence, by substituting Eq. (I.23) in Eq. (I.20), Eq. (I.24) is achieved:

$$\mathbf{x}_{k+1}=\mathbf{F}_k\cdot\mathbf{x}_k-e^{\mathbf{A}_k\cdot\frac{T_s}{2}}\cdot\mathbf{A}_k^{-1}\cdot\left(e^{-\mathbf{A}_k\cdot\frac{\Delta T_k}{2}}-e^{\mathbf{A}_k\cdot\frac{\Delta T_k}{2}}\right)\cdot\mathbf{B}_k\cdot U \tag{I.24}$$

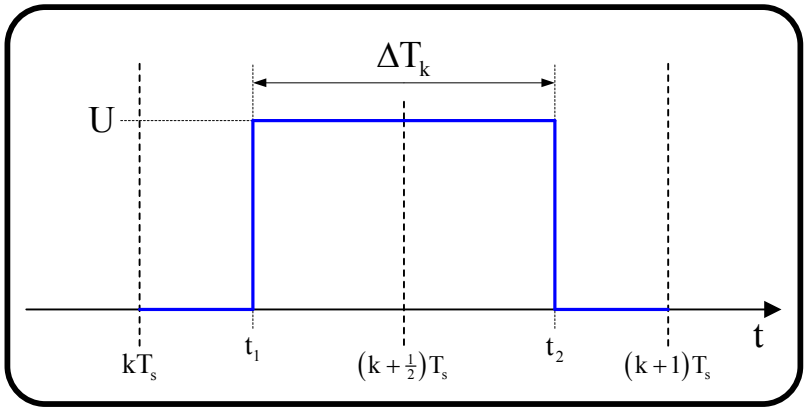

Figure I.1. Real scalar input, made up of a single symmetrical pulse.

Since the pulse width ΔT_k is very small, the following Eq. (I.25) is assumed:

$$e^{\pm \mathbf{A}_k \cdot \frac{\Delta T_k}{2}} \cong 1 \pm \mathbf{A}_k \cdot \frac{\Delta T_k}{2} + \frac{1}{2} \mathbf{A}_k^2 \cdot \left(\frac{\Delta T_k}{2} \right)^2 \tag{I.25}$$

In conclusion, substituting Eq. (I.25) in Eq. (I.24), Eq. (I.16) is achieved.

Now, if the input signal u is not the one depicted in Fig. I.1, but it is still made up of rectangular shaped pulses, symmetrically spaced with reference to the middle point of the sampling time interval, it can be expressed as in Eq. (I.26):

$$u = \sum_i u_i \tag{I.26}$$

where each input signal u_i is a pulse like that depicted in Fig. I.1. Hence, following the same previous procedure, Eq. (I.27) can be achieved:

$$\mathbf{x}_{k+1} = \mathbf{F}_k \cdot \mathbf{x}_k + e^{\mathbf{A}_k \cdot \frac{T_s}{2}} \cdot \mathbf{B}_k \cdot \sum_i \left(U_i \cdot \Delta T_{i,k} \right) \tag{I.27}$$

being U_i and $\Delta T_{i,k}$ the magnitude and the pulse width of the input signal u_i. Therefore, referring to Fig. I.2, Eq. (I.16) can still be applied by introducing the equivalent pulse width ΔT_k and its corresponding magnitude U, which satisfy the following Eq. (I.28):

$$\sum_i \left(U_i \cdot \Delta T_{k,i} \right) = U \cdot \Delta T_k \tag{I.28}$$

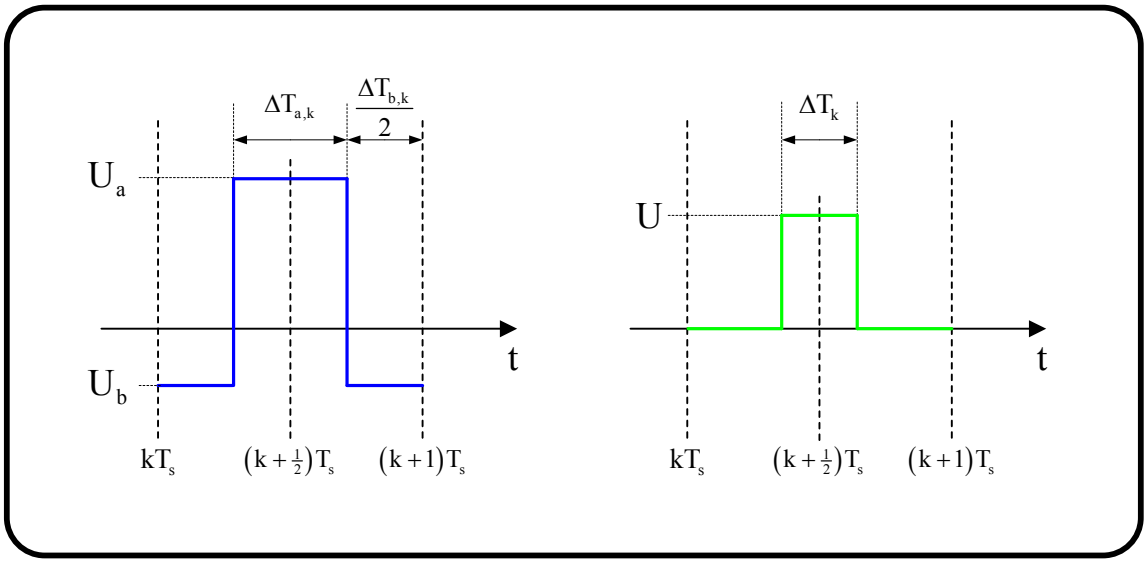

Figure I.2. Symmetrical input signal (on the left) and its equivalent pulse (on the right).

Now, if the input signal **u** is complex, it can be expressed as follow:

$$\mathbf{u}(t) = u_\alpha(t) + j \cdot u_\beta(t) \tag{I.29}$$

Hence, applying the above mentioned procedure, Eq. (I.16) is obtained, being:

$$\mathbf{\Delta T}_k = \Delta T_{\alpha,k} + j \cdot \Delta T_{\beta,k} \tag{I.30}$$

In particular, $\Delta T_{\alpha,k}$ and $\Delta T_{\beta,k}$ are the equivalent pulse widths of u_α and u_β respectively, whereas U is their equivalent magnitude.

Finally, if the input signal **u** is a vector of size r, Eq. (I.13) can be expressed as follow:

$$\mathbf{x}_{k+1} = \mathbf{F}_k \cdot \mathbf{x}_k + \sum_{i=1}^{r} \int_{k \cdot T_s}^{(k+1) \cdot T_s} e^{\mathbf{\Lambda}_k \cdot ((k+1) \cdot T_s - \tau)} \cdot \mathbf{b}_{i,k} \cdot \mathbf{u}_i(\tau) d\tau \tag{I.31}$$

where $\mathbf{b}_{i,k}$ is the column i of the matrix $\mathbf{B}_k$ and $\mathbf{u}_i$ is the corresponding input vector component. Therefore, applying the same procedure previously employed, the following Eq. (I.32) is obtained:

$$\mathbf{x}_{k+1} = \mathbf{F}_k \cdot \mathbf{x}_k + \sum_{i=1}^{r} \left(\mathbf{h}_{i,k} \cdot \mathbf{\Delta T}_{i,k} \right) \tag{I.32}$$

being:

$$\mathbf{h}_{i,k} = e^{\mathbf{\Lambda}_k \cdot \frac{T_s}{2}} \cdot \mathbf{b}_{i,k} \cdot U_i \tag{I.33}$$

Since $\mathbf{\Delta T}_{i,k}$ and U_i are respectively the equivalent pulse width and the magnitude of $\mathbf{u}_i$, Eq. (I.16) is still applicable, being the matrixes $\mathbf{H}_k$ and U those defined by Eq. (I.34):

$$\mathbf{H}_k = \left[\mathbf{h}_{1,k}, \mathbf{h}_{2,k}, ..., \mathbf{h}_{r,k} \right] \quad , \quad U = \text{diag}\left\{ U_1, U_2, ..., U_r \right\} \tag{I.34}$$

Summarizing, it has been just demonstrated that if the input vector **u** of Eq. (I.13) is made up of rectangular shaped pulses, symmetrical with reference to the middle point of the sampling time interval, Eq. (I.16) can be assumed. Considering the mathematical models of the electrical drives, **u** corresponds to the supply voltages, so it is generally possible to realize each input vector component $\mathbf{u}_i$ as required. Nevertheless, when the continuous mathematical model of the drive is referred to the rotor reference frame, Eq. (I.13) becomes:

$$\mathbf{x}_{k+1}^{(r)} = \mathbf{F}_k \cdot \mathbf{x}_k^{(r)} + \int_{k \cdot T_s}^{(k+1) \cdot T_s} e^{\mathbf{\Lambda}_k \cdot ((k+1) \cdot T_s - \tau)} \cdot \mathbf{B}_k \cdot \mathbf{u}^{(r)}(\tau) d\tau \tag{I.35}$$

Therefore, $\mathbf{u}^{(r)}$ does not generally satisfy the required condition because it depends on the rotor position, as in Eq. (I.36):

$$\mathbf{u}^{(r)}(t) = \mathbf{u}^{(s)}(t) \cdot e^{-j\cdot\theta(t)} \tag{I.36}$$

being $\mathbf{u}^{(s)}$ the input space vector referred to the stator reference frame. In fact, also if $\mathbf{u}^{(s)}$ is made up of rectangular shaped pulses, symmetrical with reference to the middle point of the sampling time interval, $\mathbf{u}^{(r)}$ can satisfy the same condition only if θ is constant over each sampling time interval. However, Eq. (I.16) can still be employed on condition that:

$$\theta(t) = \theta_k + \omega_k \cdot (t - kT_s) \qquad , \qquad t \in \left[kT_s, (k+1)T_s\right] \tag{I.37}$$

where θ_k and ω_k must be assumed constant over each sampling time interval. To prove this, it is firstly necessary to substitute Eq. (I.36) in Eq. (I.35), obtaining the following Eq. (I.38):

$$\mathbf{x}_{k+1}^{(r)} = \mathbf{F}_k \cdot \mathbf{x}_k^{(r)} + \int_{k\cdot T_s}^{(k+1)\cdot T_s} e^{\mathbf{A}_k\cdot((k+1)\cdot T_s - \tau)} \cdot e^{-j\cdot\theta(\tau)} \cdot \mathbf{B}_k \cdot \mathbf{u}^{(s)}(\tau)\, d\tau \tag{I.38}$$

Furthermore, by substituting Eq. (I.37) in Eq. (I.38), it becomes:

$$\mathbf{x}_{k+1}^{(r)} = \mathbf{F}_k \cdot \mathbf{x}_k^{(r)} + e^{-j\cdot\theta_{k+1}} \cdot \int_{k\cdot T_s}^{(k+1)\cdot T_s} e^{\tilde{\mathbf{A}}_k\cdot((k+1)\cdot T_s - \tau)} \cdot \mathbf{B}_k \cdot \mathbf{u}^{(s)}(\tau)\, d\tau \tag{I.39}$$

being:

$$\tilde{\mathbf{A}}_k = \mathbf{A}_k + j\cdot\omega_k \cdot I_A \tag{I.40}$$

Moreover, I_A is the identity matrix of the same size of $\mathbf{A}_k$. Therefore, Eq. (I.39) can be solved by employing the usually procedure, obtaining the following result:

$$\mathbf{x}_{k+1} = \mathbf{F}_k \cdot \mathbf{x}_k + e^{-j\cdot\theta_{k+1}} \cdot e^{\tilde{\mathbf{A}}_k \cdot \frac{T_s}{2}} \cdot \mathbf{B}_k \cdot U \cdot \Delta\mathbf{T}_k^{(s)} \tag{I.41}$$

Therefore, substituting Eq. (I.40) in Eq. (I.41), Eq. (I.42) is achieved:

$$\mathbf{x}_{k+1} = \mathbf{F}_k \cdot \mathbf{x}_k + \mathbf{H}_k \cdot \left(\Delta\mathbf{T}_k^{(s)} \cdot e^{-j\cdot\hat{\theta}_k}\right) \tag{I.42}$$

being:

$$\hat{\theta}_k = \theta_{k+\frac{1}{2}} = \theta_k + \omega_k \cdot \frac{T_s}{2} \tag{I.43}$$

In conclusion, Eq. (I.16) is still valid if the rotor-to-stator and stator-to-rotor space vector transformations of $\mathbf{\Delta T}_k$ are performed using the middle value of θ in the sampling time interval, as in Eq. (I.44):

$$\mathbf{\Delta T}_k^{(r)} = \mathbf{\Delta T}_k^{(s)} \cdot e^{-j\cdot\bar{\theta}_k} \tag{I.44}$$

II. BRUSHLESS DC DRIVE

II.1. Introduction

Brushless DC drive makes use of a low resolution and cheap position detector by means of which the phases are properly commutated. However, it is affected by the well known current commutation phenomena, which generally gives rise to current and torque ripple. In particular, at low speed operation, this occurs if the voltages impressed under current commutation are not properly determined. Otherwise, at high speed operation, the induced emfs are so high that the DC bus voltage cannot force the currents during commutation as required, determining, current dips. Moreover, even if perfect commutation is performed, the corresponding emf variation of the leaving phase is not negligible, leading to strong current and torque ripples and, consequently, to a reduction of the mean torque value.

The current commutation phenomena has been investigated by a long time [2] and several solutions have been proposed. As a result, current commutation has been improved by employing an appropriate PWM modulation of the supplying inverter, as in [3], where the current of non-commutating phase is imposed constant during each current commutation by properly using three current control loops. Thus, the drive performance has been improved and, nowadays, it can be successfully employed also in high performance applications. However, in the papers concerning the commutation phenomena, the winding resistances are usually neglected and the induced emfs are assumed constant during each current commutation, not taking into account the variation of the rotor position. This last assumption can be generally assumed at low speed operation because the current commutation is fast compared to the variation of the rotor position. Otherwise, at high speed operation, since the current commutation becomes quite slow and the rotor position varies faster than before, its variation should not be neglected further. In fact, even if a perfect commutation is performed, the torque ripple occurs due to the emfs variation. In [4], the current commutation compensation is imposed by an appropriate modulation technique, both at low and high speed operation. However, also in this recent contribution, the torque ripple due to the emfs variation has not been considered. In [5], the emfs variation is taken into

account but no proposal has been made in order to mitigate the corresponding torque ripple.

In this work, the employment of the predictive control technique is proposed. First of all, a predictive control algorithm is developed with the aim of improving the traditional current commutation as best as possible. Secondly, a novel predictive control algorithm is proposed in order to globally improve the drive performances: in fact, it is deduced imposing the achievement of both the reference torque value and the minimum Joule losses condition at every speed operation. Thus, a computer simulation study is conducted with the aim of comparing the performance of the drive controlled by the propose predictive algorithm with that obtained by employing the traditional control strategy.

II.2. The continuous time model

The Brushless DC machine is characterized by the particular shape of its emfs, which are depicted in Fig. II.1. Hence, it is useful to define the indexes {x,y,z}, which represent alternatively the three phases of the stator winding in each of the six sectors, as shown in Fig. II.1 too. In fact, in this way, it is possible to get the mathematical model of the drive referring to only one of the six sectors. Furthermore, being, a new variable θ_{pu} is introduced, as in the following Eq. (II.1):

$$\theta_{pu} = \left(\theta + \frac{\pi}{6}\right) \,\%\, \frac{\pi}{3} \quad , \quad \theta = p \cdot \theta_m \quad , \quad \theta_{pu} \in [0,1) \tag{II.1}$$

being % the mod operator, θ_m the rotor position and p the pole pairs. Thus, the electrical equation of the drive is obtained, as in Eq. (II.2):

$$v_{ph} = r \cdot i_{ph} + L \cdot \frac{di_{ph}}{dt} + e_{ph} \tag{II.2}$$

where r is the phase resistance and L is the equivalent inductance, whereas i_{ph}, v_{ph} and e_{ph} are the current, voltage and emf phase vector respectively, all defined by the following Eq. (II.3):

$$v_{ph} = \begin{bmatrix} v_x \\ v_y \\ v_z \end{bmatrix} \quad , \quad i_{ph} = \begin{bmatrix} i_x \\ i_y \\ i_z \end{bmatrix} \quad , \quad e_{ph} = \begin{bmatrix} e_x \\ e_y \\ e_z \end{bmatrix} = \pm E \cdot \begin{bmatrix} 1 \\ -1 \\ 1 - 2\theta_{pu} \end{bmatrix} \tag{II.3}$$

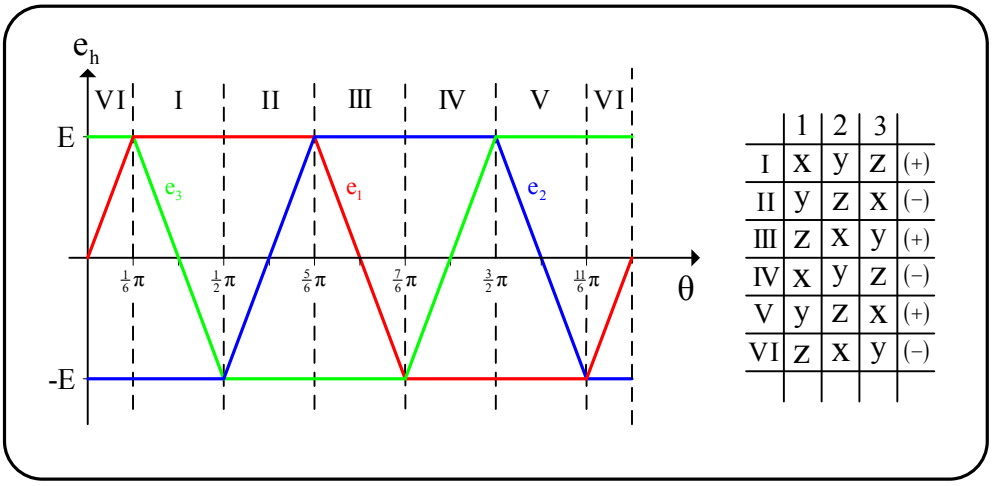

	1	2	3	
I	x	y	z	(+)
II	y	z	x	(−)
III	z	x	y	(+)
IV	x	y	z	(−)
V	y	z	x	(+)
VI	z	x	y	(−)

Figure II.1. Emfs shape an the relation between {x,y,z} and {1,2,3} in the six sectors.

Now, by multiplying both terms of Eq. (II.2) by the transpose i_{ph} vector, the power balance can be achieved. Thus, electrical power converted into the mechanical one is expressed as:

$$\mathcal{P}_m = e_{ph} \cdot i_{ph}^T \tag{II.4}$$

However, being ω_m the rotor speed, $\mathcal{P}_m$ can be also expressed as in Eq. (II.5):

$$\mathcal{P}_m = T_e \cdot \omega_m \tag{II.5}$$

Therefore, the electromagnetic torque is expressed as in Eq. (II.6):

$$T_e = \frac{e_{ph} \cdot i_{ph}^T}{\omega_m} = \frac{1}{\omega_m} \cdot \sum_h e_h \cdot i_h \tag{II.6}$$

Furthermore, by substituting Eq. (II.3) in Eq. (II.6), the following result can be achieved:

$$T_e = \pm p\Lambda \cdot \left(i_x - i_y + \left(1 - 2\theta_{pu}\right) \cdot i_z \right) \quad , \quad \Lambda = \frac{E}{\omega} = \frac{E}{p \cdot \omega_m} \tag{II.7}$$

Finally, the mechanical equations of the motor are:

$$\begin{aligned} T_e &= D_m \cdot \omega_m + J_m \cdot \frac{d\omega_m}{dt} + T_{load} \\ \omega_m &= \frac{d\theta_m}{dt} \end{aligned} \tag{II.8}$$

being J_m the rotor inertia, D_m the damping factor and T_{load} the load torque.

Summarizing, the continuous time model of the motor is defined by Eq. (II.2), (II.7) and (II.8), in which the state variables are the phase currents $\{i_x, i_y, i_z\}$, the rotor speed ω_m and its position θ_m. However, Eq. (II.2) and Eq. (II.7) can be replaced by the following Eq. (II.9) and Eq. (II.10) respectively:

$$v_{ch} = r \cdot i_{ch} + L \cdot \frac{di_{ch}}{dt} + e_{ch} \tag{II.9}$$

$$T_e = \pm \frac{2}{3} p\Lambda \cdot \left(i_{xy} - \left(1 - \theta_{pu}\right) \cdot i_{yz} - \theta_{pu} \cdot i_{zx} \right) \tag{II.10}$$

These last equations are expressed by using the chain currents $\{i_{xy},i_{yz},i_{zx}\}$ instead of the phase ones, being:

$$v_{ch}=\begin{bmatrix} v_{xy} \\ v_{yz} \\ v_{zx} \end{bmatrix} \quad , \quad i_{ch}=\begin{bmatrix} i_{xy} \\ i_{yz} \\ i_{zx} \end{bmatrix} \quad , \quad e_{ch}=\begin{bmatrix} e_{xy} \\ e_{yz} \\ e_{zx} \end{bmatrix} = \pm\, 2E \cdot \begin{bmatrix} 1 \\ -\left(1-\theta_{pu}\right) \\ -\theta_{pu} \end{bmatrix} \qquad \text{(II.11)}$$

II.3. Control Strategies

The traditional control strategy employed for the Brushless DC drive consists in achieving the following reference currents values:

$$i_{ph}^{(ref)} = \pm \begin{bmatrix} \mathcal{I} \\ -\mathcal{I} \\ 0 \end{bmatrix} \quad \rightarrow \quad i_{ch}^{(ref)} = \pm \begin{bmatrix} 2\mathcal{I} \\ -\mathcal{I} \\ -\mathcal{I} \end{bmatrix} \tag{II.12}$$

Therefore, substituting Eq. (II.12) in Eq. (II.7) or in Eq. (II.10), the reference torque value is obtained:

$$T_e^{(ref)} = p\Lambda \cdot 2\mathcal{I} \tag{II.13}$$

Hence, referring to Fig. II.2 and II.3, when a change of sector occurs, the currents must be forced to reach their reference values, in accordance with the relation between {x,y,z} and {1,2,3} reported in Fig. II.1. So, during each current commutation, the traditional algorithm keeps i_y constant by properly varying i_x and i_z, as shown in Fig. II.2, although this solution cannot assure constant torque value. In fact, being $\{\Delta i_x, \Delta i_y, \Delta i_z\}$ the currents variations imposed by the traditional control algorithm during current commutation, they can be expressed as in Eq. (II.14):

$$\begin{aligned} \Delta i_x &= -\Delta i_z = \Delta i \\ \Delta i_y &= 0 \end{aligned} \tag{II.14}$$

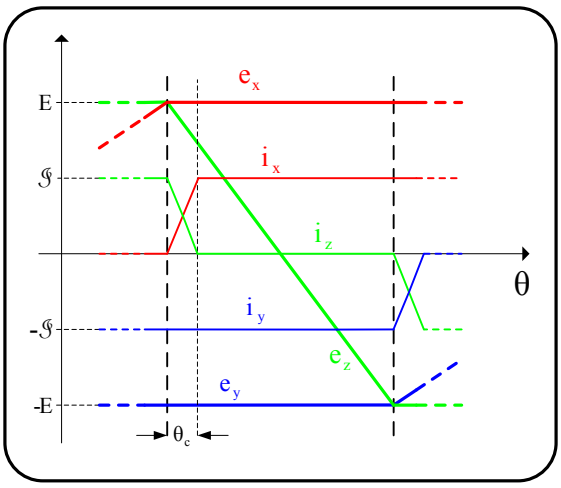

Figure II.2. Phase currents achieved by the traditional control strategy.

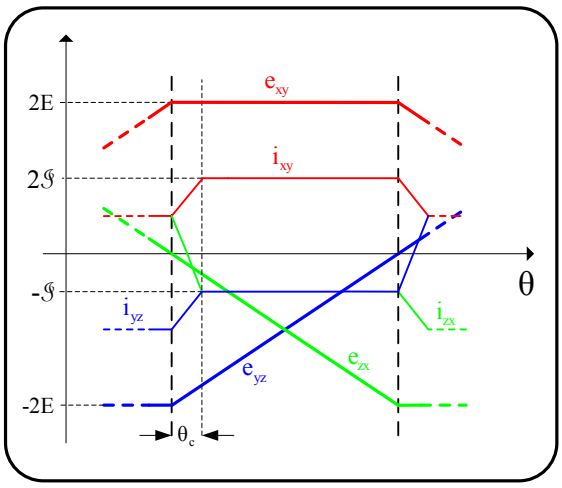

Figure II.3. Chain currents achieved by the traditional control strategy.

Thus, the corresponding torque variation ΔT_e is:

$$\Delta T_e = \pm 2p\Lambda \cdot \left(\Delta i \cdot \theta_{pu} - \left(i_z - \Delta i \right) \cdot \Delta\theta_{pu} \right) \tag{II.15}$$

Therefore, ΔT_e is zero only if the following constraint is verified:

$$\Delta i \cdot \theta_{pu} - \left(i_z - \Delta i \right) \cdot \Delta\theta_{pu} = 0 \tag{II.16}$$

At low speed operation, since it can be assumed that:

$$\theta_{pu} \cong 0 \qquad , \qquad \Delta\theta_{pu} \cong 0 \tag{II.17}$$

the performances achieved by the traditional control strategy are acceptable. Otherwise, at high speed operation, Eq. (II.17) cannot be assumed further, so the traditional control strategy does not guarantee that the torque can be kept constant during each current commutation.

This drawback can be overcome by employing the novel control strategy proposed in this work; it consists in determining new currents reference values by imposing the following constraints:

$$\pm p\Lambda \cdot \left(i_x^{(ref)} - i_y^{(ref)} + \left(1 - 2\theta_{pu} \right) \cdot i_z^{(ref)} \right) = T_e^{(ref)} \tag{II.18}$$

$$\mathcal{F}\left(i_{ph}^{(ref)} \right) = \left(i_x^{(ref)} \right)^2 + \left(i_y^{(ref)} \right)^2 + \left(i_z^{(ref)} \right)^2 = \min_{i_x, i_y, i_z} \left\{ \sum_{h=x,y,z} i_h^2 \right\} \tag{II.19}$$

In particular, Eq. (II.18) imposes the achievement of the reference torque value, whereas Eq. (II.19) requires that the currents reference values must be chosen in order to minimize the Joule losses. Hence, since:

$$i_x^{(ref)} + i_y^{(ref)} + i_z^{(ref)} = 0 \tag{II.20}$$

by combining Eq. (II.18) with Eq. (II.20), the following results can be obtained:

$$\begin{aligned} i_x^{(ref)} &= -\left(1 - \theta_{pu} \right) \cdot i_z^{(ref)} \pm \frac{T_e^{(ref)}}{2p\Lambda} \\ i_y^{(ref)} &= -\theta_{pu} \cdot i_z^{(ref)} \mp \frac{T_e^{(ref)}}{2p\Lambda} \end{aligned} \tag{II.21}$$

Hence, substituting Eq. (II.21) in Eq. (II.19), Eq. (II.22) is achieved:

$$\mathcal{F}\left(i_z^{(ref)}\right) = 2\left(1-\theta_{pu}+\theta_{pu}^2\right)\cdot\left(i_z^{(ref)}\right)^2 \mp 2\left(1-2\theta_{pu}\right)\frac{T_e^{(ref)}}{2p\Lambda}\cdot i_z^{(ref)} + 2\left(\frac{T_e^{(ref)}}{2p\Lambda}\right)^2 \tag{II.22}$$

Now, since:

$$\forall\theta_{pu}\in[0,1) \qquad \rightarrow \qquad 1-\theta_{pu}+\theta_{pu}^2 \geq 0 \tag{II.23}$$

Eq. (II.19) is satisfied if $i_z^{(ref)}$ is chosen as in Eq. (II.24):

$$i_z^{(ref)} = \pm\frac{1-2\theta_{pu}}{\left(1-\theta_{pu}+\theta_{pu}^2\right)}\cdot\frac{T_e^{(ref)}}{4p\Lambda} \tag{II.24}$$

In this way, Eq. (II.22) becomes:

$$\mathcal{F}\left(i_z^{(ref)}\right) = \frac{3}{2}\cdot\left(\frac{T_e^{(ref)}}{2p\Lambda}\right)^2\cdot\frac{1}{\left(1-\theta_{pu}+\theta_{pu}^2\right)} \tag{II.25}$$

Moreover, substituting Eq. (II.24) in Eq. (II.21), the other current reference values can be easily achieved:

$$\begin{aligned} i_x^{(ref)} &= \pm\frac{1+\theta_{pu}}{\left(1-\theta_{pu}+\theta_{pu}^2\right)}\cdot\frac{T_e^{(ref)}}{4p\Lambda} \\ i_y^{(ref)} &= \mp\frac{2-\theta_{pu}}{\left(1-\theta_{pu}+\theta_{pu}^2\right)}\cdot\frac{T_e^{(ref)}}{4p\Lambda} \end{aligned} \tag{II.26}$$

Consequently, from Eq. (II.24) and Eq. (II.26), the $i_{ph}^{(ref)}$ and the $i_{ch}^{(ref)}$ vectors can be easily obtained, as in Eq. (II.27) and in Eq. (II.28):

$$i_{ph}^{(ref)} = \pm\frac{\mathcal{I}}{2}\cdot\frac{1}{\left(1-\theta_{pu}+\theta_{pu}^2\right)}\begin{bmatrix} 1+\theta_{pu} \\ -\left(2-\theta_{pu}\right) \\ 1-2\theta_{pu} \end{bmatrix} \tag{II.27}$$

$$i_{ch}^{(ref)} = \pm\frac{3\mathcal{I}}{2}\cdot\frac{1}{\left(1-\theta_{pu}+\theta_{pu}^2\right)}\begin{bmatrix} 1 \\ -\left(1-\theta_{pu}\right) \\ -\theta_{pu} \end{bmatrix} \tag{II.28}$$

being $\mathcal{I}$ the same reference current value employed in Eq. (II.12) and in Eq. (II.13).

The new reference phase currents signals and the corresponding chain ones are depicted in Fig. II.4 and II.5 respectively. The corresponding mean Joule losses can be expressed as in the following Eq. (II.29):

$$\widetilde{\mathcal{P}}_J = r \cdot \int_0^1 \mathcal{F}\left(i_z^{(ref)}\right) d\theta_{pu} = r \cdot \frac{\pi}{\sqrt{3}} \cdot \left(\frac{T_e^{(ref)}}{2p\Lambda}\right)^2 = \frac{\pi}{\sqrt{3}} \cdot r \cdot \mathcal{I}^2 \qquad \text{(II.29)}$$

Therefore, by employing the proposed reference currents signals, the mean Joule losses can be reduced to about 90.7 % of the ones obtained by the traditional control strategy, which are expressed as in Eq. (II.30):

$$\widetilde{\mathcal{P}}_J = 2 \cdot r \cdot \mathcal{I}^2 \qquad \text{(II.30)}$$

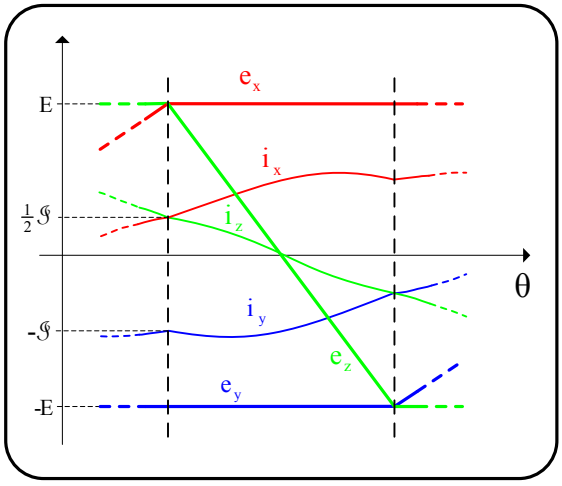

Figure II.4. Phase currents achieved by the proposed control strategy.

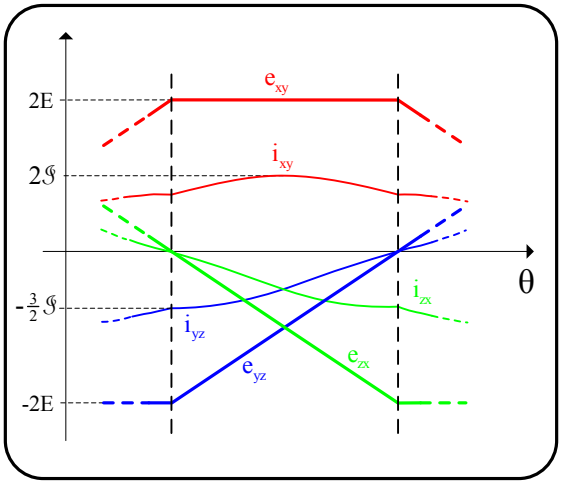

Figure II.5. Chain currents achieved by the proposed control strategy.

II.4. The discrete time model

In order to determine the discrete time model of the Brushless DC drive, Eq. (II.2) cannot be employed due to the emfs shape, which prevents the phase voltages to be made up of symmetrical pulses, as required. However, this drawback can be successfully overcome by employing Eq. (II.9) in place of Eq. (II.2); in fact, the chain voltages are not affected by the emfs shape, so the discretization procedure can be successfully performed. Moreover, only Eq. (II.9) and Eq. (II.10) are considered; in fact, the sampling time T_s is chosen sufficiently small so that the rotor speed ω_m can be assumed constant in each sampling time interval, equal to $\omega_{m,k}$. As a consequence, referring to the generic $[kT_s,(k+1)T_s]$ sampling time interval, θ_{pu} can be expressed by the following Eq. (II.31):

$$\theta_{pu}(t) = \left(\theta_{pu,k} + \omega_{pu,k} \cdot (t - kT_s)\right) \;\%\; 1 \qquad \text{(II.31)}$$

being % the mod operator and:

$$\theta_{pu,k} = \frac{3\theta_k}{\pi} + \frac{1}{2} \quad , \quad \omega_{pu,k} = \frac{3\omega_k}{\pi} \qquad \text{(II.32)}$$

Furthermore, it is necessary to determine the commutation instant $\mathcal{T}_k$, in correspondence of which the next change of sector occurs. Hence, considering Eq. (II.31), this time value can easily be computed as follow:

$$\theta_{pu,k} + \omega_{pu,k} \cdot (\mathcal{T}_k - kT_s) = 1 \quad \rightarrow \quad \mathcal{T}_k = kT_s + \frac{1 - \theta_{pu,k}}{\omega_{pu,k}} \qquad \text{(II.33)}$$

However, since all the $\mathcal{T}_k$ values bigger than $(k+1)T_s$ mean that the next commutation instant does not belong to $[kT_s,(k+1)T_s]$, it is more useful to define $\mathcal{T}_k$ as in Eq. (II.34):

$$\mathcal{T}_k = \min\left\{kT_s + \frac{1 - \theta_{pu,k}}{\omega_{pu,k}}, (k+1)T_s\right\} \qquad \text{(II.34)}$$

and, in per unit, as in the following Eq. (II.35):

$$\mathcal{T}_{pu,k} = \frac{\mathcal{T}_k - kT_s}{T_s} = \min\left\{\frac{1 - \theta_{pu,k}}{\omega_{pu,k} T_s},\ 1\right\} \qquad \text{(II.35)}$$

Thus, always referring to $[kT_s,(k+1)T_s]$, if $\mathfrak{I}_{pu,k}$ is bigger than one, e_{ch} and θ_{pu} are well defined by Eq. (II.36):

$$e_{ch}^{(-)} = \pm\, 2E \cdot \begin{bmatrix} 1 \\ -\left(1-\theta_{pu}^{(-)}\right) \\ -\theta_{pu}^{(-)} \end{bmatrix} \quad , \quad \theta_{pu}^{(-)}(t) = \theta_{pu,k} + \omega_{pu,k} \cdot \delta_{-2}\left(t - kT_s\right) \tag{II.36}$$

where $^{(-)}$ denotes that the variables are evaluated before the next commutation instant, being:

$$\delta_{-2}\left(t - kT_s\right) = t - kT_s \qquad \left(t \geq kT_s\right) \tag{II.37}$$

Otherwise, if $\mathfrak{I}_{pu,k}$ is less than one, as shown in Fig. II.6 and in Fig. II.7, Eq. (II.36) can be applied only before $\mathfrak{I}_k$. In fact, after that, it must be replaced by Eq. (II.38):

$$e_{ch}^{(+)} = \pm\, 2E \cdot \begin{bmatrix} \left(1-\theta_{pu}^{(+)}\right) \\ \theta_{pu}^{(+)} \\ -1 \end{bmatrix} \quad , \quad \theta_{pu}^{(+)}(t) = \omega_{pu,k} \cdot \delta_{-2}\left(t - \mathfrak{I}_k\right) \tag{II.38}$$

where $^{(+)}$ denotes that these variables are evaluated after the commutation instant. Therefore, taking into account both these situations, the e_{ch} vector can be expressed as in Eq. (II.39):

$$e_{ch} = e_{ch,k} + \Delta e_{ch,k} \tag{II.39}$$

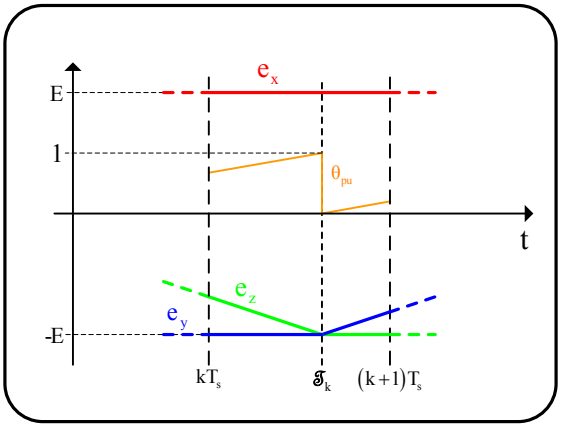

Figure II.6. e_{ph} and θ_{pu} evolutions when commutation occurs in $[kT_s,(k+1)T_s]$.

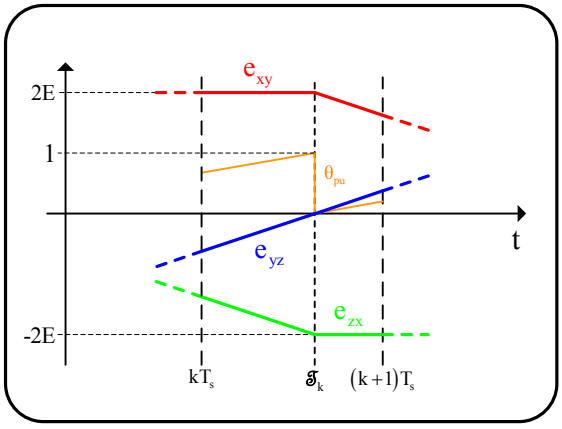

Figure II.7. e_{ch} and θ_{pu} evolutions when commutation occurs in $[kT_s,(k+1)T_s]$.

being:

$$e_{ch,k} = \pm\, 2E \cdot \begin{bmatrix} 1 \\ -\left(1-\theta_{pu,k}\right) \\ -\theta_{pu,k} \end{bmatrix}$$
$$\Delta e_{ch,k} = \pm\, 2E \cdot \omega_{pu,k} \cdot \left(\begin{bmatrix} 0 \\ 1 \\ -1 \end{bmatrix} \cdot \delta_{-2}\left(t - kT_s\right) + \begin{bmatrix} -1 \\ 0 \\ 1 \end{bmatrix} \cdot \delta_{-2}\left(t - \mathfrak{I}_k\right) \right) \tag{II.40}$$

In this way, the discrete time model of the system can be achieved, as in Eq. (II.41):

$$i_{ch,k+1} = f \cdot i_{ch,k} + g \cdot e_{ch,k} + \Delta_{ch,k} + h \cdot \Delta T_{ch,k} \tag{II.41}$$

being:

$$f = e^{-\frac{r}{L}\cdot T_s} \quad , \quad g = -\frac{1}{r} \cdot \left(1 - e^{-\frac{r}{L}\cdot T_s}\right) \quad , \quad h = \frac{V}{L} \cdot e^{-\frac{r}{L}\cdot\frac{T_s}{2}} \tag{II.42}$$

$$\Delta_{ch,k} = -\frac{1}{L} \cdot \int_{k\cdot T_s}^{(k+1)\cdot T_s} e^{-\frac{r}{L}\cdot\left((k+1)\cdot T_s - \tau\right)} \cdot \Delta e_{ch}\left(\tau\right) d\tau \tag{II.43}$$

In particular, substituting Eq. (II.40) in Eq. (II.43), it becomes:

$$\Delta_{ch,k} = \mp \frac{2E}{r} \omega_{pu,k} \cdot \left(gL \cdot \begin{bmatrix} 0 \\ 1 \\ -1 \end{bmatrix} - \frac{L}{r}\left(1 - e^{-\frac{r}{L}\left(1-\mathfrak{I}_{pu,k}\right)\cdot T_s}\right) \cdot \begin{bmatrix} -1 \\ 0 \\ 1 \end{bmatrix} - T_s \cdot \begin{bmatrix} \left(1-\mathfrak{I}_{pu,k}\right) \\ -1 \\ \mathfrak{I}_{pu,k} \end{bmatrix} \right) \tag{II.44}$$

In conclusion, the discrete torque equation can be easily achieved by replacing, in Eq. (II.10), the continuous variables with the corresponding discrete ones, obtaining the following Eq. (II.45):

$$T_{e,k+1} = \pm \frac{2}{3} p\Lambda \cdot \left(i_{xy,k+1} - \left(1-\theta_{pu,k+1}\right) \cdot i_{yz,k+1} - \theta_{pu,k} \cdot i_{zx,k+1} \right) \tag{II.45}$$

II.5. Predictive Control Algorithms

Both the traditional and the proposed control strategies can be employed by using predictive control algorithms; in particular, replacing in Eq. (II.41) the $i_{ch,k+1}$ vector with its reference value, the voltage pulse widths vector can be easily computed as in Eq. (II.46):

$$i_{ch,k+1} = i_{ch,k+1}^{(ref)} \quad \rightarrow \quad \Delta T_{ch,k} = \frac{1}{h}\left(i_{ch,k+1}^{(ref)} - \xi_{ch,k}\right) \tag{II.46}$$

being:

$$\xi_{ch,k} = f \cdot i_{ch,k} + g \cdot e_{ch,k} + \Delta_{ch,k} \tag{II.47}$$

In this way, the $\Delta T_{ch,k}$ value that guarantees, at the end of the sampling time interval, the achievement of the currents reference values is determined. However, it cannot always be realized due to the voltage saturation constraint, which is expressed by the following Eq. (II.48):

$$\left|\Delta T_{ab}\right| \le T_s \quad , \quad ab \in \{xy, yz, zx\} \tag{II.48}$$

Thus, when the voltage saturation occurs, it is necessary to define an appropriate saturation algorithm that guarantees the best performance available.

Firstly referring to the traditional control strategy, the i_y current must be kept constant during current commutation, also in case of voltage saturation; this condition is expressed by Eq. (II.49):

$$i_{y,k+1} = \frac{1}{3}\left(i_{yz,k+1} - i_{xy,k+1}\right) = \mp\Im \tag{II.49}$$

Therefore, considering Eq. (II.41), Eq. (II.49) can be also expressed as:

$$\Delta T_{xy,k} - \Delta T_{yz,k} = \zeta_{i,k}\left(\Im\right) \tag{II.50}$$

being:

$$\zeta_{i,k}\left(\Im\right) = \frac{1}{h}\left(\pm 3\Im + \xi_{yz,k} - \xi_{xy,k}\right) \tag{II.51}$$

Moreover, since:

$$\Delta T_{xy,k} + \Delta T_{yz,k} + \Delta T_{zx,k} = 0 \tag{II.52}$$

Eq. (II.53) can be also obtained:

$$\begin{aligned}\Delta T_{xy,k} &= -\frac{1}{2}\left(\Delta T_{zx,k} - \zeta_{i,k}\right)\\ \Delta T_{yz,k} &= -\frac{1}{2}\left(\Delta T_{zx,k} + \zeta_{i,k}\right)\end{aligned} \tag{II.53}$$

Thus, substituting Eq. (II.53) in Eq. (II.48), the voltage saturation constraint becomes:

$$\begin{aligned}-\left(2T_s - \zeta_{i,k}\right) \le \Delta T_{zx,k} \le \left(2T_s + \zeta_{i,k}\right)\\ -\left(2T_s + \zeta_{i,k}\right) \le \Delta T_{zx,k} \le \left(2T_s - \zeta_{i,k}\right)\\ -T_s \le \Delta T_{zx,k} \le T_s\end{aligned} \tag{II.54}$$

However, Eq. (II.54) can be better expressed as:

$$-\psi_{i,k} \le \Delta T_{zx,k} \le \psi_{i,k} \tag{II.55}$$

being:

$$\psi_{i,k} = \min\left\{\left(2T_s + \zeta_{i,k}\right), \left(2T_s - \zeta_{i,k}\right), T_s\right\} \tag{II.56}$$

Now, in order to reduce the current commutation as much as possible, the $\Delta T_{zx,k}$ value must be chosen as in Eq. (II.57):

$$\Delta T_{zx,k} = \mp\psi_{i,k} \tag{II.57}$$

Nevertheless, since Eq. (II.55) is applicable only if:

$$\psi_{i,k} \ge 0 \tag{II.58}$$

it is necessary to verify the following further condition:

$$\begin{aligned}&\left(2T_s + \zeta_{i,k}\right) \ge 0\\ &\left(2T_s - \zeta_{i,k}\right) \ge 0\end{aligned} \quad \rightarrow \quad \left|\zeta_{i,k}\right| \le 2T_s \tag{II.59}$$

Hence, when the voltage saturation occurs, if Eq. (II.59) is verified, the voltage pulse width vector $\Delta T_{ch,k}$ is:

$$\Delta T_{ch,k} = \frac{1}{2}\begin{bmatrix}1\\-1\\0\end{bmatrix}\zeta_{i,k} \mp \frac{1}{2}\begin{bmatrix}-1\\-1\\2\end{bmatrix}\psi_{i,k} \tag{II.60}$$

Otherwise, when Eq. (II.59) is not verified, the i_y current value cannot be kept constant further, so the voltage pulse width vector $\Delta T_{ch,k}$ is:

$$\Delta T_{ch,k} = \pm \begin{bmatrix} 1 \\ -1 \\ 0 \end{bmatrix} T_s \tag{II.61}$$

being, in this case:

$$\begin{aligned} \zeta_{i,k} &= \pm\ 2T_s \\ \psi_{i,k} &= 0 \end{aligned} \tag{II.62}$$

Now, considering the proposed control strategy, when the voltage saturation occurs, it is imposed the achievement of the torque value closest to the reference one. So, the following Eq. (II.63) is employed:

$$i_{ch,k+1} = \pm \frac{3\Im^{(sat)}}{2} \cdot \frac{1}{\left(1-\theta_{pu}+\theta_{pu}^2\right)} \begin{bmatrix} 1 \\ -\left(1-\theta_{pu}\right) \\ -\theta_{pu} \end{bmatrix} = i_{ch,k+1}^{(sat)} \tag{II.63}$$

in which $\Im^{(sat)}$ is the value closest to $\Im$, reachable at the end of the sampling time interval. Hence, by substituting Eq. (II.63) in Eq. (II.41), Eq. (II.64) is obtained:

$$i_{ch,k+1} = i_{ch,k+1}^{(sat)} \quad \rightarrow \quad \Delta T_{ch,k} = \frac{1}{h}\left(i_{ch,k+1}^{(sat)} - \xi_{ch,k}\right) \tag{II.64}$$

Now, since:

$$\begin{aligned} &\left(1-\theta_{pu}+\theta_{pu}^2\right) \geq 0 \\ &\left(1-\theta_{pu}\right) \geq 0 \qquad\qquad \forall \theta_{pu} \in [0,1) \\ &\theta_{pu} \geq 0 \end{aligned} \tag{II.65}$$

by substituting Eq. (II.64) in Eq. (II.48), the voltage saturation constraint becomes:

$$\begin{aligned} &-\frac{2}{3}\left(1-\theta_{pu}+\theta_{pu}^2\right)\left(hT_s - \xi_{xy,k}\right) \leq \pm\Im^{(sat)} \leq \frac{2}{3}\left(1-\theta_{pu}+\theta_{pu}^2\right)\left(hT_s + \xi_{xy,k}\right) \\ &-\frac{2}{3}\left(1-\theta_{pu}+\theta_{pu}^2\right)\frac{\left(hT_s + \xi_{yz,k}\right)}{\left(1-\theta_{pu}\right)} \leq \pm\Im^{(sat)} \leq \frac{2}{3}\left(1-\theta_{pu}+\theta_{pu}^2\right)\frac{\left(hT_s - \xi_{yz,k}\right)}{\left(1-\theta_{pu}\right)} \\ &-\frac{2}{3}\left(1-\theta_{pu}+\theta_{pu}^2\right)\frac{\left(hT_s + \xi_{zx,k}\right)}{\theta_{pu}} \leq \pm\Im^{(sat)} \leq \frac{2}{3}\left(1-\theta_{pu}+\theta_{pu}^2\right)\frac{\left(hT_s - \xi_{zx,k}\right)}{\theta_{pu}} \end{aligned} \tag{II.66}$$

Thus, in order to satisfy Eq. (II.66), the following condition must be verified:

$$-\mathcal{G}^{(\min)} \le \pm\mathcal{G}^{(\text{sat})} \le \mathcal{G}^{(\max)} \tag{II.67}$$

being:

$$\begin{aligned}
\mathcal{G}^{(\min)} &= \frac{2}{3}\left(1-\theta_{pu}+\theta_{pu}^2\right)\cdot\min\left\{\left(hT_s-\xi_{xy,k}\right),\frac{\left(hT_s+\xi_{yz,k}\right)}{\left(1-\theta_{pu}\right)},\frac{\left(hT_s+\xi_{zx,k}\right)}{\theta_{pu}}\right\}\\
\mathcal{G}^{(\max)} &= \frac{2}{3}\left(1-\theta_{pu}+\theta_{pu}^2\right)\cdot\min\left\{\left(hT_s+\xi_{xy,k}\right),\frac{\left(hT_s-\xi_{yz,k}\right)}{\left(1-\theta_{pu}\right)},\frac{\left(hT_s-\xi_{zx,k}\right)}{\theta_{pu}}\right\}
\end{aligned} \tag{II.68}$$

In conclusion, the equivalent drive control scheme is reported in Fig. II.8.

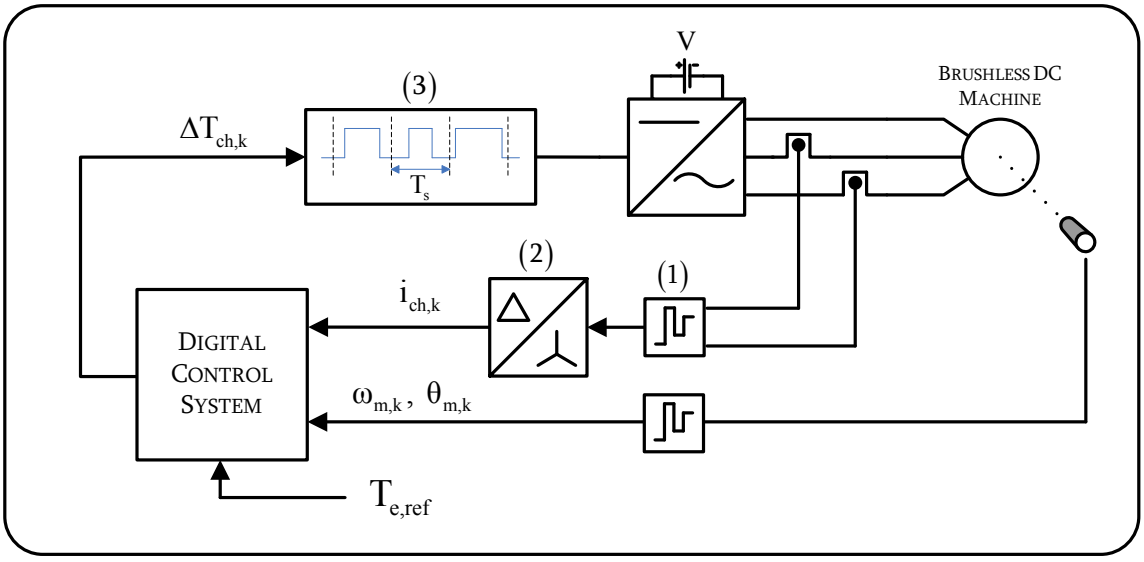

Figure II.8. Block Control Scheme of the Brushless DC Drive controlled by predictive algorithms: (1) sample and hold; (2) phase to chain transformation; (3) symmetrical pulses generator.

II.6. Simulations and Results

In order to verify the performances obtainable by both the traditional and the proposed control strategy, a simulation study was performed in the Matlab Simulink environment. Referring to the drive block scheme depicted in Fig. II.9, the DC voltage source, the inverter and the Brushless DC Machine were modelled by the SimPowerSystem Library, whereas the other control blocks were realized employing the Simulink Library. The inverter switching frequency and the load torque were set to 10 kHz and to 0 Nm respectively, whereas the other simulations parameters values are reported in Table II.1.

TABLE II.1

PARAMETERS		UNITS
r	2.5	[Ω]
L	11.2	[mH]
p	2	[-]
Λ	0.125	[Wb]
J_m	0.0016	[Kgm^2]
D_m	0.012	[Nms]
T_s	100	[μs]
V	100	[V]

The simulation study firstly refers to the start up of the motor, when a step reference torque of 0.36 Nm was applied, starting from rest. As a result, the low steady state speed value of 30 rad/s was achieved in about 1 s. The simulations results, referred to the steady state speed value, are reported from Fig. II.10 through II.21.

Firstly considering the results obtained by employing the traditional control strategy, it can be seen that different results can be achieved by employing either the unipolar modulation or the bipolar one, as highlighted from Fig. II.10 through II.12.

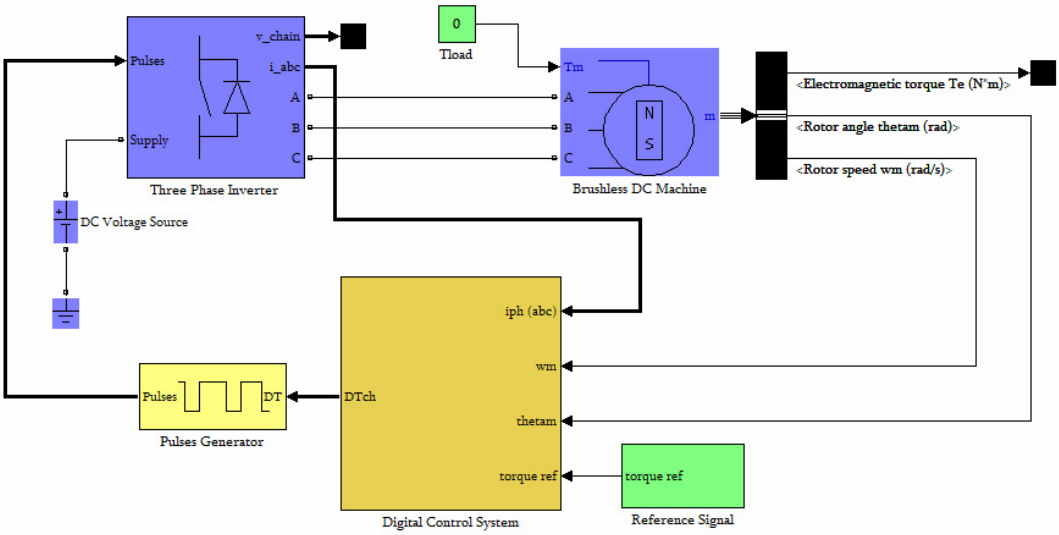

Figure II.9. Block Control Scheme of the Brushless DC Drive employed for the simulations.

In particular, employing the unipolar modulation, the current i_z begins to grow after the middle point of each sector, flowing through the free wheeling diodes. As a consequence, the torque ripple is increased and, above all, its mean value is slightly less than the reference one. This unwanted phenomena does not occur by employing the bipolar modulation, but which is characterized by very high currents and torque ripples compared to those achieved by the unipolar one. However, regardless of the modulation technique employed, current commutations last for a short time, not affecting the torque response significantly, as well shown from Fig. II.13 through II.15.

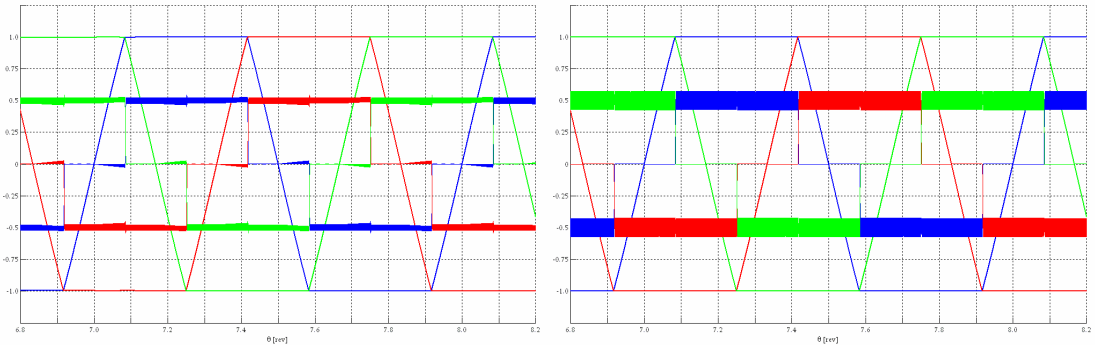

Figure II.10. Phase emfs and currents obtained by the traditional control strategy (in p.u.): unipolar (on the left) and bipolar modulation (on the right), $I^* = 1.44$ A, $E^* = 7.5$ V.

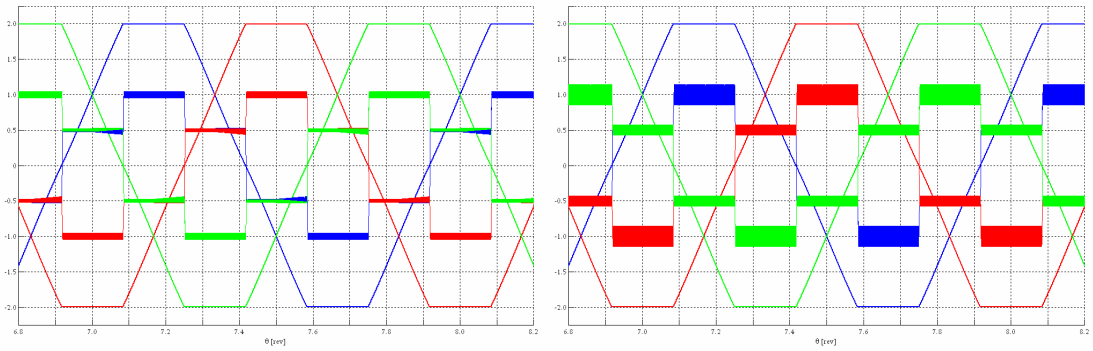

Figure II.11. Chain emfs and currents obtained by the traditional control strategy (in p.u.): unipolar (on the left) and bipolar modulation (on the right), $I^* = 1.44$ A, $E^* = 7.5$ V.

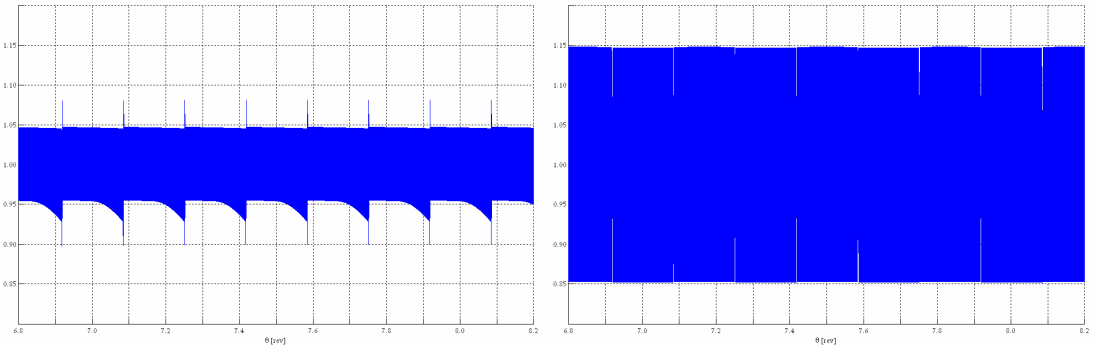

Figure II.12. Torque evolution obtained by the traditional control strategy (in p.u.): unipolar (on the left) and bipolar modulation (on the right), $T_e^* = 0.36$ Nm.

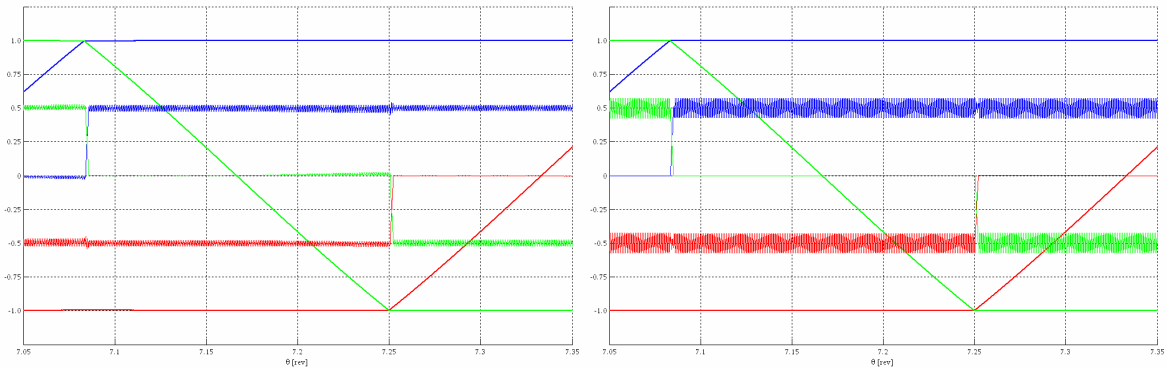

Figure II.13. Phase emfs and currents evolutions (in p.u.) (zoomed sight of Fig. II.15).

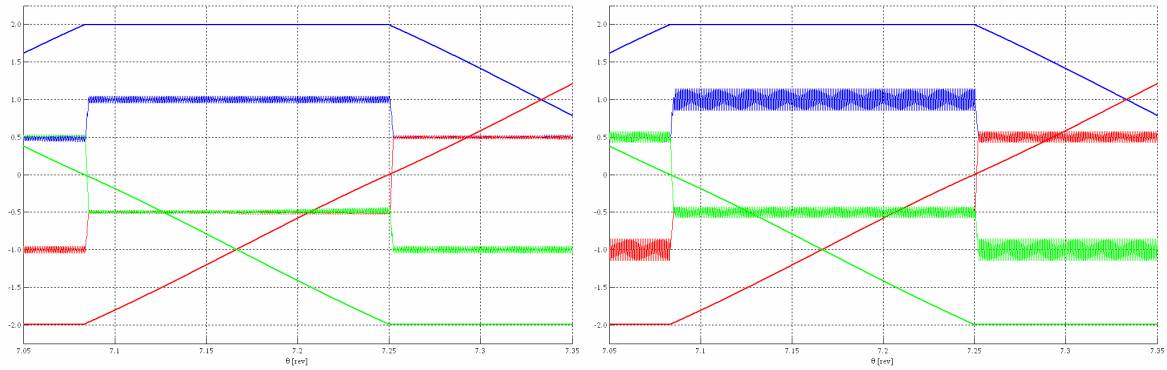

Figure II.14. Chain emfs and currents evolutions (in p.u.) (zoomed sight of Fig. II.16).

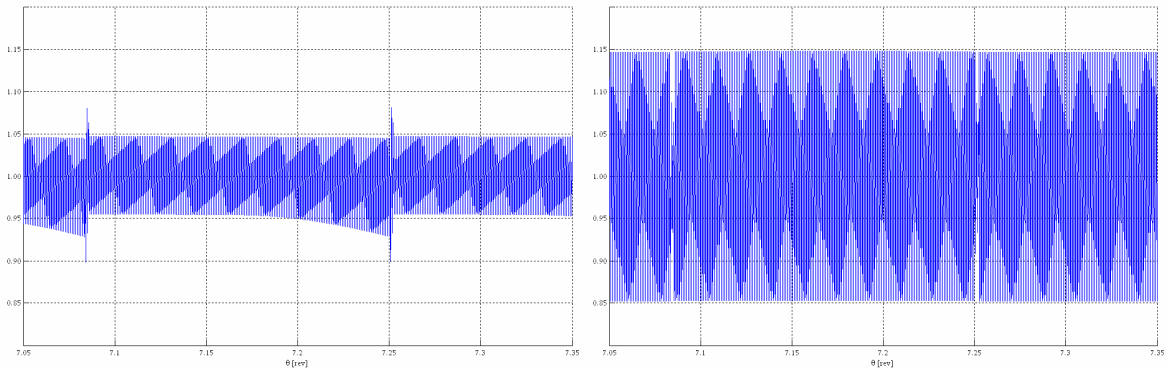

Figure II.15. Torque evolution (in p.u.) (zoomed sight of Fig. II.17).

Otherwise, the currents and torque responses obtained by employing the proposed control strategy are not affected by the previous drawbacks, as shown from Fig. II.16 through II.21. In particular, the value of the currents i_x and i_z is the same at start of each sector, so the traditional current commutation disappear. As a consequence, a better tracking of the currents reference values can be performed, so no mean torque value reduction occurs, being, at the same time, the currents and torque ripples quite small.

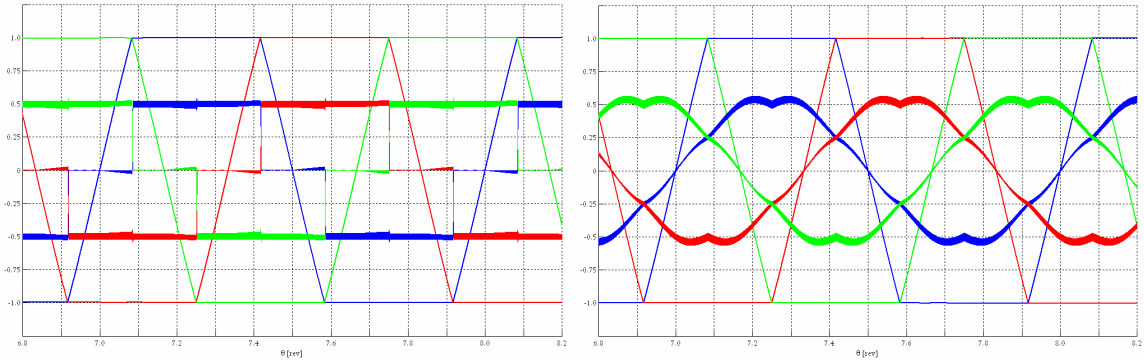

Figure II.16. Phase emfs and currents (in p.u.) obtained by the traditional control strategy (on the left) and by the proposed one (on the right): $I^* = 1.44$ A, $E^* = 7.5$ V.

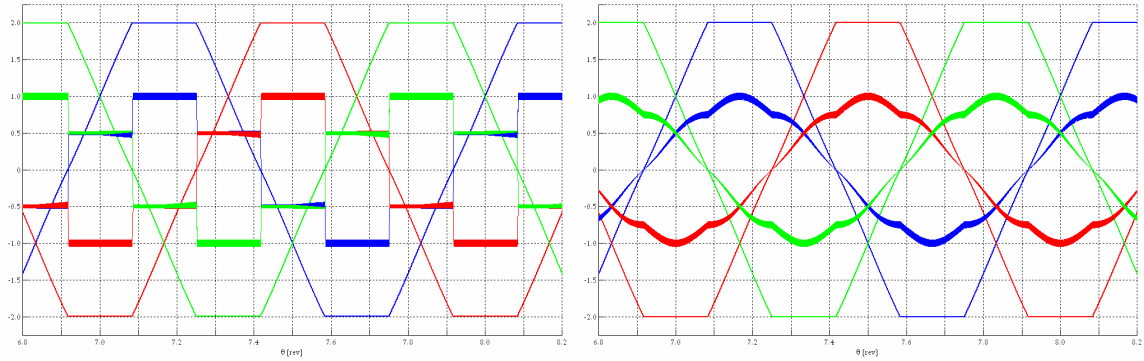

Figure II.17. Chain emfs and currents (in p.u.) obtained by the traditional control strategy (on the left) and by the proposed one (on the right): $I^* = 1.44$ A, $E^* = 7.5$ V.

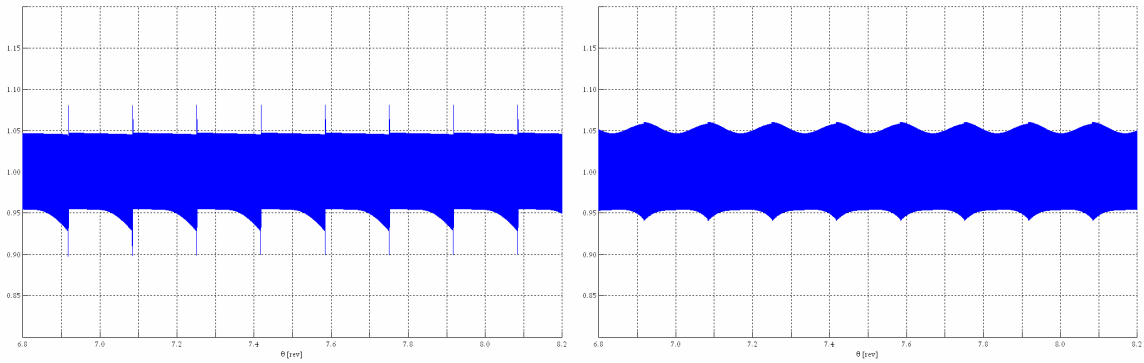

Figure II.18. Torque evolution (in p.u.) obtained by the traditional control strategy (on the left) and by the proposed one (on the right): $T_e^* = 0.36$ Nm.

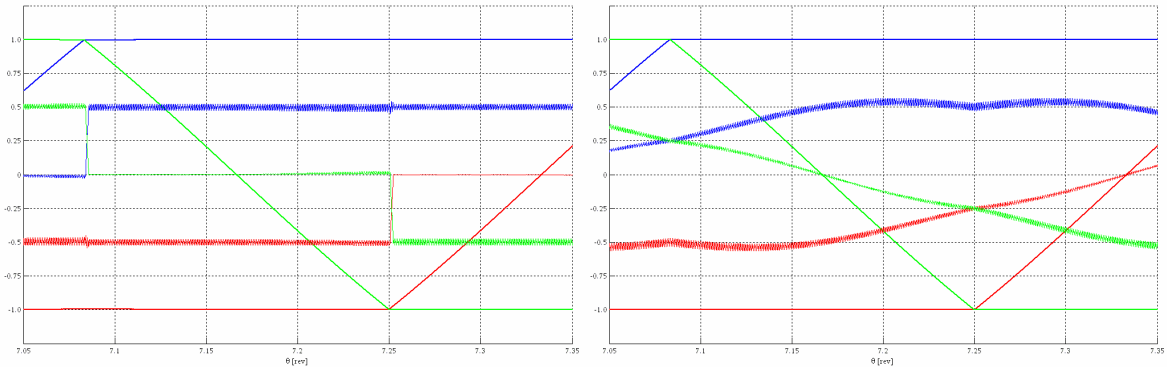

Figure II.19. Phase emfs and currents evolutions (in p.u.) (zoomed sight of Fig. II.21).

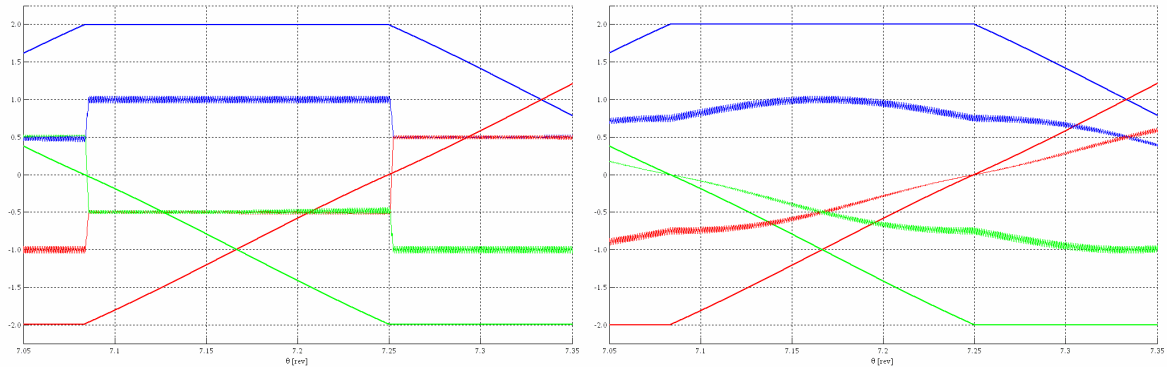

Figure II.20. Chain emfs and currents evolutions (in p.u.) (zoomed sight of Fig. II.22).

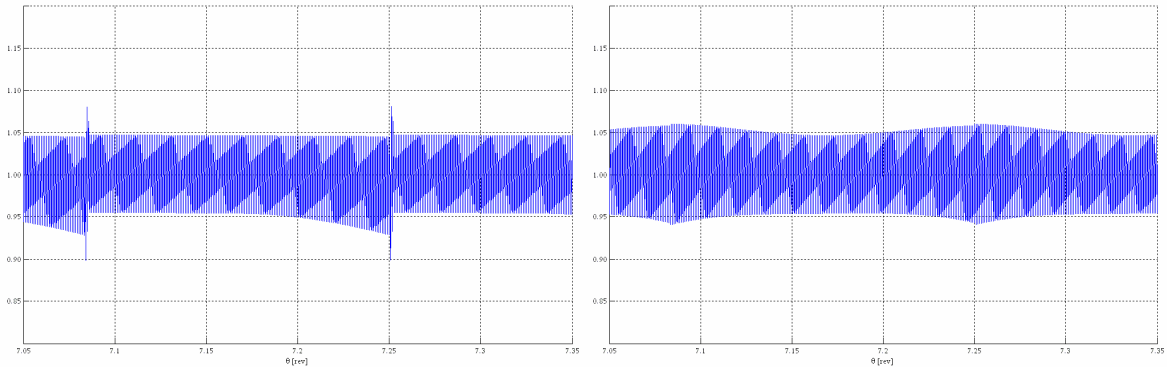

Figure II.21. Torque evolution (in p.u.) (zoomed sight of Fig. II.23).

After 1 s, when the steady state speed value was achieved, the reference torque value was increased to 1.3 Nm in order to reach the higher steady state speed value of about 108.3 rad/s. The simulations results, referred to the new steady state speed condition, are shown from Fig. II.22 through II.33.

Firstly considering the results obtained by the traditional control strategy, depicted from Fig. II.22 through Fig. II.27, it can be seen that the differences employing the unipolar modulation instead of using the bipolar one are less significant than at low speed operation. Anyway, the performances achieved are worse than before, although the current i_y is kept constant during current commutations. In fact, these ones last more than before, significantly affecting both the torque ripple and its mean value.

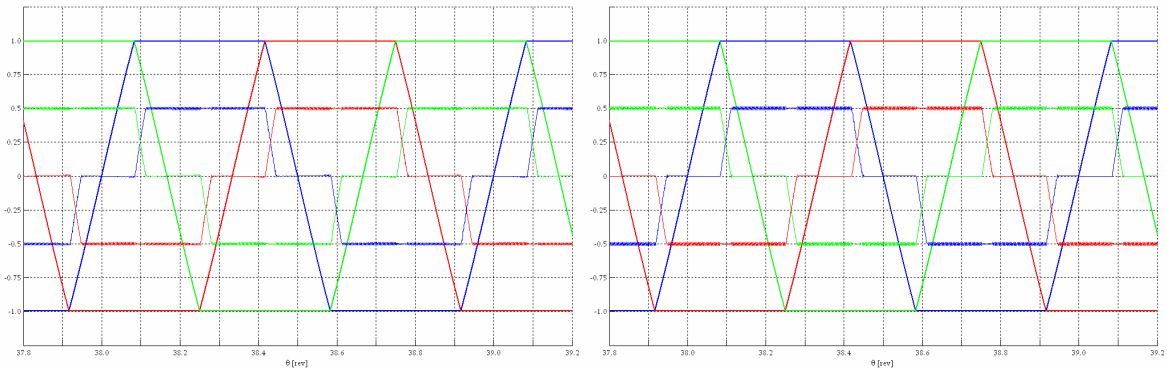

Figure II.22. Phase emfs and currents (in p.u.) obtained by the traditional control strategy: unipolar (on the left) and bipolar modulation (on the right), $I^* = 5.2$ A, $E^* \approx 27.1$ V.

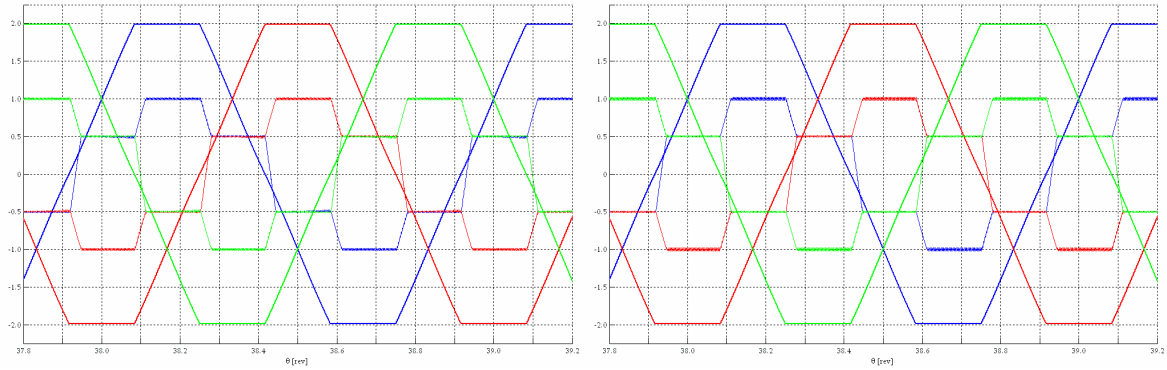

Figure II.23. Chain emfs and currents (in p.u.) obtained by the traditional control strategy: unipolar (on the left) and bipolar modulation (on the right), $I^* = 5.2$ A, $E^* \approx 27.1$ V.

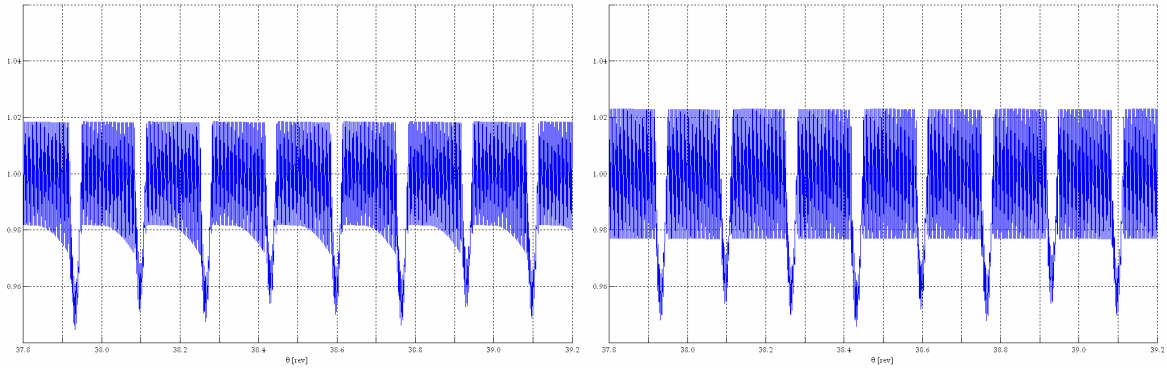

Figure II.24. Torque evolution (in p.u.) obtained by the traditional control strategy: unipolar (on the left) and bipolar modulation (on the right), $T_e^* = 1.3$ Nm.

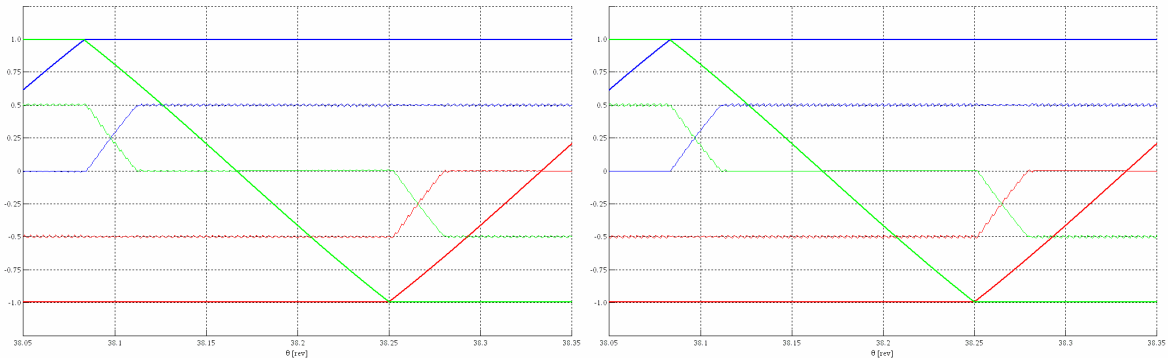

Figure II.25. Phase emfs and currents evolutions (in p.u.) (zoomed sight of Fig. II.27).

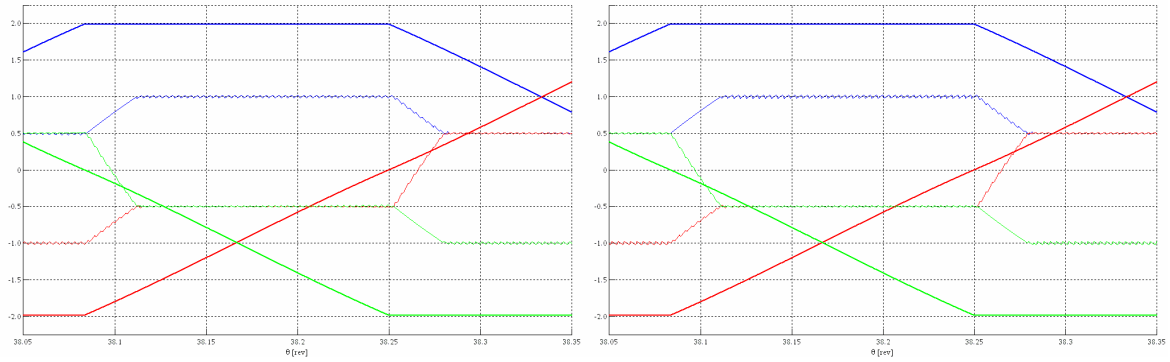

Figure II.26. Chain emfs and currents evolutions (in p.u.) (zoomed sight of Fig. II.28).

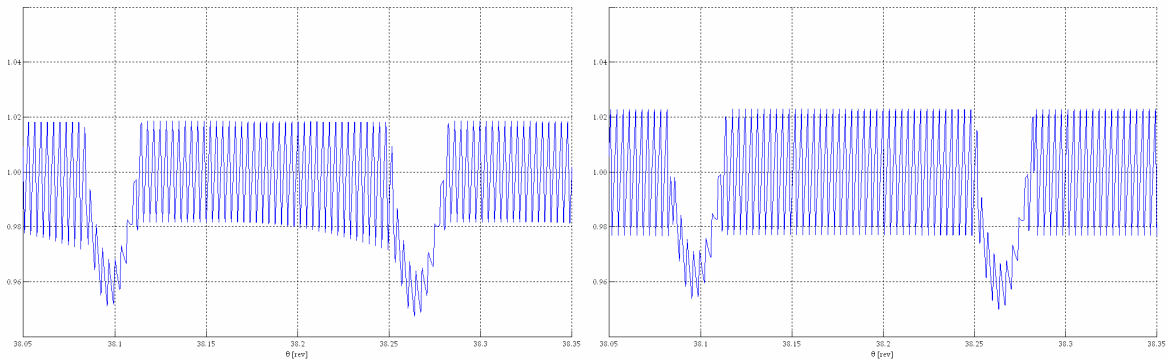

Figure II.27. Torque evolution (in p.u.) (zoomed sight of Fig. II.29).

On the contrary, the results obtained by employing the proposed control strategy are as good as those obtained at low speed operation, as highlighted from Fig. II.28 through II.33.

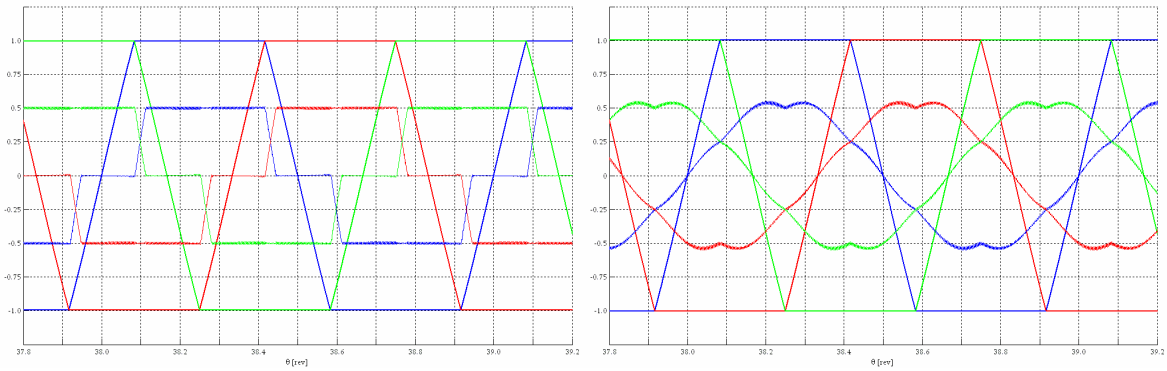

Figure II.28. Phase emfs and currents (in p.u.) obtained by the traditional control strategy (on the left) and by the proposed one (on the right): $I^* = 5.2$ A, $E^* \approx 27.1$ V.

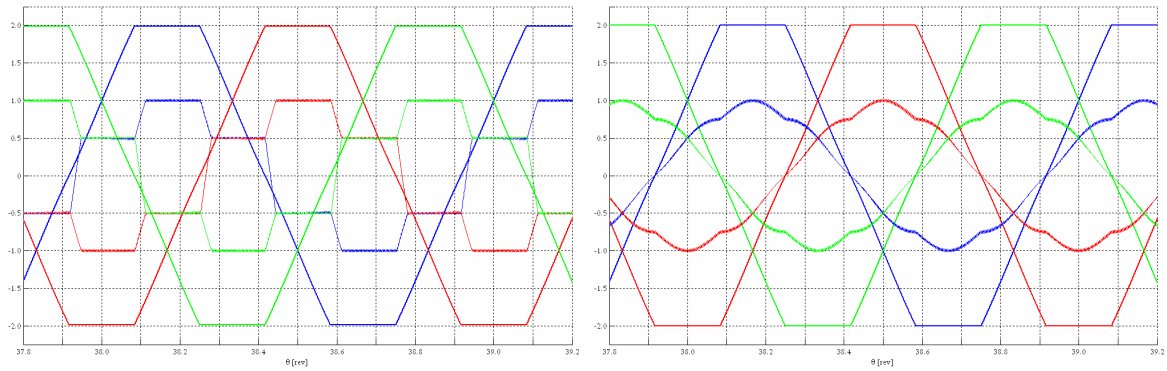

Figure II.29. Chain emfs and currents (in p.u.) obtained by the traditional control strategy (on the left) and by the proposed one (on the right): $I^* = 5.2$ A, $E^* \approx 27.1$ V.

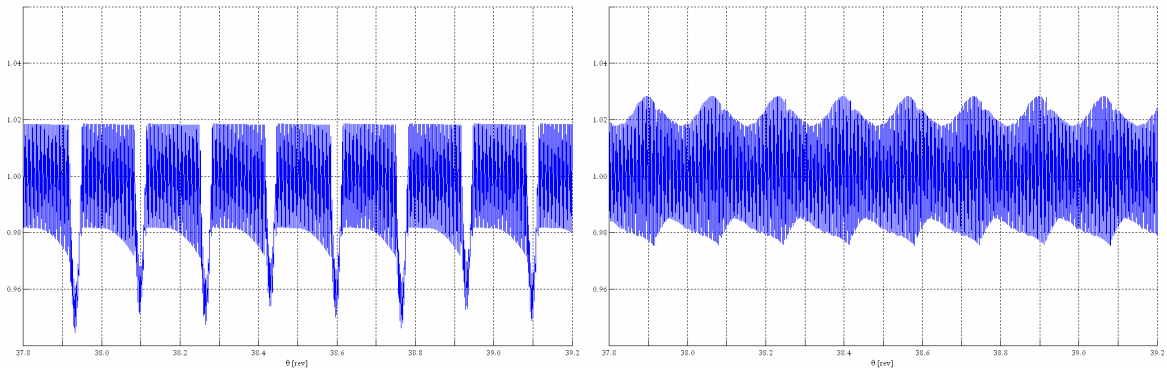

Figure II.30. Torque evolution (in p.u.) obtained by the traditional control strategy (on the left) and by the proposed one (on the right): $T_e^* = 1.3$ Nm.

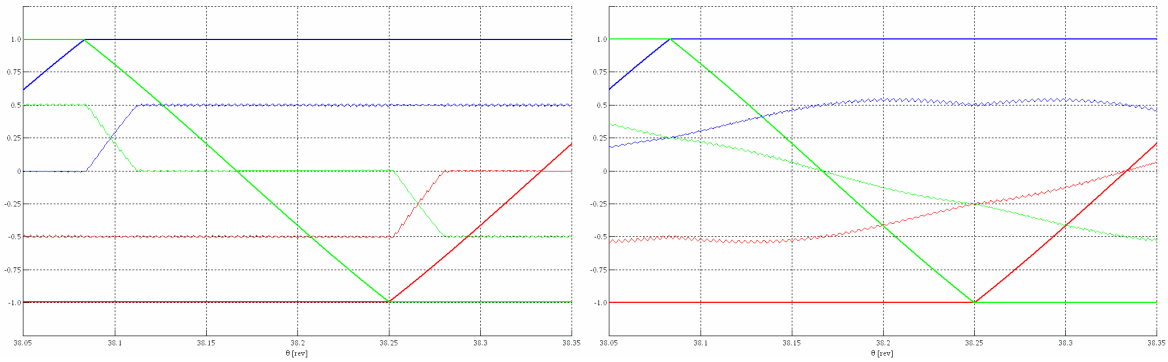

Figure II.31. Phase emfs and currents evolutions (in p.u.) (zoomed sight of Fig. II.27).

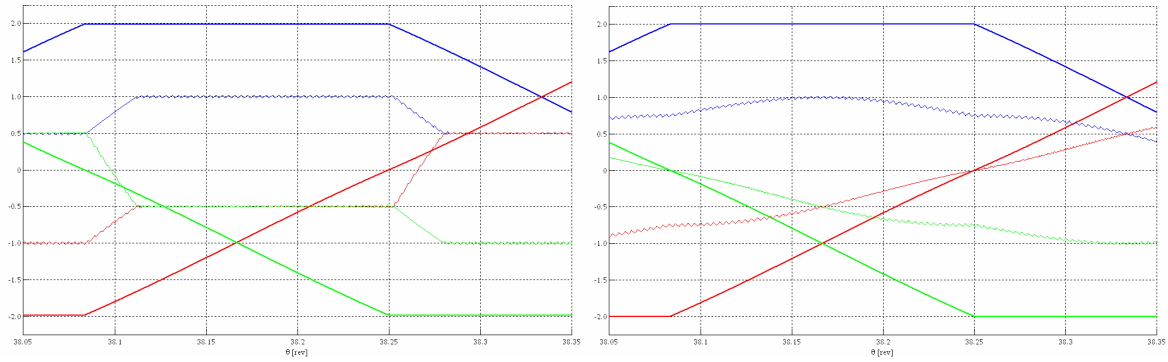

Figure II.32. Chain emfs and currents evolutions (in p.u.) (zoomed sight of Fig. II.28).

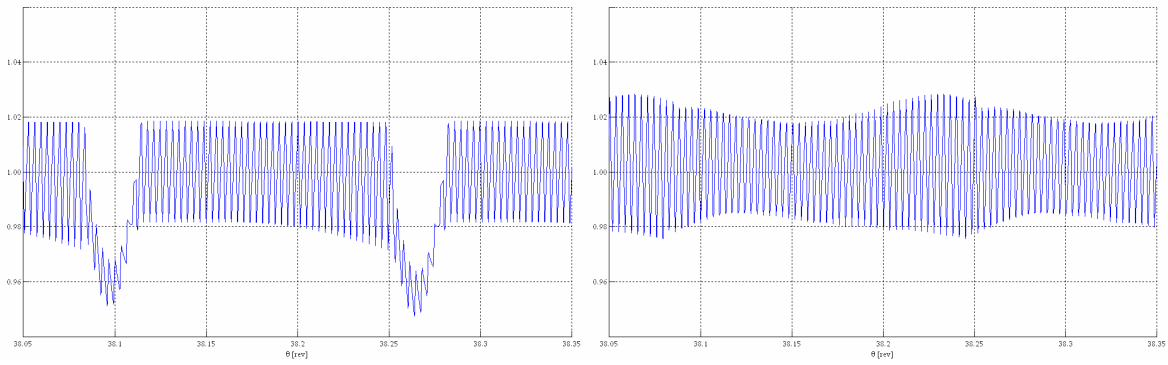

Figure II.33. Torque evolution (in p.u.) (zoomed sight of Fig. II.29).

In conclusion, after 2 s, the reference torque value is strongly increased with the aim of getting the maximum torque available. The results achieved at steady state operation by both the control strategies employed are reported from Fig. II.34 through II.36.

Firstly considering the traditional control strategy, both the unipolar and the bipolar modulation lead to six step operations: the mean torque value is about 1.71 Nm and its ripple, referred to the previous mean value, is about 40%. Moreover, the steady state speed value achieved is about 142.4 rad/s, as shown in Fig. II.37.

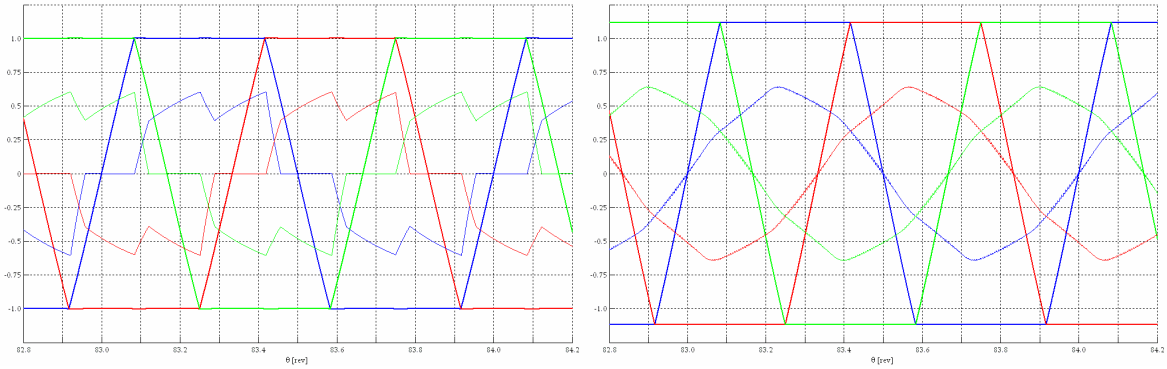

Figure II.34. Phase emfs and currents (in p.u.) obtained by the traditional control strategy (on the left) and by the proposed one (on the right): $I^* \approx 6.84$ A, $E^* \approx 35.6$ V.

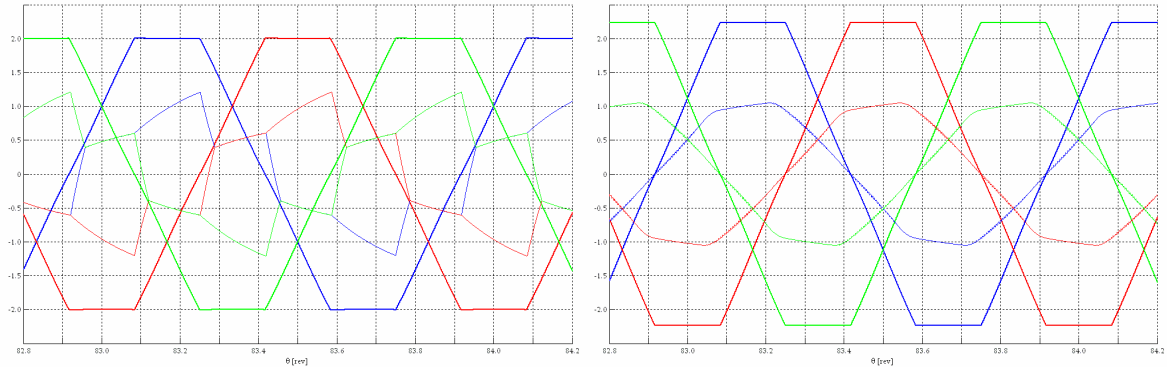

Figure II.35. Chain emfs and currents (in p.u.) obtained by the traditional control strategy (on the left) and by the proposed one (on the right): $I^* \approx 6.84$ A, $E^* \approx 35.6$ V.

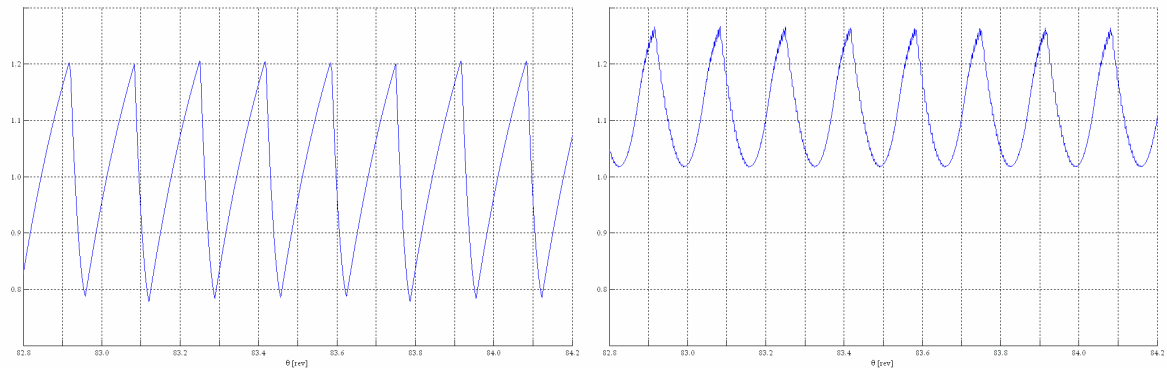

Figure II.36. Torque evolution (in p.u.) obtained by the traditional control strategy (on the left) and by the proposed one (on the right): $T_e^* \approx 1.71$ Nm.

Otherwise, the proposed control strategy allows the achievement of the higher mean torque value of 1.92 Nm (+12.3%), which corresponds to the higher steady state speed value of about 159.2 rad/s, as depicted in Fig. II.37. Furthermore, the torque ripple is significantly reduced to about 22.1% of its mean value.

In conclusion, all the simulations results confirm that the proposed control strategy allows the achievement of better performance than those obtainable by the traditional control strategy, especially at high speed operations.

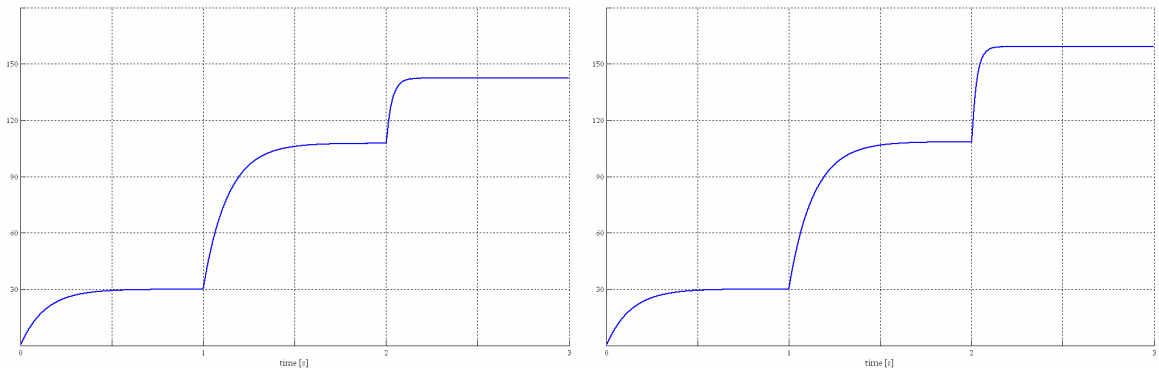

Figure II.37. Speed evolution (rad/s) obtained by the traditional control strategy (on the left) and by the proposed one (on the right).

III. SYNCHRONOUS RELUCTANCE DRIVE

III.1. Introduction

The improvements in design and optimization of the "axially laminated" or "distributed anisotropy" rotor of the Synchronous Reluctance Machine (SRM) allowed it to be employed in AC drives, in competition with both Permanent Magnet Machine (PMM) and Induction Machine (IM) drives [6-9]. In fact, by using a proper control, its torque density can be higher than that of the IM, but lower than that of PMM with high energy magnets. However, the latter one is more expensive, due to the high cost of the magnets. Furthermore, the SRM has a rugged rotor and it is maintenance free, like IM, while it does not present the rotor parameters variation consequent to overheating, which affects both PMM and IM.

Hence, since the mathematical model of SRM is a non-linear one, a complex control strategy is required: it is basically made up of coordinate transformations (stator-to-rotor and vice-versa) and stator mmf orientation along the rotor axis. As has been pointed out in a number of technical papers [10], in which also rotor magnetic saturation cross coupling effects have been considered, two main field orientations have been proposed. One consists in keeping the magnitude of the stator flux vector constant, while the torque is properly driven by the stator current component orthogonal to the stator flux vector. The other one consists in maintaining the air gap flux component constant along the rotor d-axis, while the torque is controlled by varying the q-axis current component. Due to the nonlinearities also present in the steady-state electrical equations, the former technique is less considered in the literature, compared to the latter one. Another control strategy, based on Direct Mean Torque Control and predictive algorithm, has been proposed recently in [11].

In this work, the applications of the PCT is widely considered. First of all, referring to the traditional control strategy, a predictive control algorithm is developed in order to achieve better performances compared to those obtainable by the traditional control techniques. However, since the time required by the predictive control algorithm is quite high, both the computation and the application of the voltage pulse widths vector cannot be carried out in the same sampling time interval, unless very fast processor units, like FPGAs, are employed [11-12]. Therefore, two other alternatives are

proposed: the first one consists in applying the voltage pulse widths vector with a delay of one sampling time interval, whereas the second one consists in employing predictive state observer. Hence, a simulation study is performed in order to highlight the performance obtainable by all the proposed solutions, also in comparison with the employment of the traditional PI regulators. As a result, it is shown that the delayed application of the voltage pulse widths vector is not a good alternative because it can give rise to oscillatory responses and instability. Otherwise, by employing predictive state observer, the application of the voltage pulse widths can be successfully postponed to the next sampling time intervals.

After that, the PCT is employed in order to develop a predictive optimal algorithm. First of all, the reference current values are chosen in order to achieve the minimum steady state Joule losses condition available. Secondly, the maximum torque variation available over each sampling time interval is imposed in order to achieve the reference torque value as fast as possible. Hence, a computer simulation of the drive is performed in the Matlab Simulink environment, with the aim of comparing the performance achievable by the proposed predictive optimal algorithm with that obtainable by the traditional technique and by predictive non optimal algorithms.

In conclusion, by introducing the magnetic saturation effects as in [13], all the control algorithms are properly modified in order to take into account this phenomena. As a consequence, a new simulation study is conducted in order to evaluate the performance obtainable by all the control algorithms previously considered.

III.2. Mathematical models

The electrical equations of the SRM are expressed by the following Eq. (III.1):

$$v = r \cdot i + \frac{d\lambda}{dt} \tag{III.1}$$

being r the phase resistance and v, i and λ the voltage, the current and the magnetic flux phase vector respectively, as in Eq. (III.2):

$$v = \begin{bmatrix} v_1 \\ v_2 \\ v_3 \end{bmatrix} \quad , \quad i = \begin{bmatrix} i_1 \\ i_2 \\ i_3 \end{bmatrix} \quad , \quad \lambda = \begin{bmatrix} \lambda_1 \\ \lambda_2 \\ \lambda_3 \end{bmatrix} \tag{III.2}$$

Hence, by introducing their corresponding space vectors by means of Eq. (III.3):

$$\mathbf{x}^{(s)} = \frac{2}{3} \cdot \left(x_1 + x_2 \cdot e^{j\frac{2}{3}\pi} + x_3 \cdot e^{j\frac{4}{3}\pi} \right) \quad , \quad \mathbf{x} = \{\mathbf{v}, \mathbf{i}, \boldsymbol{\lambda}\} \tag{III.3}$$

Eq. (III.4) is obtained:

$$\mathbf{v}^{(s)} = r \cdot \mathbf{i}^{(s)} + \frac{d\boldsymbol{\lambda}^{(s)}}{dt} \tag{III.4}$$

In particular, the space vector $\boldsymbol{\lambda}^{(s)}$ can be computed as follow:

$$\boldsymbol{\lambda}^{(s)} = \frac{3}{2}\left(L_0 \cdot \mathbf{i}^{(s)} + L_1 \cdot e^{j \cdot 2\theta} \cdot \overline{\mathbf{i}}^{(s)} \right) \quad , \quad L_0 > L_1 > 0 \tag{III.5}$$

being:

$$\theta = p \cdot \theta_m \tag{III.6}$$

where p are the pole pairs and θ_m is the rotor position. Now, changing from the stator reference frame to the rotor one by using the following Eq. (III.7):

$$\mathbf{x}^{(r)} = \mathbf{x}^{(s)} \cdot e^{-j \cdot \theta} \quad , \quad \mathbf{x} = \{\mathbf{v}, \mathbf{i}, \boldsymbol{\lambda}\} \tag{III.7}$$

Eq. (III.4) becomes:

$$\mathbf{v}^{(r)} = r \cdot \mathbf{i}^{(r)} + \frac{d\boldsymbol{\lambda}^{(r)}}{dt} + j\omega \cdot \boldsymbol{\lambda}^{(r)} \tag{III.8}$$

where:

$$\boldsymbol{\lambda}^{(r)} = \boldsymbol{\lambda}^{(s)} \cdot e^{-j \cdot \theta} = \frac{3}{2}\left(L_0 \cdot \mathbf{i}^{(r)} + L_1 \cdot \overline{\mathbf{i}}^{(r)} \right) \quad , \quad \omega = p \cdot \omega_m \tag{III.9}$$

being ω_m the rotor speed. Furthermore, Eq. (III.8) can be also expressed as:

$$v^{(r)} = r \cdot i^{(r)} + \frac{d\lambda^{(r)}}{dt} - \omega \cdot J \cdot \lambda^{(r)} \tag{III.10}$$

being:

$$v^{(r)} = \begin{bmatrix} v_d \\ v_q \end{bmatrix} \quad , \quad i^{(r)} = \begin{bmatrix} i_d \\ i_q \end{bmatrix} \quad , \quad \lambda^{(r)} = \begin{bmatrix} \lambda_d \\ \lambda_q \end{bmatrix} \quad , \quad J = \begin{bmatrix} 0 & 1 \\ -1 & 0 \end{bmatrix} \tag{III.11}$$

Now, since the complex power $\mathcal{A}$ can be computed by the following Eq. (III.12):

$$\mathcal{A} = \frac{3}{2} \mathbf{v}^{(s)} \cdot \overline{\mathbf{i}}^{(s)} = \frac{3}{2} \mathbf{v}^{(r)} \cdot \overline{\mathbf{i}}^{(r)} \tag{III.12}$$

where $\bar{}$ denotes the conjugate operator, the electrical power converted into the mechanical one is expressed as:

$$\mathcal{P}_m = -\frac{3}{2} \omega \cdot \Im\left\{ \boldsymbol{\lambda}^{(r)} \cdot \overline{\mathbf{i}}^{(r)} \right\} = -\frac{3}{2} \omega \cdot \left(i^{(r)} \right)^T \cdot J \cdot \lambda^{(r)} \tag{III.13}$$

Therefore, the electromagnetic torque is expressed as in Eq. (III.14):

$$T_e = \frac{\mathcal{P}_m}{\omega_m} = -\frac{3}{2} p \cdot \left(i^{(r)} \right)^T \cdot J \cdot \lambda^{(r)} = \frac{3}{2} p \cdot \left(\lambda^{(r)} \right)^T \cdot J \cdot i^{(r)} \tag{III.14}$$

Moreover, since $\lambda^{(r)}$ can be defined as in Eq. (III.15):

$$\lambda^{(r)} = \mathfrak{L}^{(r)} \cdot i^{(r)} \quad , \quad \mathfrak{L}^{(r)} = \begin{bmatrix} L_d & 0 \\ 0 & L_q \end{bmatrix} \tag{III.15}$$

being:

$$\begin{aligned} L_d &= \frac{3}{2}\left(L_0 + L_1 \right) \\ L_q &= \frac{3}{2}\left(L_0 - L_1 \right) \end{aligned} \quad , \quad L_d > L_q > 0 \tag{III.16}$$

the electrical equations and the electromagnetic torque can be expressed as in Eq. (III.17) and in Eq. (III.18) respectively:

$$v^{(r)} = r \cdot i^{(r)} + \mathfrak{L}^{(r)} \cdot \frac{di^{(r)}}{dt} - \omega \cdot J \cdot \mathfrak{L}^{(r)} \cdot i^{(r)} \tag{III.17}$$

$$T_e = \frac{3}{2} p \left(\mathfrak{L}^{(r)} \cdot i^{(r)} \right)^T \cdot J \cdot i^{(r)} = \frac{3}{2} p \left(L_d - L_q \right) \cdot i_d \cdot i_q \tag{III.18}$$

Finally, the mechanical equations are:

$$\begin{aligned} T_e &= D_m \cdot \omega_m + J_m \cdot \frac{d\omega_m}{dt} + T_{load} \\ \omega_m &= \frac{d\theta_m}{dt} \end{aligned} \qquad \text{(III.19)}$$

being J_m the rotor inertia, D_m the damping factor and T_{load} the load torque. So, the continuous time model of the SRM is defined by Eq. (III.17) through Eq. (III.19), in which the state variables are the dq current space vector components, the mechanical speed ω_m and the rotor position θ_m.

Now, in order to obtain the discrete time model of the SRM, only Eq. (III.17) and Eq. (III.18) are employed; in fact, it is supposed that the sampling time T_s is chosen sufficiently small in order to consider the rotor speed ω_m constant over each sampling time interval, equal to $\omega_{m,k}$. Hence, referring to the generic kT_s sampling time instant, Eq. (III.17) becomes:

$$\frac{di^{(r)}}{dt} = A_k \cdot i^{(r)} + B \cdot v^{(r)} \qquad \text{(III.20)}$$

being:

$$\begin{aligned} A_k &= \left(\mathcal{L}^{(r)}\right)^{-1} \cdot \left(-r \cdot I + \omega_k \cdot J \cdot \mathcal{L}^{(r)} \right) \\ B &= \left(\mathcal{L}^{(r)}\right)^{-1} \end{aligned} \quad , \quad I = \begin{bmatrix} 1 & 0 \\ 0 & 1 \end{bmatrix} \qquad \text{(III.21)}$$

Therefore, the discrete time model of the system, referred to the generic $[kT_s,(k+1)T_s]$ sampling time interval, is:

$$i_{k+1}^{(r)} = F_k \cdot i_k^{(r)} + H_k \cdot \Delta T_k^{(r)} \qquad \text{(III.22)}$$

where:

$$F_k = e^{A_k \cdot T_s} \quad , \quad H_k = e^{A_k \cdot \frac{T_s}{2}} \cdot B \cdot V \qquad \text{(III.23)}$$

being $\Delta T_k^{(r)}$ the dq voltage pulse widths vector. Finally, considering Eq. (III.18), the electromagnetic torque value reached at the end of the sampling time interval is:

$$T_{e,k+1} = \frac{3}{2} p \left(\mathcal{L}^{(r)} \cdot i_{k+1}^{(r)} \right)^T \cdot J \cdot i_{k+1}^{(r)} = \frac{3}{2} p \left(L_d - L_q \right) \cdot i_{d,k+1} \cdot i_{q,k+1} \qquad \text{(III.24)}$$

III.3. Control Strategies

The traditional control strategy employed for the SRM generally consists in keeping the i_d current vector component at some constant value, different from zero: this is done with the aim of linearly driving the electromagnetic torque by the i_q current vector component. However, this control strategy is characterized by some drawbacks: first of all, since the i_d value is not generally changed during drive operation, an optimal (i_d,i_q) steady state condition cannot be achieved for different reference torque values; secondly, this constraint does not guarantee the achievement of the best dynamic performance available.

Therefore, a novel control strategy is proposed in this work: it consists in achieving the reference torque value and the corresponding minimum Joule losses steady state condition, by simultaneously varying both the i_d and i_q current vector components. As a consequence, the currents reference values must satisfy the following Eq. (III.25) and Eq. (III.26):

$$\frac{3}{2}p\left(L_d - L_q\right)\cdot i_{d,ref}\cdot i_{q,ref} = T_{e,ref} \tag{III.25}$$

$$i_{d,ref}^2 + i_{q,ref}^2 = \mathfrak{I}_{ref} \tag{III.26}$$

being:

$$\mathfrak{I}_{ref} = \min_{T_e = T_{e,ref}} \left\{ \left\| i^{(r)} \right\| \right\} \tag{III.27}$$

Referring to the (i_d,i_q) plane, a graphical interpretation can be given: in fact, Eq. (III.25) represents the equilateral hyperbola whose points correspond to the $T_{e,ref}$ torque value; otherwise, Eq. (III.26) represents the circle centred in the origin and tangent to the previous hyperbola. Therefore, the tangent point of these two curves, which allows the achievement of both the reference torque value and the minimum current vector magnitude, can be easily determined by employing the following Eq. (III.28):

$$i_{d,ref} = i_{q,ref} = \pm\sqrt{\frac{\mathfrak{I}_{ref}}{2}} \tag{III.28}$$

being:

$$\mathfrak{I}_{ref} = \frac{4T_{e,ref}}{3p}\cdot\frac{1}{\left(L_d - L_q\right)} \tag{III.29}$$

If the family of the hyperbolas corresponding to different torque values is considered, the minimum Joule losses locus depicted in Fig. III.1 can be found: in fact, it is drawn by joining all the points of each torque hyperbola that are characterized by the minimum current vector magnitude.

However, since Eq. (III.27) imposes the reference current values only, it does not affect the i_d and i_q evolutions. Thus, these last ones only depend on both the voltage saturation and the current limitation constraints, which are respectively expressed by the following Eq. (III.30) and Eq. (III.31):

$$\left\| \mathbf{v}^{(r)} \right\| \leq \frac{V}{\sqrt{3}} \tag{III.30}$$

$$\left\| \mathbf{i}^{(r)} \right\| \leq \mathcal{G}_{max} \tag{III.31}$$

Therefore, when at least one of these occurs, the voltage vector synthesized by the control algorithms must be properly arranged.

In this work, two different solutions are proposed: the first one consists in varying the magnitude of the voltage vector only, in order to satisfy both Eq. (III.30) and Eq. (III.31). Nevertheless, this solution does not generally guarantee the improvement of the dynamic performance of the drive, which can be better assured by imposing the achievement of the reference torque value as fast as possible.

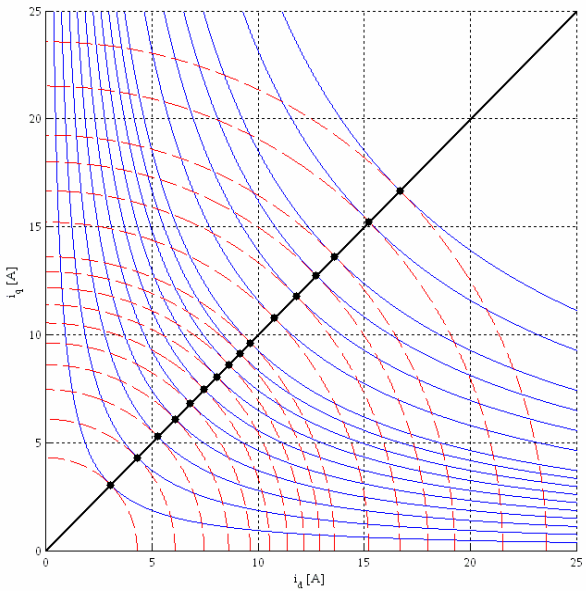

Figure III.1. Minimum Joule losses locus (in black), obtained by joining the points of each torque hyperbolas (in blue) tangent to the current circles centred in the origin (in red).

This can be done by satisfying the following Eq. (III.32):

$$\left|\tilde{T}_{e,k+1} - T_{e,ref}\right| = \min_{T_{e,k+1}} \left\{ \left|T_{e,k+1} - T_{e,ref}\right| \right\} \qquad \text{(III.32)}$$

being $\tilde{T}_{e,k+1}$ the torque value closest to $T_{e,ref}$ reachable at the end of the $[kT_s,(k+1)T_s]$ sampling time interval. However, when the reference torque value is achieved, the corresponding current vector value does not generally match the reference one. Therefore, it must be properly driven the to the minimum Joule losses condition along the reference torque hyperbola, in order to keep the torque constant at $T_{e,ref}$. In conclusion, the equivalent control scheme of the drive is depicted in Fig. III.6.

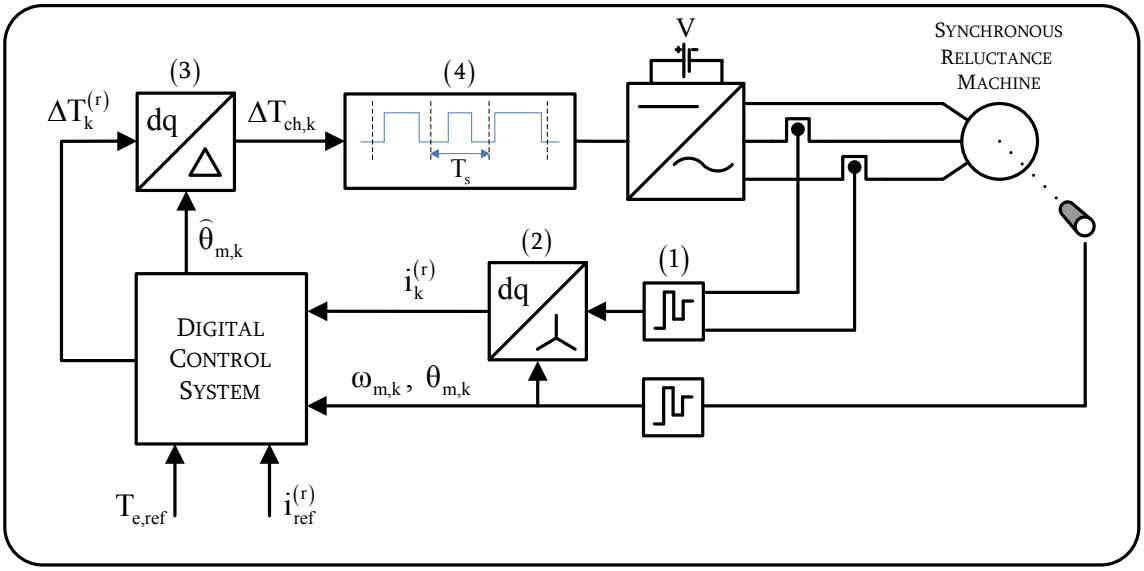

Figure III.2. Block Control Scheme of the Synchronous Reluctance Drive: (1) sample and hold; (2) phase to rotor dq transformation; (3) rotor dq to chain transformation; (4) symmetrical pulses generator.

III.4. Predictive Control Algorithms

Regardless of the control strategy employed, it is possible to compute the dq voltage pulse widths vector by imposing the achievement of the reference current values at the end of the sampling time interval, as in the following equation:

$$i_{k+1}^{(r)} = i_{ref}^{(r)} \qquad \rightarrow \qquad \Delta T_k^{(r)} = H_k^{-1} \cdot \left(i_{ref}^{(r)} - F_k \cdot i_k^{(r)} \right) \tag{III.33}$$

However this result cannot be generally achieved after only one sampling time interval, especially due to the voltage saturation constraint. In fact, it is necessary to always satisfy the following Eq. (III.34):

$$\left\| \Delta T_k^{(r)} \right\|^2 \le T^2 \qquad , \qquad T = \frac{T_s}{\sqrt{3}} \tag{III.34}$$

Hence, taking into account Eq. (III.22), Eq. (III.34) becomes:

$$\left(i_{k+1}^{(r)} \right)^T \cdot E_k \cdot i_{k+1}^{(r)} + 2 e_k^T \cdot i_{k+1}^{(r)} + e_{33,k} \le 0 \tag{III.35}$$

being:

$$\begin{aligned} E_k &= \begin{bmatrix} e_{11,k} & e_{12,k} \\ e_{12,k} & e_{22,k} \end{bmatrix} = H_k^{-T} \cdot H_k^{-1} \qquad , \qquad e_k = \begin{bmatrix} e_{13,k} \\ e_{23,k} \end{bmatrix} = -H_k^{-T} \cdot H_k^{-1} \cdot F_k \cdot i_k^{(r)} \\ e_{33,k} &= \left(F_k \cdot i_k^{(r)} \right)^T \cdot H_k^{-T} \cdot H_k^{-1} \cdot F_k \cdot i_k^{(r)} - T^2 \end{aligned} \tag{III.36}$$

Referring to the (i_d,i_q) plane, Eq. (III.35) corresponds to all the points inside the ellipse $\mathcal{E}_k$, whose parametric equation is:

$$i_{k+1}^{(r)} = c_k + r_k \tag{III.37}$$

respectively being c_k and r_k the centre and the "radius" of $\mathcal{E}_k$, both defined by the following Eq. (III.38):

$$\begin{aligned} c_k &= F_k \cdot i_k^{(r)} \\ r_k &= T \cdot H_k \cdot \begin{bmatrix} \cos(\tau_k) \\ \sin(\tau_k) \end{bmatrix} \qquad , \qquad \tau_k \in [0, 2\pi) \end{aligned} \tag{III.38}$$

First of all, the application of the traditional control strategy is considered, so a predictive traditional algorithm (PTA) is developed. At the start up of the motor, both

i_d and i_q are zero, so it is firstly necessary to reach the i_d reference value as fast as possible, by simultaneously keeping i_q constant to zero. This condition can be achieved by reaching the intersection point of $\mathfrak{S}_k$ with the d-axis, as highlighted in Fig. III.3; the corresponding i_d value, closest to $i_{d,ref}$, can be determined by the following Eq. (III.39):

$$e_{11,k} \cdot i_{d,k+1}^2 + 2 \cdot e_{13,k} \cdot i_{d,k+1} + e_{33,k} = 0 \qquad \text{(III.39)}$$

which gives the i_d values corresponding to both the intersection points of $\mathfrak{S}_k$ with the d-axis. Hence, the above procedure is recursively applied until the i_d reference value is reached.

After that, the reference torque value is achieved by properly varying the i_q current component. Also in this case, the voltage saturation constraint does not generally permit the achievement of the i_q reference value after only one sampling time interval. So, the PTA allows the achievement of the i_q value closest to $i_{q,ref}$, by simultaneously keeping i_d constant to $i_{d,ref}$. This condition can be satisfied by reaching the intersection point of $\mathfrak{S}_k$ with the $i_d = i_{d,ref}$ line, as shown in Fig. III.4. Thus, the corresponding i_q value can be computed by the following Eq. (III.40):

$$e_{22,k} \cdot i_{q,k+1}^2 + 2\left(e_{12,k} \cdot i_{d,ref} + e_{23,k}\right) \cdot i_{q,k+1} + \left(e_{11,k} \cdot i_{d,ref}^2 + 2e_{13,k} \cdot i_{d,ref} + e_{33,k}\right) = 0 \qquad \text{(III.40)}$$

Applying this procedure recursively, both the current reference values and, hence, the reference torque one, can be achieved.

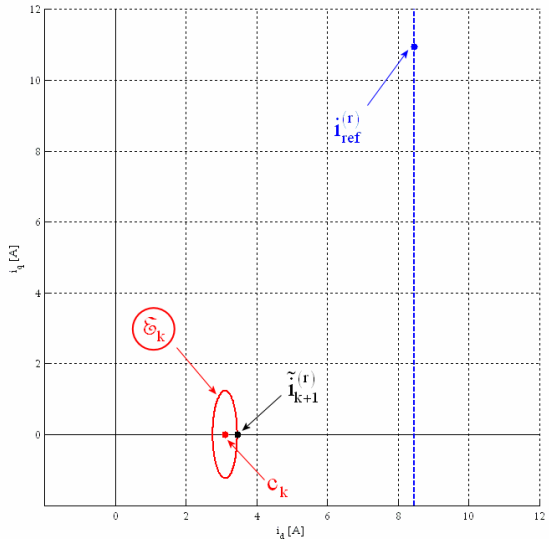

Figure III.3. Graphical representation of the PTA when voltage saturation occurs and $i_d \neq i_{d,ref}$.

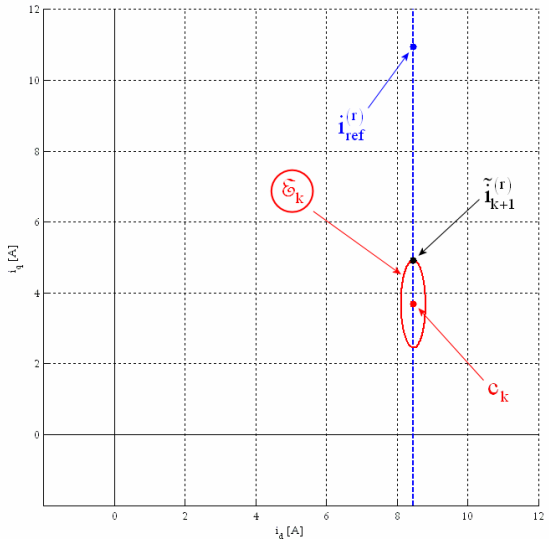

Figure III.4. Graphical representation of the PTA when voltage saturation occurs and $i_d = i_{d,ref}$.

However, in order to improve the performance obtainable by the traditional control strategy, another predictive algorithm, called predictive standard algorithm (PSA), is developed, which allows i_d and i_q to vary simultaneously. Moreover, when voltage saturation occurs, the PSA forces the current vector to reach the intersection point of the voltage saturation ellipse $\mathfrak{S}_k$ with the line going through c_k and i_{ref}, as shown in Fig. III.5. So, the current state value reached at the end of the sampling time interval can be computed by the following Eq. (III.41):

$$\tilde{i}_{k+1}^{(r)} = c_k + \frac{T}{\left| H_k^{-1} \cdot \left(i_{ref}^{(r)} - c_k \right) \right|} \cdot \left(i_{ref}^{(r)} - c_k \right) \qquad \text{(III.41)}$$

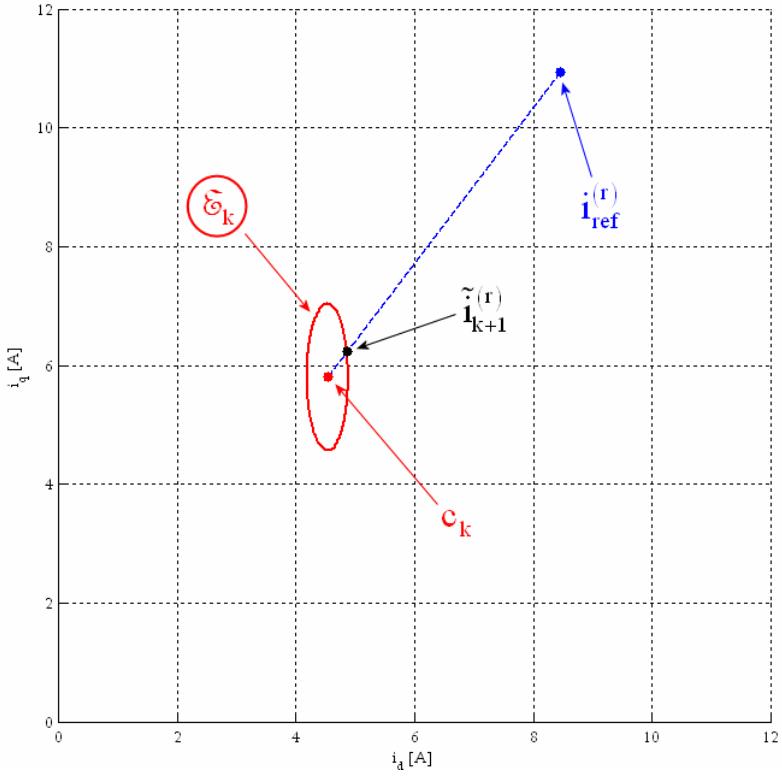

Figure III.5. Graphical representation of the PSA when $i \neq i_{ref}$.

However, since the PSA does not guarantee the improvement of the dynamic performance of the drive, a predictive optimal algorithm (POA) is developed in order to achieve the torque reference value as fast as possible. Therefore, when voltage saturations occurs, the achievement of the torque value closest to $T_{e,ref}$ is imposed: this optimal value corresponds to the tangent point of $\mathfrak{S}_k$ with the torque curve $\tilde{\mathfrak{I}}_{k+1}$, as shown in Fig. III.6.

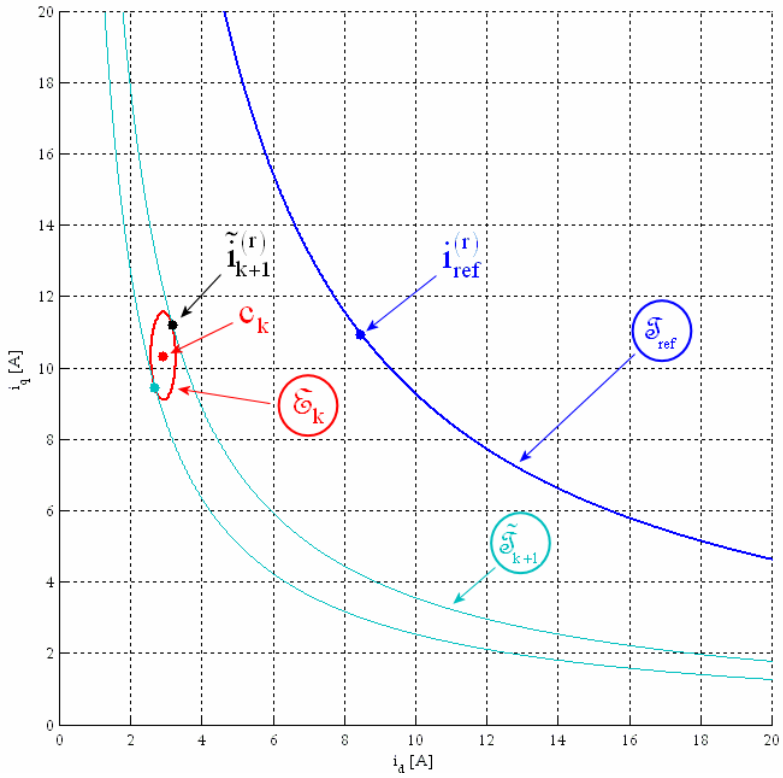

Figure III.6. Graphical representation of the proposed predictive algorithm when voltage saturation occurs and $T_e \neq T_{,e,ref}$.

In order to find $\tilde{\mathfrak{T}}_{k+1}$, the equation of the generic torque hyperbola $\mathfrak{T}_{k+1}$ is firstly considered:

$$\left(i^{(r)}_{k+1}\right)^T \cdot Q \cdot i^{(r)}_{k+1} + 2 \cdot q^T \cdot i^{(r)}_{k+1} + q_{33,k} = 0 \qquad \text{(III.42)}$$

being:

$$Q = \begin{bmatrix} q_{11} & q_{12} \\ q_{12} & q_{22} \end{bmatrix} = \frac{1}{2}\left(\left(\mathcal{L}^{(r)}\right)^T \cdot J - J \cdot \mathcal{L}^{(r)}\right) \quad , \quad q = \begin{bmatrix} q_{13} \\ q_{23} \end{bmatrix} = \begin{bmatrix} 0 \\ 0 \end{bmatrix} \quad , \quad q_{33,k} = -\frac{2T_{e,k+1}}{3p} \qquad \text{(III.43)}$$

Hence, since the tangent point belongs to both $\tilde{\mathfrak{T}}_{k+1}$ and $\mathfrak{E}_k$, by substituting Eq. (III.37) in Eq. (III.42), the following result is achieved:

$$\left[\cos(\tau_k) \quad \sin(\tau_k)\right] \cdot U_k \cdot \begin{bmatrix} \cos(\tau_k) \\ \sin(\tau_k) \end{bmatrix} \cdot T^2 + 2u_k^T \cdot \begin{bmatrix} \cos(\tau_k) \\ \sin(\tau_k) \end{bmatrix} \cdot T + u_{33,k} = 0 \qquad \text{(III.44)}$$

being:

$$\begin{aligned} U_k &= H_k^T \cdot Q \cdot H_k \\ u_k &= H_k^T \cdot \left(Q \cdot c_k + q_k\right) \\ u_{33,k} &= \left(c_k^T \cdot Q + 2q_k^T\right) \cdot c_k + q_{33,k} \end{aligned} \qquad \text{(III.45)}$$

Now, considering that:

$$\cos(\tau_k)=\frac{1}{2}\left(e^{j\cdot\tau_k}+e^{-j\cdot\tau_k}\right) \quad , \quad \sin(\tau_k)=-j\cdot\frac{1}{2}\left(e^{j\cdot\tau_k}-e^{-j\cdot\tau_k}\right) \tag{III.46}$$

by substituting Eq. (III.46) in Eq. (III.44), the following expression is obtained:

$$\mathbf{a}_k\cdot e^{j\cdot 4\tau_k}+\mathbf{b}_k\cdot e^{j\cdot 3\tau_k}+c_k\cdot e^{j\cdot 2\tau_k}+\overline{\mathbf{b}}_k\cdot e^{j\cdot\tau_k}+\overline{\mathbf{a}}_k=0 \tag{III.47}$$

being:

$$\begin{aligned}\mathbf{a}_k&=\left(\left(u_{11,k}-u_{22,k}\right)-j\cdot 2u_{12,k}\right)\cdot T^2\\ \mathbf{b}_k&=4\left(u_{13,k}-j\cdot u_{23,k}\right)\cdot T\\ c_k&=\left(\left(u_{11,k}+u_{22,k}\right)\cdot T^2+2u_{33,k}\right)\end{aligned} \tag{III.48}$$

Finally, imposing, in Eq. (III.47), the existence condition of two coincident solutions, the following equations are achieved:

$$w_k^T\cdot\Lambda_k\cdot t_k=0 \tag{III.49}$$

$$e^{j\cdot\tau_k}=-T\cdot\frac{w_k^T\cdot\mathbf{N}_k\cdot t_k}{w_k^T\cdot\mathbf{M}_k\cdot t_k} \tag{III.50}$$

where Λ_k, $\mathbf{N}_k$ and $\mathbf{M}_k$ are the matrixes defined in Eq. (III.54) and in Eq. (III.55), being:

$$\begin{aligned}w_k^T&=\left[u_{33,k}^4 \quad u_{33,k}^3 \quad u_{33,k}^2 \quad u_{33,k} \quad 1\right]\\ t_k^T&=\left[T^8 \quad T^6 \quad T^4 \quad T^2 \quad 1\right]\end{aligned} \tag{III.51}$$

In particular, Eq. (III.49) allows the determination of all the torque hyperbolas tangent to $\mathcal{E}_k$, whereas Eq. (III.50) determines the phases of the dq voltage pulse widths vector that must be applied in order to reach their tangent point with $\mathcal{E}_k$. Therefore, by properly choosing the torque hyperbola tangent to $\mathcal{E}_k$, the corresponding tangent point can be reached by applying the following voltage pulse widths vector:

$$\Delta\mathbf{T}_k^{(r)}=T\cdot e^{j\cdot\tau_k}=-T^2\cdot\frac{w_k^T\cdot\mathbf{N}_k\cdot t_k}{w_k^T\cdot\mathbf{M}_k\cdot t_k} \tag{III.52}$$

Employing the above mentioned procedure recursively, the reference torque hyperbola $\mathcal{T}_{ref}$ is reached. However, when it occurs, the currents values reached do not generally correspond to the minimum joule losses condition. So, the POA drives the current vector along $\mathcal{T}_{ref}$ in order to get its reference value as fast as possible. This is carried out

by reaching, at the end of each sampling time interval, the intersection point of $\mathcal{E}_k$ with $\mathcal{T}_{ref}$, closest to i_{ref}, as shown in Fig. III.7. This value can be computed by substituting Eq. (III.37) in the following Eq. (III.53):

$$\left(i_{k+1}^{(r)}\right)^T \cdot Q \cdot i_{k+1}^{(r)} + 2 \cdot q^T \cdot i_{k+1}^{(r)} + q_{33,ref} = 0 \quad , \quad q_{33,ref} = -\frac{2T_{e,ref}}{3p} \tag{III.53}$$

In conclusion, the matrixes employed in Eq. (III.49), (III.50) and (III.52) are:

$$\Lambda = \begin{bmatrix} 0 & 0 & 0 & 0 & \lambda_{15} \\ 0 & 0 & 0 & \lambda_{24} & \lambda_{25} \\ 0 & 0 & \lambda_{33} & \lambda_{34} & \lambda_{35} \\ 0 & \lambda_{42} & \lambda_{43} & \lambda_{44} & 0 \\ \lambda_{51} & \lambda_{52} & \lambda_{53} & \lambda_{54} & 0 \end{bmatrix} \tag{III.54}$$

$$\mathbf{N} = \begin{bmatrix} 0 & 0 & 0 & 0 & 0 \\ 0 & 0 & 0 & 0 & 0 \\ 0 & 0 & 0 & 0 & \mathbf{n}_{35} \\ 0 & 0 & 0 & \mathbf{n}_{44} & \mathbf{n}_{45} \\ 0 & 0 & \mathbf{n}_{53} & \mathbf{n}_{54} & 0 \end{bmatrix} \quad , \quad \mathbf{M} = \begin{bmatrix} 0 & 0 & 0 & 0 & 0 \\ 0 & 0 & 0 & 0 & \mathbf{m}_{25} \\ 0 & 0 & 0 & \mathbf{m}_{34} & \mathbf{m}_{35} \\ 0 & 0 & \mathbf{m}_{43} & \mathbf{m}_{44} & 0 \\ 0 & \mathbf{m}_{52} & \mathbf{m}_{53} & \mathbf{m}_{54} & 0 \end{bmatrix} \tag{III.55}$$

whose coefficients are defined in the following pages.

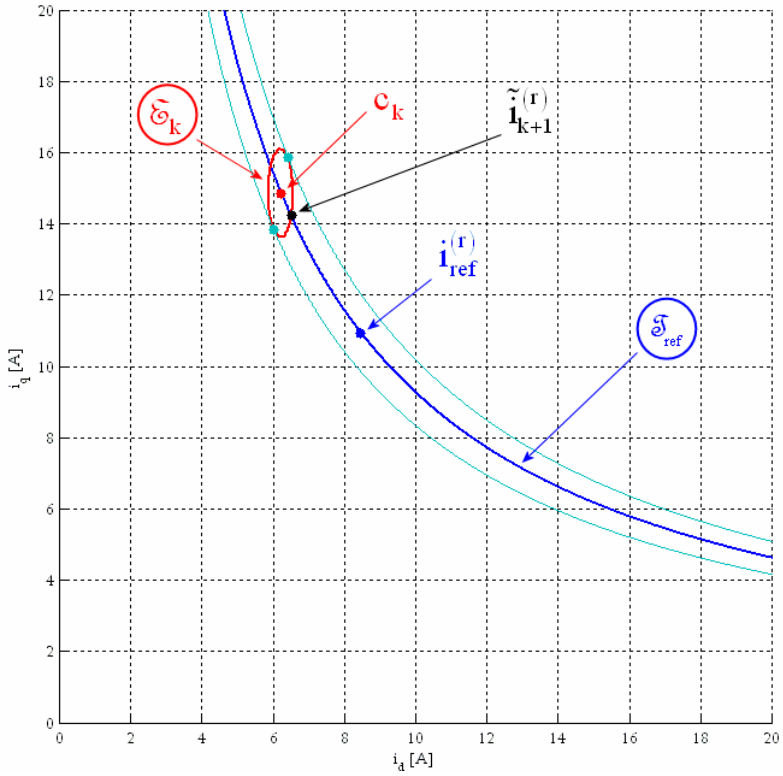

Figure III.7. Graphical representation of the POA when voltage saturation occurs and $T_e = T_{e,ref}$.

$$\lambda_{15} = \left(u_{11} - u_{22}\right)^2 + 4u_{12}^2$$

$$\begin{cases} \lambda_{24} = 2\left(u_{11} + u_{22}\right) \cdot \left(\left(u_{11} - u_{22}\right)^2 + 4u_{12}^2\right) \\ \lambda_{25} = -2\left(\left(u_{11} - u_{22}\right) \cdot \left(u_{13}^2 - u_{23}^2\right) + 4u_{12}u_{13}u_{23}\right) \end{cases}$$

$$\begin{cases} \lambda_{33} = \left(u_{11}^2 + 4u_{11}u_{22} + u_{22}^2 - 2u_{12}^2\right) \cdot \left(\left(u_{11} - u_{22}\right)^2 + 4u_{12}^2\right) \\ \lambda_{34} = -2\left(u_{11}^2 \cdot \left(4u_{13}^2 + u_{23}^2\right) + u_{22}^2 \cdot \left(u_{13}^2 + 4u_{23}^2\right) + 5\left(u_{13}^2 + u_{23}^2\right) \cdot \left(2u_{12}^2 - u_{11}u_{22}\right) + \right. \\ \qquad \left. + 6u_{12}u_{13}u_{23} \cdot \left(u_{11} + u_{22}\right)\right) \\ \lambda_{35} = \left(u_{13}^2 + u_{23}^2\right)^2 \end{cases}$$

$$\begin{cases} \lambda_{42} = 2\left(u_{11} + u_{22}\right) \cdot \left(u_{11}u_{22} - u_{12}^2\right) \cdot \left(\left(u_{11} - u_{22}\right)^2 + 4u_{12}^2\right) \\ \lambda_{43} = 2\left(-\left(u_{11}^3 \cdot \left(u_{13}^2 + 4u_{23}^2\right) + u_{22}^3 \cdot \left(4u_{13}^2 + u_{23}^2\right)\right) + 6u_{12}u_{13}u_{23} \cdot \left(u_{11}^2 - 4u_{11}u_{22} + u_{22}^2 + 6u_{12}^2\right)\right. \\ \qquad - 5u_{11}u_{22} \cdot \left(u_{11} \cdot \left(u_{13}^2 - 2u_{23}^2\right) - u_{22} \cdot \left(2u_{13}^2 - u_{23}^2\right)\right) + \\ \qquad \left. - u_{12}^2 \cdot \left(u_{11} \cdot \left(u_{13}^2 + 19u_{23}^2\right) + u_{22} \cdot \left(19u_{13}^2 + u_{23}^2\right)\right)\right) \\ \lambda_{44} = 2\left(u_{13}^2 + u_{23}^2\right) \cdot \left(u_{11} \cdot \left(5u_{13}^2 - 4u_{23}^2\right) - u_{22} \cdot \left(4u_{13}^2 - 5u_{23}^2\right) + 18u_{12}u_{13}u_{23}\right) \end{cases}$$

$$\begin{cases} \lambda_{51} = \left(u_{11} \cdot u_{22} - u_{12}^2\right)^2 \cdot \left(\left(u_{11} - u_{22}\right)^2 + 4u_{12}^2\right) \\ \lambda_{52} = 2\left(-2\left(u_{23}^2u_{11}^4 + u_{13}^2u_{22}^4\right) - \left(u_{13}^2 + u_{23}^2\right) \cdot \left(u_{11}^2u_{22}^2 - u_{11}u_{22}u_{12}^2 + 6u_{12}^4\right) + \right. \\ \qquad + 2u_{12}u_{13}u_{23} \cdot \left(2\left(u_{11}^3 + u_{22}^3\right) - 3\left(u_{11}u_{22} - 3u_{12}^2\right) \cdot \left(u_{11} + u_{22}\right)\right) + \\ \qquad - u_{11}u_{22} \cdot \left(u_{11}^2 \cdot \left(u_{13}^2 - 4u_{23}^2\right) - u_{22}^2 \cdot \left(4u_{13}^2 - u_{23}^2\right)\right) + \\ \qquad \left. - u_{12}^2 \cdot \left(u_{11}^2 \cdot \left(u_{13}^2 + 10u_{23}^2\right) + u_{22}^2 \cdot \left(10u_{13}^2 + u_{23}^2\right)\right)\right) \\ \lambda_{53} = u_{11}^2 \cdot \left(u_{13}^4 - 8u_{23}^4\right) - u_{22}^2 \cdot \left(8u_{13}^4 - u_{23}^4\right) + 2u_{13}^2u_{23}^2 \cdot \left(10\left(u_{11}^2 + u_{22}^2\right) - 19u_{11}u_{22}\right) + \\ \qquad + 4\left(u_{13}^4 + u_{23}^4\right) \cdot \left(2u_{11}u_{22} + 3u_{12}^2\right) + \\ \qquad - 12u_{12}u_{13}u_{23} \cdot \left(3u_{11} \cdot \left(u_{13}^2 - 2u_{23}^2\right) - 3u_{22} \cdot \left(2u_{13}^2 - u_{23}^2\right) + 7u_{12}u_{13}u_{23}\right) \\ \lambda_{54} = -4\left(u_{13}^2 + u_{23}^2\right)^3 \end{cases}$$

$$\mathbf{n}_{35} = \left(u_{13} + j \cdot u_{23}\right) \cdot \left(u_{11} - u_{22} - j \cdot 2u_{12}\right)$$

$$\begin{cases} \mathbf{n}_{44} = -\left(u_{11} - u_{22} - j \cdot 2u_{12}\right) \cdot \left(u_{11} \cdot \left(u_{13} - j \cdot 3u_{23}\right) - u_{22} \cdot \left(3u_{13} - j \cdot u_{23}\right) + j \cdot 4u_{12} \cdot \left(u_{13} - j \cdot u_{23}\right)\right) \\ \mathbf{n}_{45} = -\left(u_{13}^2 + u_{23}^2\right) \cdot \left(u_{13} - j \cdot u_{23}\right) \end{cases}$$

$$\begin{cases} \mathbf{n}_{53} = j \cdot \left(u_{11} - u_{22} - j \cdot 2u_{12}\right) \cdot \left(2u_{11}u_{23} \cdot \left(u_{11} + j \cdot u_{12}\right) - j \cdot 2u_{22}u_{13} \cdot \left(u_{22} - j \cdot u_{12}\right) + \right. \\ \qquad + j \cdot u_{11}u_{22} \cdot \left(u_{13} + j \cdot u_{22}\right) + \\ \qquad \left. - u_{12} \cdot \left(u_{13} \cdot \left(2u_{11} + j \cdot 3u_{12}\right) - j \cdot u_{23} \cdot \left(2u_{22} - j \cdot 3u_{12}\right)\right)\right) \\ \mathbf{n}_{54} = \left(u_{13} - j \cdot u_{23}\right) \cdot \left(u_{11} \cdot \left(u_{13}^2 - 2u_{23}^2\right) - u_{22} \cdot \left(2u_{13}^2 - u_{23}^2\right) + \right. \\ \qquad \left. - j \cdot 6u_{13}u_{23} \cdot \left(u_{11} - u_{22} + j \cdot 2u_{12}\right) + j \cdot 6u_{12} \cdot \left(u_{13}^2 - u_{23}^2\right)\right) \end{cases}$$

$$\mathbf{m}_{25} = 2\left(u_{11} - u_{22} - j \cdot 2u_{12}\right)$$

$$\begin{cases} \mathbf{m}_{34} = 3\left(u_{11} - u_{22} - j \cdot 2u_{12}\right) \cdot \left(u_{11} + u_{22}\right) \\ \mathbf{m}_{35} = -2\left(u_{13} - j \cdot u_{23}\right)^2 \end{cases}$$

$$\begin{cases} \mathbf{m}_{43} = \left(u_{11} - u_{22} - j \cdot 2u_{12}\right) \cdot \left(u_{11}^2 + u_{22}^2 + 4u_{11}u_{22} - 2u_{12}^2\right) \\ \mathbf{m}_{44} = -\left(u_{13} - j \cdot u_{23}\right) \cdot \left(u_{11} \cdot \left(9u_{13} + j \cdot 5u_{23}\right) - u_{22} \cdot \left(5u_{13} + j \cdot 9u_{23}\right) - j \cdot 14u_{12} \cdot \left(u_{13} + j \cdot u_{23}\right)\right) \end{cases}$$

$$\begin{cases} \mathbf{m}_{52} = \left(u_{11} - u_{22} - j \cdot 2u_{12}\right) \cdot \left(u_{11}u_{22} - u_{12}^2\right) \cdot \left(u_{11} + u_{22}\right) \\ \mathbf{m}_{53} = -u_{11}^2 \cdot \left(u_{13}^2 + 6u_{23}^2\right) + u_{22}^2 \cdot \left(6u_{13}^2 + u_{23}^2\right) + j \cdot 4u_{13}u_{23} \cdot \left(u_{11}^2 + u_{22}^2 - u_{11}u_{22}\right) + \\ \qquad + 7u_{11}u_{22} \cdot \left(u_{13}^2 - u_{23}^2\right) - 6u_{12}^2 \cdot \left(u_{13}^2 - u_{23}^2 + j \cdot 4u_{13}u_{23}\right) + \\ \qquad - j \cdot 2u_{12} \cdot \left(u_{11} \cdot \left(u_{13}^2 - 8u_{23}^2\right) - u_{22} \cdot \left(8u_{13}^2 - u_{23}^2\right) + j \cdot 9u_{13}u_{23} \cdot \left(u_{11} - u_{22}\right)\right) \\ \mathbf{m}_{54} = 6\left(u_{13}^2 + u_{23}^2\right) \cdot \left(u_{13} - j \cdot u_{23}\right)^2 \end{cases}$$

III.5. Predictive State Observer

Since the time required by predictive control algorithms is relatively high, the employment of predictive state observer is proposed in order to successfully postpone the application of the voltage pulse widths vector to the next sampling time intervals.

Therefore, since the continuous time model of the SRM expressed by Eq. (III.17) through Eq. (III.19) is non linear, some assumptions are needed in order to get the discrete time model of the state observer. First of all, since the mechanical time constant is quite large compared to the electrical ones, Eq. (III.20) can still be employed in place of Eq. (III.17). Moreover, applying the traditional control strategy, i_d is assumed constant in Eq. (III.18), equal to $i_{d,k}$. In this way, the following result is achieved:

$$T_e = \frac{3}{2} p \left(L_d - L_q \right) \cdot i_{d,k} \cdot i_q \tag{III.56}$$

Hence, also assuming the load torque disturbance equal to zero, the continuous time model of the SRM can be now expressed as in Eq. (III.57):

$$\frac{dx}{dt} = \hat{A}_k \cdot x + \hat{B} \cdot v \tag{III.57}$$

where:

$$x = \begin{bmatrix} i_d \\ i_q \\ \omega_m \\ \theta_m \end{bmatrix} \quad , \quad \hat{A}_k = \begin{bmatrix} A_k & \varnothing \\ A_{21,k} & A_{22,k} \end{bmatrix} \quad , \quad \hat{B} = \begin{bmatrix} B \\ \varnothing \end{bmatrix} \tag{III.58}$$

being:

$$A_{21,k} = \frac{3}{2} \frac{p}{J_m} \left(L_d - L_q \right) \cdot i_{d,k} \cdot \begin{bmatrix} 0 & 1 \\ 0 & 0 \end{bmatrix} \quad , \quad A_{22,k} = \frac{1}{J_m} \begin{bmatrix} -D_m & 0 \\ J_m & 0 \end{bmatrix} \tag{III.59}$$

Thus, the discrete time model of the predictive state observer can be obtained as in Eq. (III.60):

$$\hat{x}_{k+1} = \hat{F}_k \cdot \hat{x}_k + \hat{H}_k \cdot \Delta T_k + G_k \cdot \left(x_k - \hat{x}_k \right) \tag{III.60}$$

being $\hat{x}$ the observed state and G_k the gain matrix, which is chosen in order to set the observer poles to the required values, whereas the other matrixes are defined by Eq. (III.61):

$$\hat{F}_k = e^{\hat{A}_k \cdot T_s} \quad , \quad \hat{H}_k = e^{\hat{A}_k \cdot \frac{T_s}{2}} \cdot \hat{B} \cdot V \tag{III.61}$$

Therefore, being $\{\mathbf{p}_d, \mathbf{p}_q, p_\omega, 1\}$ the continuous system poles, in this work the observer ones $\{\hat{p}_d, \hat{p}_q, \hat{p}_\omega, \hat{p}_\theta\}$ are set as in Eq. (III.62):

$$\begin{aligned} \hat{p}_{d,k} &= 3 \cdot \Re\left\{\mathbf{p}_{d,k}\right\} \quad , \quad \hat{p}_{q,k} = 3 \cdot \Re\left\{\mathbf{p}_{q,k}\right\} \\ \hat{p}_\omega &= 3 \cdot p_\omega \quad , \quad \hat{p}_\theta = \tfrac{1}{5} \hat{p}_\omega \end{aligned} \tag{III.62}$$

Therefore, the gain matrix G_k was chosen as in Eq. (III.63):

$$G_k = \hat{F}_k - \mathrm{diag}\left\{e^{\hat{p}_{d,k} \cdot T_s}, e^{\hat{p}_{q,k} \cdot T_s}, e^{\hat{p}_\omega \cdot T_s}, e^{\hat{p}_\theta \cdot T_s}\right\} \tag{III.63}$$

III.6. Magnetic Saturation Effects

Although L_d and L_q are assumed constants, as in Eq. (III.16), they strongly depend on both i_d and i_q values, due to the magnetic saturation effects. Hence, Eq. (III.16) should be better replaced by Eq. (III.64) [13]:

$$\begin{aligned} L_d &= A_0 + \frac{B_0}{i_d^4 + C_0 \cdot i_d^2 + D_0} - \frac{B_1}{i_d^4 + C_1 \cdot i_d^2 + D_1} \cdot \left(1 - \frac{1}{1 + C_q \cdot i_q^2}\right) \\ L_q &= A_2 + \frac{B_2}{i_q^4 + C_2 \cdot i_q^2 + D_2} - \frac{B_3}{i_q^4 + C_3 \cdot i_q^2 + D_3} \cdot \left(1 - \frac{1}{1 + C_d \cdot i_d^2}\right) \end{aligned} \qquad \text{(III.64)}$$

In fact, by measuring L_d and L_q at different $i^{(r)}$ values, it is possible to determine all the coefficients of Eq. (III.64) so that it reproduces the L_d and L_q evolutions, as pointed out in [13]. All the coefficients values are reported in Table III.1, whereas the L_d and L_q evolutions are shown in Fig. III.8 and III.9 respectively.

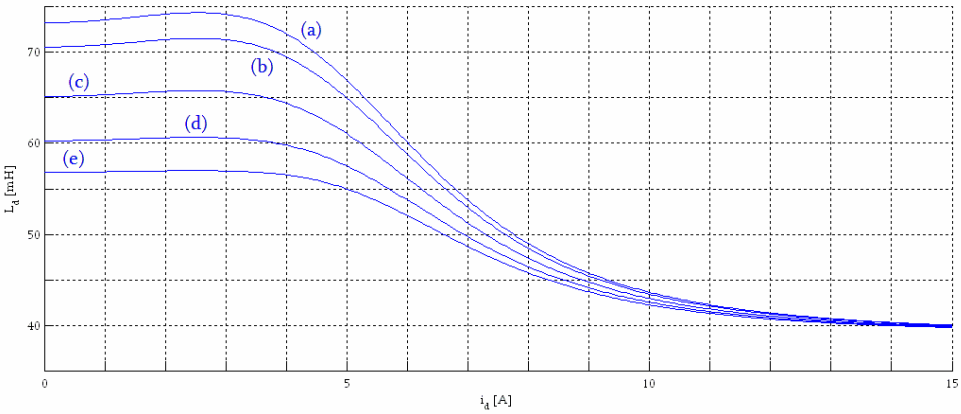

Figure III.8. L_d evolutions for different i_q values: i_q = 0 A (a), i_q = 3 A (b), i_q = 6 A (c), i_q = 9 A (d), i_q = 12 A (e).

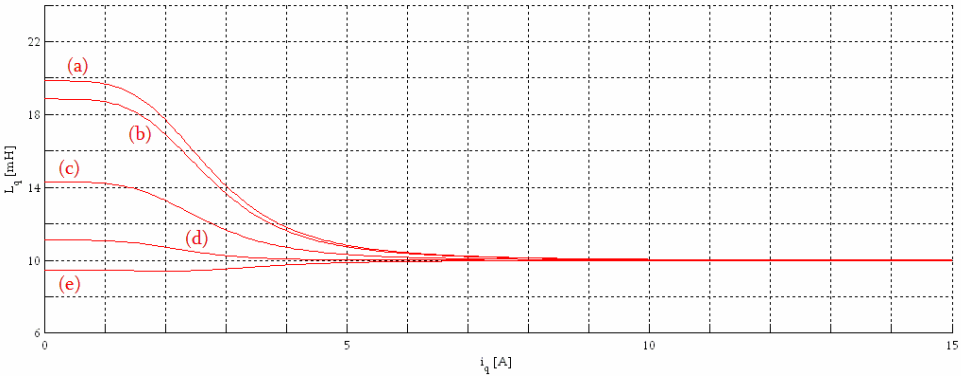

Figure III.9. L_q evolutions for different i_d values: i_d = 0 A (a), i_d = 1 A (b), i_d = 3 A (c), i_d = 5 A (d), i_d = 7 A (e).

TABLE III.1

A_0	B_0	C_0	D_0	B_1	C_1	D_1	C_q
0.0391	45.4	–12.9	1329	19.9	–13	795	0.0133
A_2	B_2	C_2	D_2	B_3	C_3	D_3	C_d
0.0100	0.571	0.0	58	0.825	0.0	63.8	0.0833

Therefore, taking into account the magnetic saturation effects, Eq. (III.17) cannot be assumed further, so it must be replaced by Eq. (III.65):

$$v^{(r)} = r \cdot i^{(r)} + \ell^{(r)} \cdot \frac{di^{(r)}}{dt} - \omega \cdot J \cdot \mathfrak{L}^{(r)} \cdot i^{(r)} \tag{III.65}$$

being:

$$\ell^{(r)} = \frac{\partial \lambda^{(r)}}{\partial i^{(r)}} = \begin{bmatrix} \frac{\partial \lambda_d}{\partial i_d} & \frac{\partial \lambda_d}{\partial i_q} \\ \frac{\partial \lambda_q}{\partial i_d} & \frac{\partial \lambda_q}{\partial i_q} \end{bmatrix} \tag{III.66}$$

Moreover, since Eq. (III.65) is non linear with reference to $i^{(r)}$, in order to obtain the discrete time model of the SRM it is assumed that the magnetic flux $\lambda^{(r)}$ varies linearly in the $[kT_s,(k+1)T_s]$ sampling time interval, as in Eq. (III.67):

$$\lambda^{(r)}(t) \cong \mathfrak{L}_k^{(r)} \cdot i_k^{(r)} + \ell_k^{(r)} \cdot \left(i^{(r)}(t) - i_k^{(r)} \right) \quad , \quad t \in \left[kT_s, (k+1)T_s \right] \tag{III.67}$$

Hence, by substituting Eq. (III.67) in Eq. (III.10), the following result can be achieved:

$$\frac{di^{(r)}}{dt} = A_k \cdot i^{(r)} + B_k \cdot v^{(r)} + C_k \tag{III.68}$$

being:

$$\begin{aligned} A_k &= \left(\ell_k^{(r)} \right)^{-1} \cdot \left(-r \cdot I + \omega \cdot J \cdot \ell_k^{(r)} \right) \\ B_k &= \left(\ell_k^{(r)} \right)^{-1} \\ C_k &= \omega \cdot \left(\ell_k^{(r)} \right)^{-1} \cdot J \cdot \left(\mathfrak{L}_k^{(r)} - \ell_k^{(r)} \right) \cdot i_k^{(r)} \end{aligned} \tag{III.69}$$

Furthermore, always assuming the rotor speed ω_m constant over the $[kT_s,(k+1)T_s]$ sampling time interval, equal to $\omega_{m,k}$, the discrete time model of the system can be obtained:

$$i_{k+1}^{(r)} = F_k \cdot i_k^{(r)} + \Delta_k + H_k \cdot \Delta T_k^{(r)} \tag{III.70}$$

where:

$$F_k = e^{A_k \cdot T_s} \quad , \quad \Delta_k = -A_k^{-1} \cdot \left(I - e^{A_k \cdot T_s}\right) \cdot C_k \quad , \quad H_k = e^{A_k \cdot \frac{T_s}{2}} \cdot B_k \cdot V \tag{III.71}$$

being $\Delta T_k^{(r)}$ the dq voltage pulse widths vector, as usually. Considering now the electromagnetic torque, now it must be expressed as follow:

$$T_{e,k+1} = \frac{3}{2} p \cdot \left(i_{k+1}^{(r)}\right)^T \cdot \mathcal{L}_{k+1}^{(r)} \cdot J \cdot i_{k+1}^{(r)} \tag{III.72}$$

Referring to the (i_d,i_q) plane, Eq. (III.72) defines the constant torque curves, which are not equilateral hyperbolas such as in the linear case. As a consequence, the minimum Joule losses locus is now the one depicted in Fig. III.10. Anyway, assuming the intersection point of the minimum Joule losses locus with the reference torque curve as reference, the optimal steady state condition can still be found.

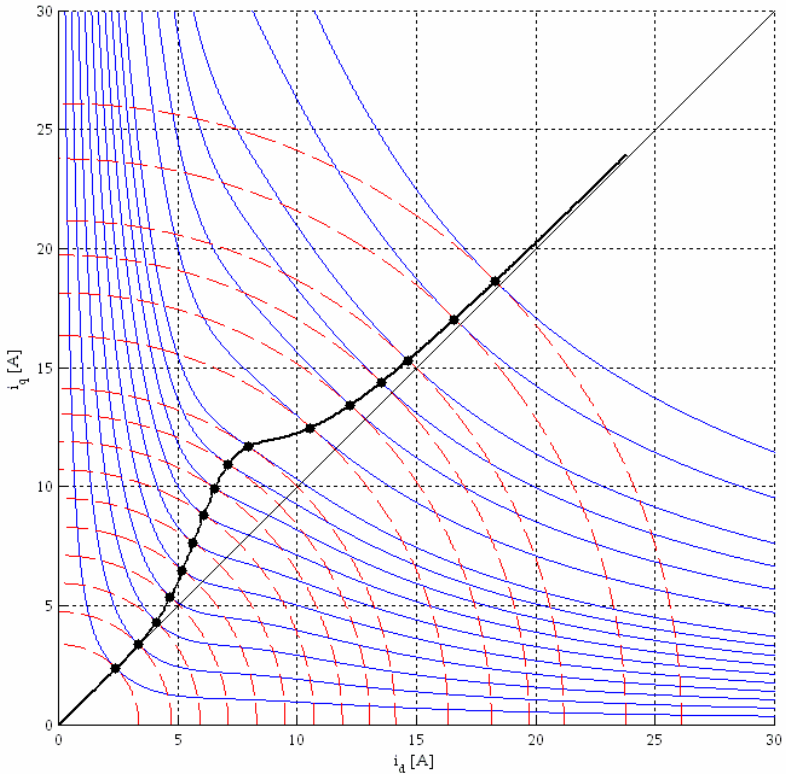

Figure III.10. Minimum Joule losses locus taking into account the magnetic saturation effects.

Considering the control algorithms previously described, some arrangements are required in order to take into account the magnetic saturation effects. First of all, Eq. (III.36) must be replaced by Eq. (III.73):

$$\begin{aligned} E_k &= \begin{bmatrix} e_{11,k} & e_{12,k} \\ e_{12,k} & e_{22,k} \end{bmatrix} = H_k^{-T} \cdot H_k^{-1} \quad , \quad e_k = \begin{bmatrix} e_{13,k} \\ e_{23,k} \end{bmatrix} = -H_k^{-T} \cdot H_k^{-1} \cdot \left(F_k \cdot i_k^{(r)} + \Delta_k \right) \\ e_{33,k} &= \left(F_k \cdot i_k^{(r)} + \Delta_k \right)^T \cdot H_k^{-T} \cdot H_k^{-1} \cdot \left(F_k \cdot i_k^{(r)} + \Delta_k \right) - T^2 \end{aligned} \tag{III.73}$$

Consequently, the centre of the voltage saturation ellipse $\mathfrak{S}_k$ must be expressed as follow:

$$c_k = F_k \cdot i_k^{(r)} + \Delta_k \tag{III.74}$$

Finally, although the constant torque curves are defined by Eq. (III.72), Eq. (III.42) can still be employed by replacing Eq. (III.43) with the following Eq. (III.75):

$$\begin{aligned} Q_k &= \begin{bmatrix} q_{11} & q_{12} \\ q_{12} & q_{22} \end{bmatrix} = \frac{1}{2} \left(\left(\ell_k^{(r)} \right)^T \cdot J - J \cdot \ell_k^{(r)} \right) \\ q_k &= \begin{bmatrix} q_{13} \\ q_{23} \end{bmatrix} = -\frac{1}{2} J \cdot \left(\wp_k^{(r)} - \ell_k^{(r)} \right) \cdot i_k^{(r)} \quad , \quad q_{33,k} = -\frac{2T_{e,k+1}}{3p} \end{aligned} \tag{III.75}$$

In fact, this last one is obtained by substituting Eq. (III.67) in Eq. (III.14), so it defines the torque hyperbola Ψ_{k+1} that well approximates $\mathfrak{I}_{k+1}$ in a neighbourhood of $(i_{d,k},i_{q,k})$, as shown in Fig. III.11 and III.12.

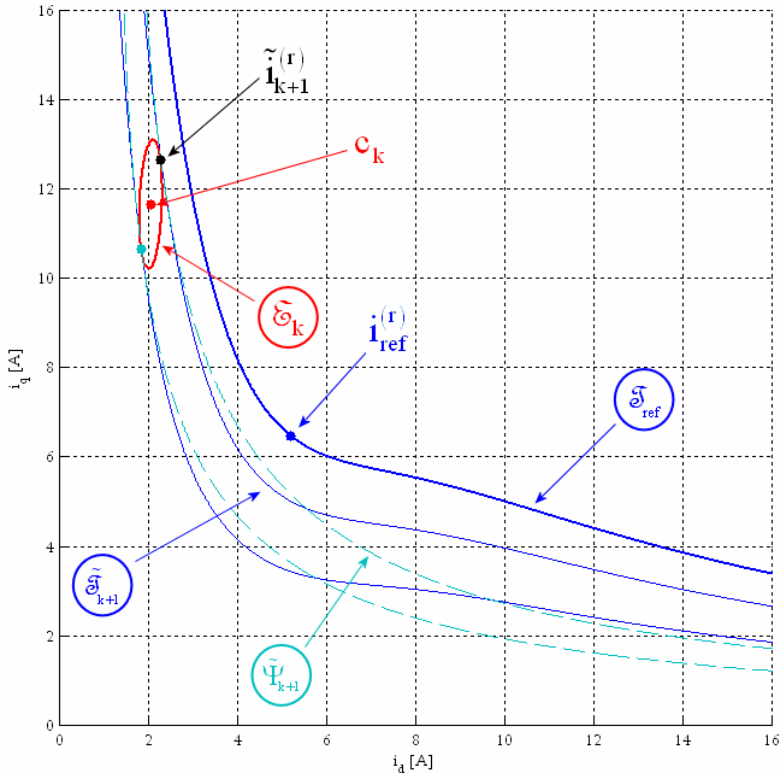

Figure III.11. Graphical representation of the POA when $T_e \neq T_{e,ref}$.

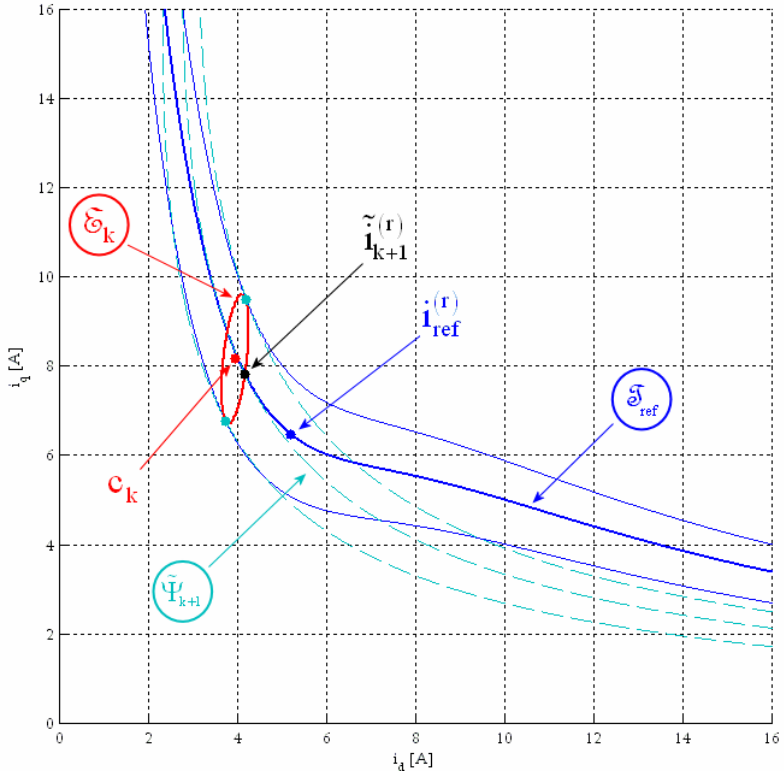

Figure III.12. Graphical representation of the POA when $T_e = T_{e,ref}$ and $i^{(r)} \neq i^{(r)}_{ref}$.

III.7. Simulations and Results

Several simulation studies were performed in the Matlab Simulink environment with the aim of comparing the performance obtained by the predictive control algorithms with those achieved by the traditional techniques. The drive block scheme employed in the simulations is depicted in Fig. III.13: the DC voltage source, the inverter and the SRM were modelled by using the SimPowerSystem Library, whereas the other control blocks were realized employing the Simulink Library.

TABLE III.2

PARAMETERS		UNITS
r	2	[Ω]
L_d	137.85	[mH]
L_q	57.15	[mH]
p	2	[-]
J_m	$1.94 \cdot 10^{-3}$	[Kgm^2]
D_m	0.012	[Nms]
T_s	100	[μs]
V	200	[V]

The first simulation study refers to the application of the traditional control strategy: this is performed both employing the PI current regulators (cases 1a and 2a) and the predictive control technique (cases 3a, 4a and 5a). The simulations parameters values are those reported in Table III.2, whereas the inverter switching frequency was set to 10 kHz in all the simulations performed. In cases 1a and 2a, the gains of the q-current PI regulator were set in order to have a bandwidth of 1 kHz, while those of the d-current one were determined in order to obtain a bandwidth equal to L_q/L_d kHz. Moreover, in case 2a, the feed forward compensation of the d-q cross coupling motional emfs was introduced. In case 3a, the voltage pulse widths vectors are computed by PTA and immediately applied.

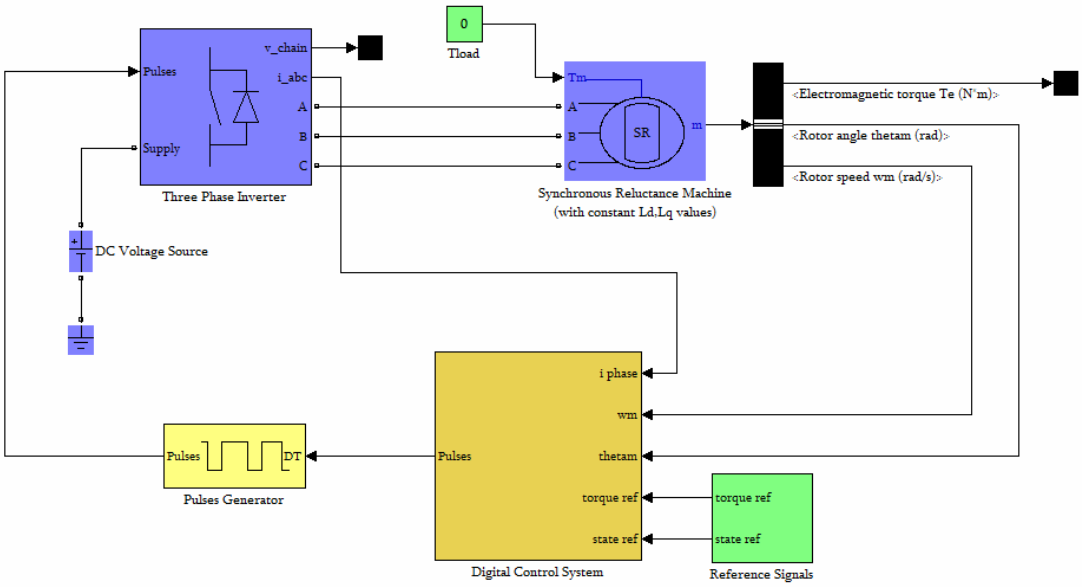

Figure III.13. Block Control Scheme of the Synchronous Reluctance Drive employed for the first two simulation studies.

Otherwise, in case 4a, their application is delayed by one sampling time interval. Finally, in case 5a, the predictive state observer was introduced in order to correctly postpone the application of the voltage pulse widths vectors to the next sampling time intervals.

Firstly, the simulations refer to the start up of the drive: starting from rest, the i_d reference value of 1.5 A is imposed, whereas $i_{q,ref}$ is set to zero. After 4 ms, $i_{q,ref}$ is increased to 5 A in order to achieve the reference torque value of about 1.81 Nm. The corresponding simulations results are depicted from Fig. III.14 through III.16.

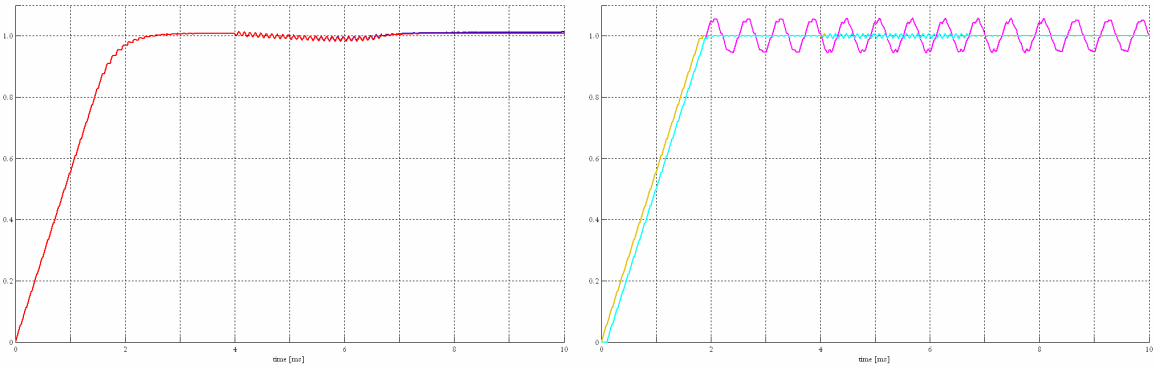

Figure III.14. i_d responses at start up (in p.u., i_d^* = 1.5 A): cases 1a (blue), 2a (red), 3a (gold), 4a (magenta) and 5a (cyan).

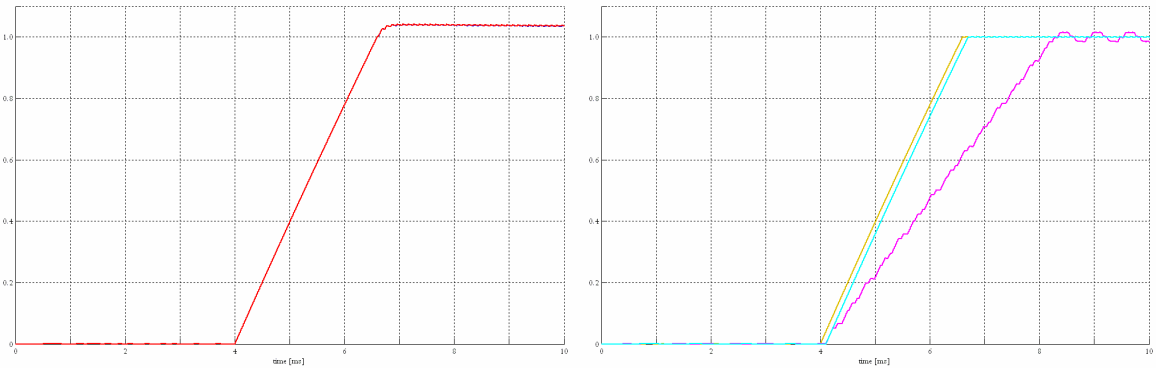

Figure III.15. i_q responses at start up (in p.u., i_q^* = 5 A): cases 1a (blue), 2a (red), 3a (gold), 4a (magenta) and 5a (cyan).

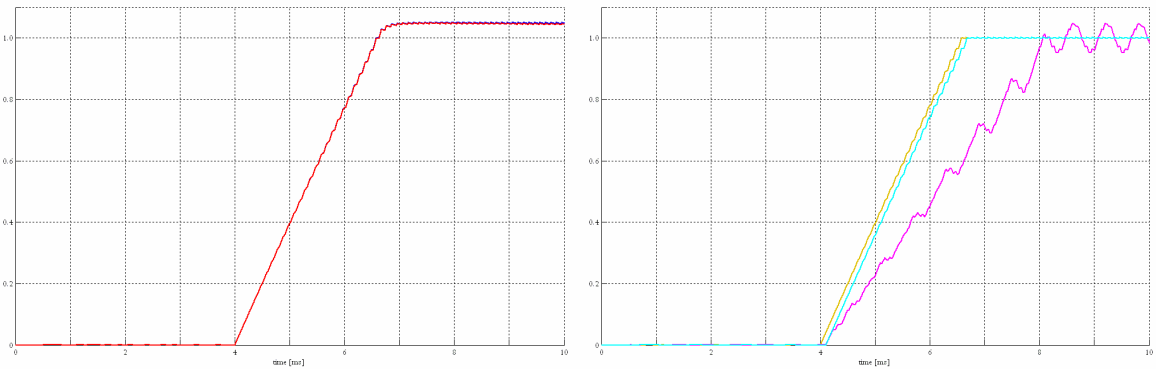

Figure III.16. Torque responses at start up (in p.u., T_e^* = 1.81 Nm): cases 1a (blue), 2a (red), cases 3a (gold), 4a (magenta) and 5a (cyan).

It can be seen that all the reference values are achieved at about the same time in all cases, excepted for case 4a, which is characterized by the worst torque and current responses. In fact, they are both affected by strong ripples due to the delayed application of the voltage pulses widths vectors. The current responses of cases 1a and 2a, which are almost the same due to the starting zero speed condition, are both affected by little overshoots. Furthermore, in these cases, the PI regulators are unable to keep i_d constant to $i_{d,ref}$ during the i_q transient response; this are better assured in cases 3a and 5a. Referring to these last ones, their current and torque responses differ each other only for the delay of one sampling time interval introduced by the predictive observer employed. Anyway, their performances are better than those achieved in cases 1a and 2a because no overshoots occur.

Finally, the (i_d,i_q) trajectories followed at the start up of the drive by all the control algorithms employed are shown in Fig. III.17. It can be noticed that they are partially overlapped during the i_d transient response. On the contrary, they become quite different each other during the i_q transient response, excepted for case 3a and 4a, which are characterized by the same current trajectory.

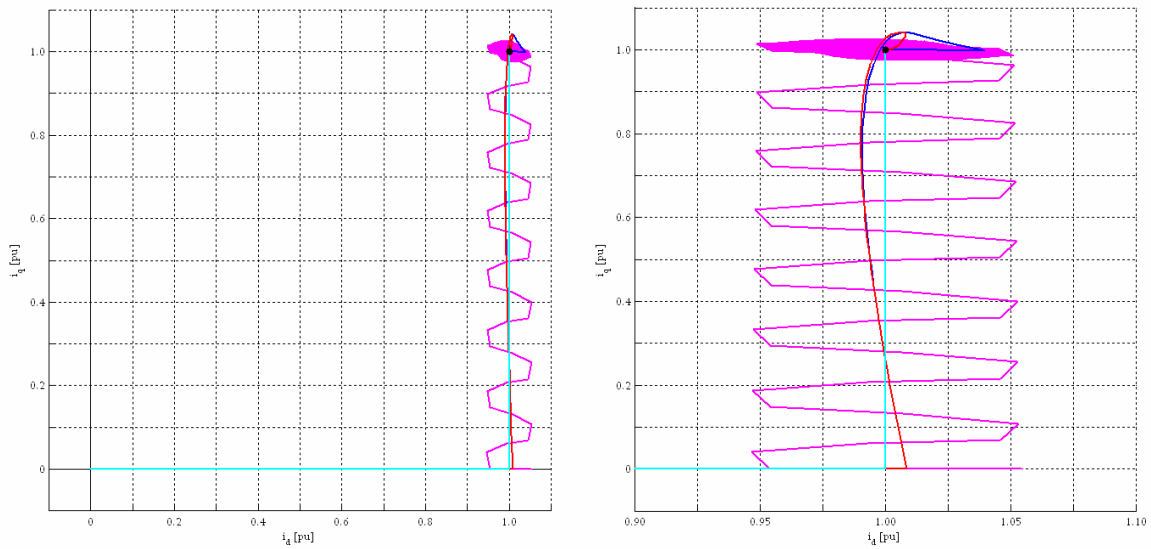

Figure III.17. All current trajectories followed at the start up of the drive: cases 1a (blue), 2a (red), 3a (gold), 4a (magenta) and 5a (cyan).

After that, the simulations refer to the torque inversion, which is performed at 1 s, after the achievement of the steady state speed value of about 151.3 rad/s. The corresponding simulations results are shown from Fig. III.18 through III.20.

It can be seen that the PI regulators employed in cases 1a and 2a do not prevent i_d to change during i_q inversion: in particular, referring to the case 2a, this drawback is less significant than in case 1a, due to the feed forward compensation of the d-q cross coupling motional emfs introduced.

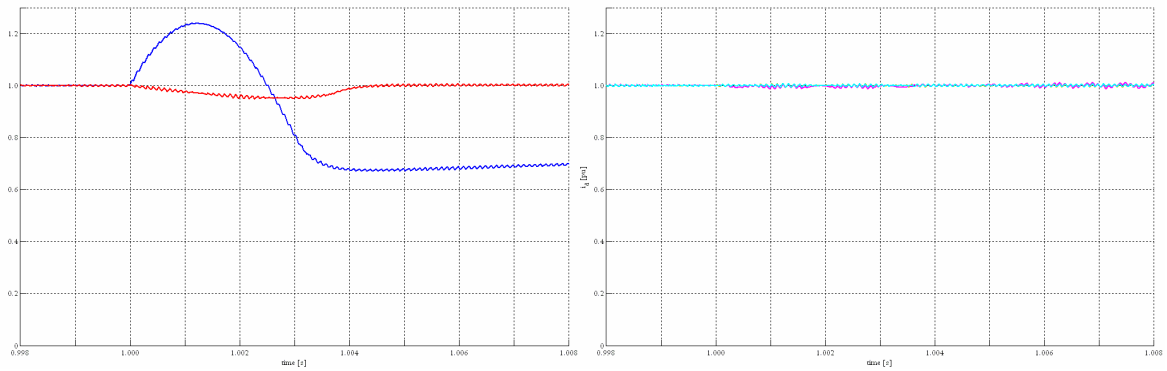

Figure III.18. i_d evolutions at torque inversion (in p.u., i_d^* = 1.5 A): cases 1a (blue), 2a (red), 3a (gold), 4a (magenta) and 5a (cyan).

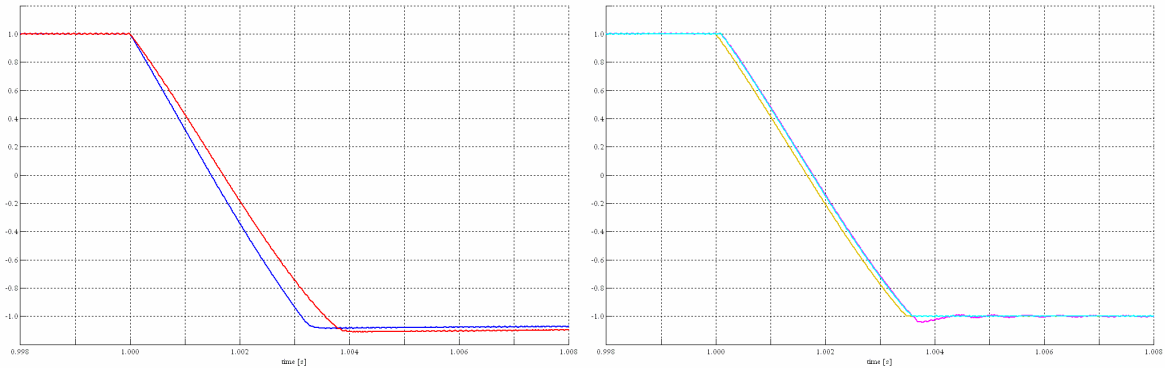

Figure III.19. i_q evolutions at torque inversion (in p.u., i_q^* = 5 A): cases 1a (blue), 2a (red), 3a (gold), 4a (magenta) and 5a (cyan).

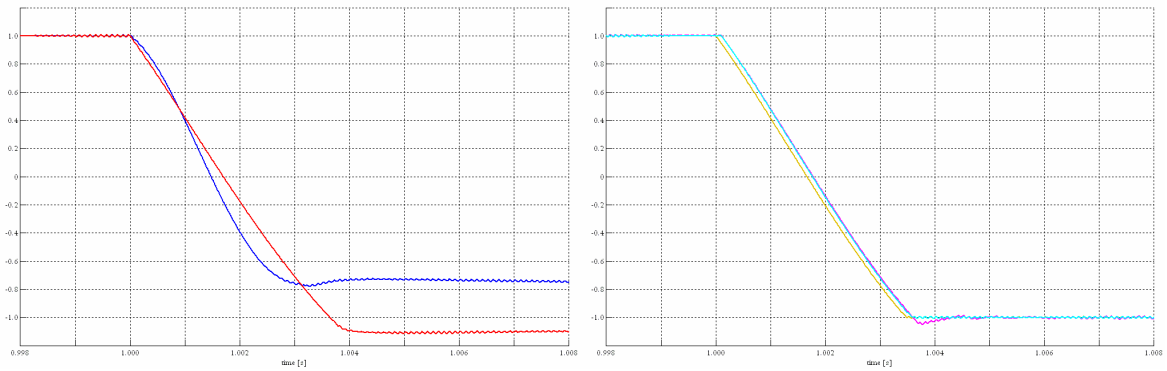

Figure III.20. Torque responses at inversion (in p.u., T_e^* = 1.81 Nm): cases 1a (blue), 2a (red), 3a (gold), 4a (magenta) and 5a (cyan).

As a consequence, in case 1a, the i_d variation strongly affects the torque response until it is driven to its reference value again. Anyway, the i_q responses obtained in both these cases are affected by overshoots, such as at the start up of the drive. Otherwise, better results are obtained in all the other cases: in fact, i_d is kept constant to its reference value during i_q transient response. However, in case 4a, a little overshoot on the i_q evolutions occurs.

In conclusion, all the (i_d,i_q) trajectories followed during the torque inversion are shown in Fig. III.21, whereas the results referred to all the simulation time are shown from Fig. III.22 through III.25. Since the results obtained in case 2a are better than those achieved in case 1a, this last one is not employed for the next simulations studies. In the same way, the predictive control algorithms employed in cases 4a and 5a are not considered further.

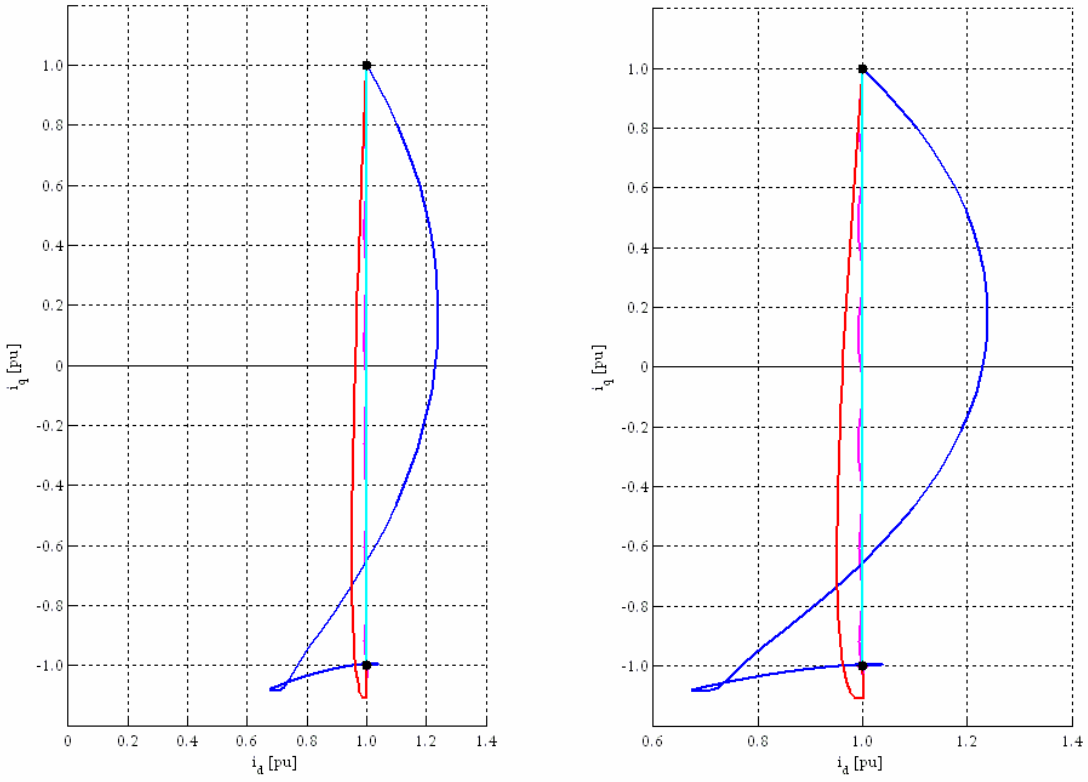

Figure III.21. All current trajectories followed at torque inversion: cases 1a (blue), 2a (red), 3a (gold), 4a (magenta) and 5a (cyan).

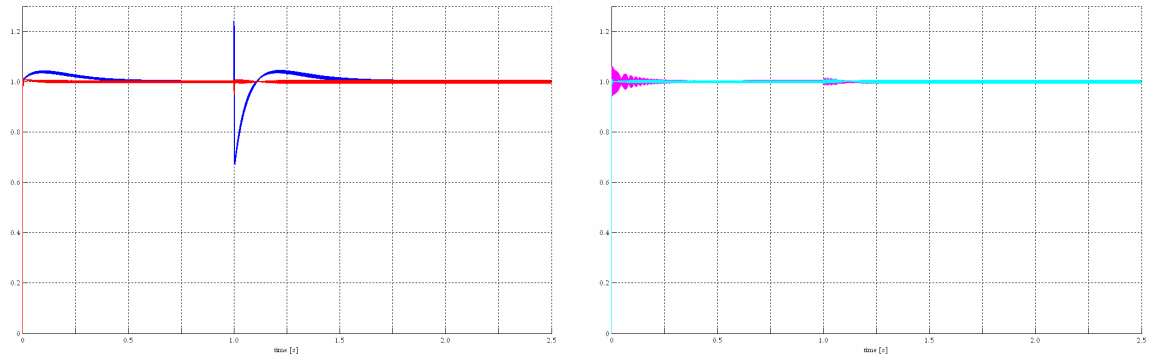

Figure III.22. i_d evolutions (in p.u., $i_d^* = 1.5$ A): cases 1a (blue), 2a (red), 3a (gold), 4a (magenta) and 5a (cyan).

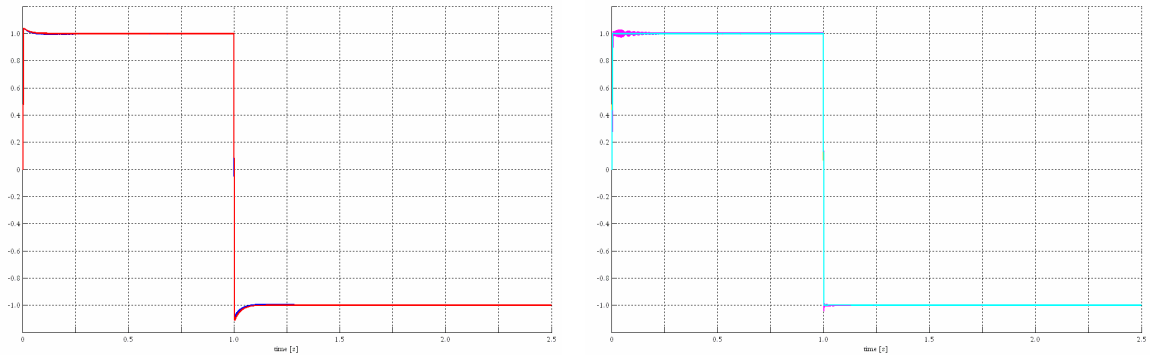

Figure III.23. i_q evolutions (in p.u., $i_q^* = 5$ A): cases 1a (blue), 2a (red), 3a (gold), 4a (magenta) and 5a (cyan).

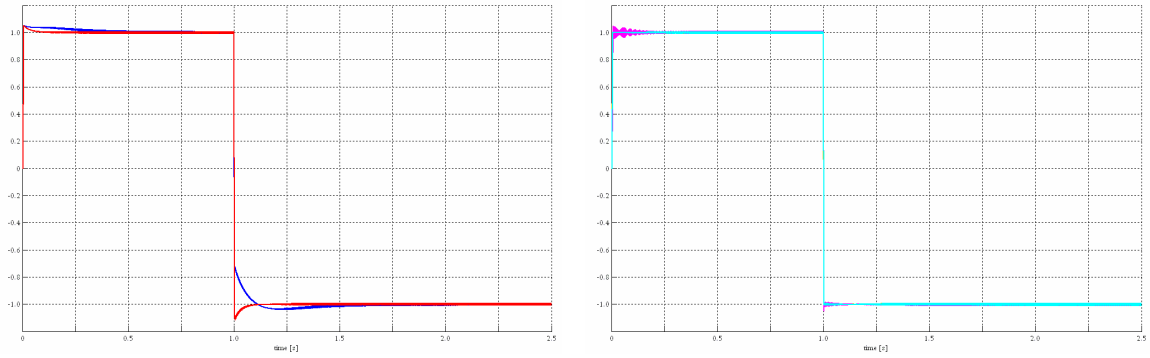

Figure III.24. Torque responses (in p.u., $T_e^* = 1.81$ Nm): cases 1a (blue), 2a (red), 3a (gold), 4a (magenta) and 5a (cyan).

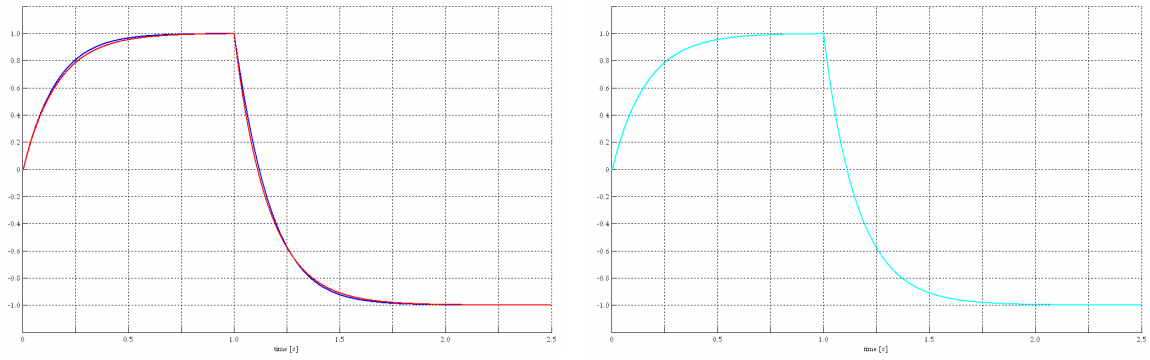

Figure III.25. Speed responses (in p.u., $\omega_m^* \approx 151.3$ rad/s): cases 1a (blue), 2a (red), 3a (gold), 4a (magenta) and 5a (cyan).

After that, a new simulation study is conducted with the aim of compared the results obtainable by the traditional control strategy with those achieved by employing the predictive optimal algorithm proposed in this work. The new simulations parameters values are reported in Table III.3, whereas the inverter switching frequency was still set to 10 kHz in all the simulations performed. Thus, the traditional control strategy was employed by means of PI current regulators (case 1b), whose bandwidths were set as in the previous simulation study. Moreover, the PTA (case 2b) was also applied, whereas a non optimal control strategy was performed by employing both PI current regulators (case 3b) and the PSA (case 4b). Finally, the torque transient optimization is carried out by the POA (case 5b).

TABLE III.3

PARAMETERS		UNITS
r	0.34	[Ω]
L_d	50	[mH]
L_q	14	[mH]
p	2	[-]
J_m	$7.041 \cdot 10^{-3}$	[Kgm^2]
D_m	0.0562	[Nms]
T_s	100	[μs]
V	300	[V]

First of all, the simulations refer to the drive response to a step reference torque of 10 Nm, starting from rest. The corresponding reference current values are chosen in order to reach the minimum Joule losses steady state condition available. The start up torque and currents responses of the drive are shown from Fig III.26 through III.28.

Firstly considering the traditional control algorithms, it can be seen that the employment of the predictive technique allows the achievement of better performances compared to those obtained by employing the traditional PI current regulators, as already pointed out in the previous simulation study. In fact, the i_d reference value is reached faster in case 2b than in 1b, determining the improvement of the torque response. Furthermore, in case 1b, both the currents and the torque responses are affected by little overshoots, which do not occur employing the PTA.

Considering now the other control strategies employed, it can be seen that they are all able to improve the performance of the drive with reference to the traditional control algorithms. Nevertheless, the results obtained employing the PI regulators (case 3b) are not as good as those achieved by the PSA employed in case 4b. In fact, in this last one, both the i_d and i_q reference values are reached faster than in case 3b, whose responses are also affected by little overshoots.

Anyway, the POA employed in case 5b allows the fastest achievement of the reference torque value compared to all the other cases. This best performance is obtained through

very high variation of the i_q current component, as highlighted in Fig. III.27. However, when the reference torque is achieved, i_q is gradually reduced until it reaches the same steady state value of the other cases considered.

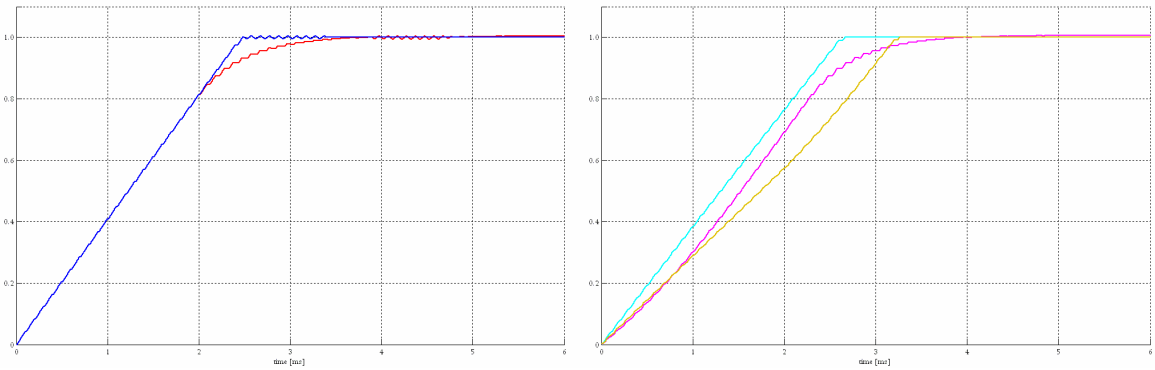

Figure III.26. i_d responses at start up (in p.u., $i_d^* \approx 8.46$ A): cases 1b (red), 2b (blue), cases 3b (magenta), 4b (cyan) and 5b (gold).

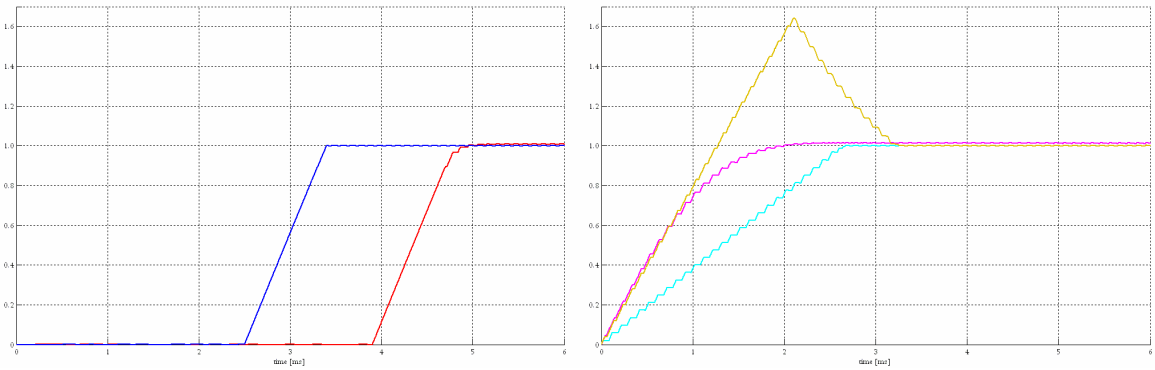

Figure III.27. i_q responses at start up (in p.u., $i_q^* \approx 10.94$ A): cases 1b (red), 2b (blue), cases 3b (magenta), 4b (cyan) and 5b (gold).

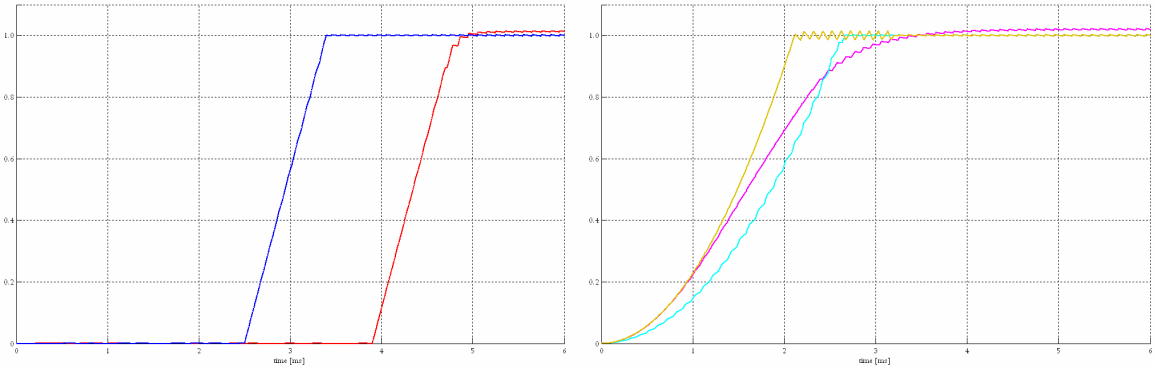

Figure III.28. Torque responses at start up (in p.u., $T_e^* = 10$ Nm): cases 1b (red), 2b (blue), cases 3b (magenta), 4b (cyan) and 5b (gold).

Finally, the trajectories followed by the current vector in all cases are shown in Fig. III.29, in which the reference torque hyperbola is also depicted. It can be seen that these trajectories are quite different each other, excepted for those of cases 1b and 2b, which are almost the same. In particular, it can be noticed that the POA employed in case 5b allows a good tracking of the reference torque hyperbola while it drives the current vector to its steady state value.

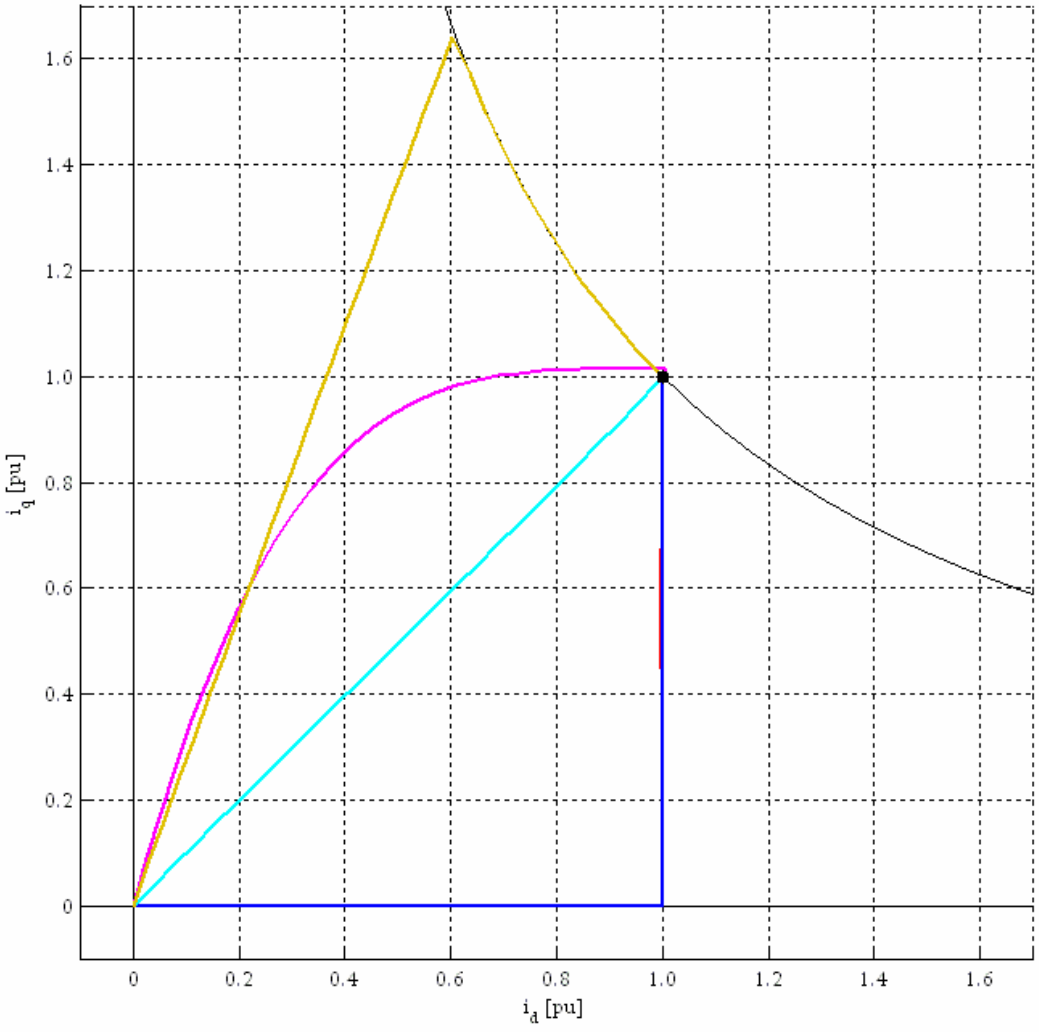

Figure III.29. All current trajectories followed at the start up of the drive: cases 1b (red), 2b (blue), 3b (magenta), 4b (cyan) and 5b (gold).

After 1.5 s, when the steady state speed is reached, the torque inversion is performed, so its reference value is set to -10 Nm. The corresponding simulation results are reported from Fig. III.30 through III.32, which highlight how all the currents and the torque responses achieved are very closed each other. However, those obtained in case 1b and 3b are slightly worse than the other ones.

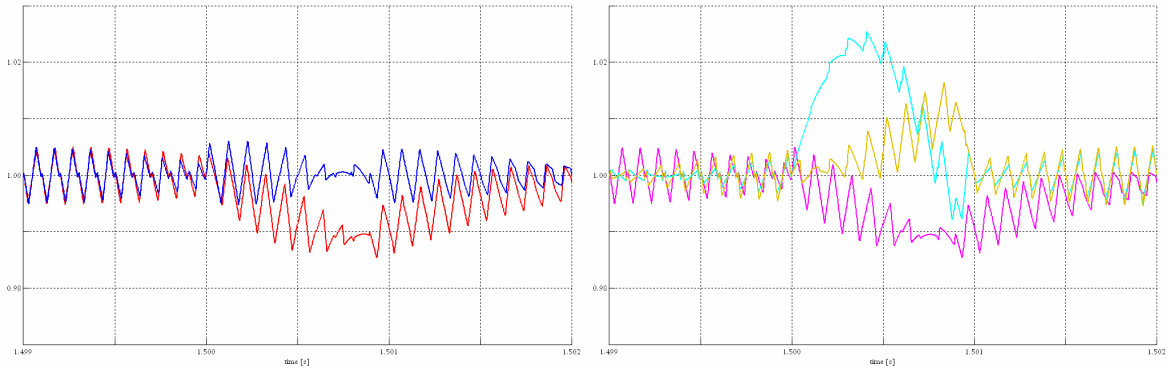

Figure III.30. i_d responses at torque inversion (in p.u., $i_d^* \approx 8.46$ A): cases 1b (red), 2b (blue), cases 3b (magenta), 4b (cyan) and 5b (gold).

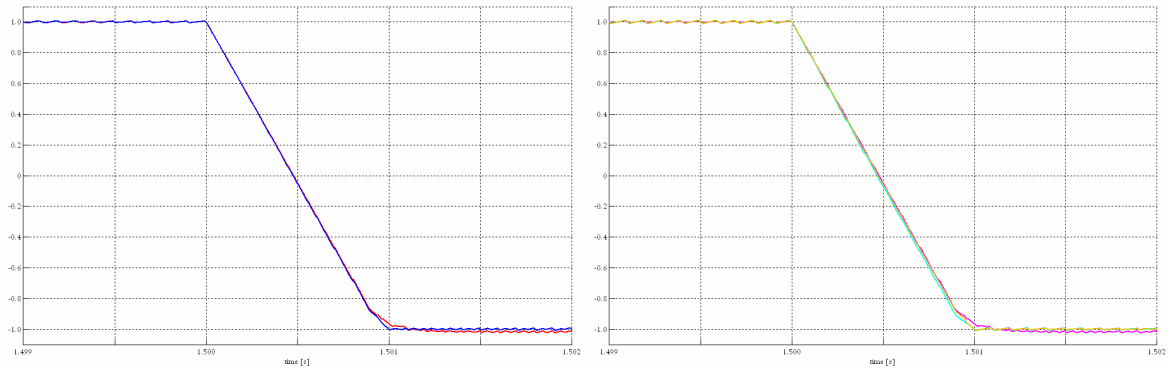

Figure III.31. i_q responses at torque inversion (in p.u., $i_q^* \approx 10.94$ A): cases 1b (red), 2b (blue), cases 3b (magenta), 4b (cyan) and 5b (gold).

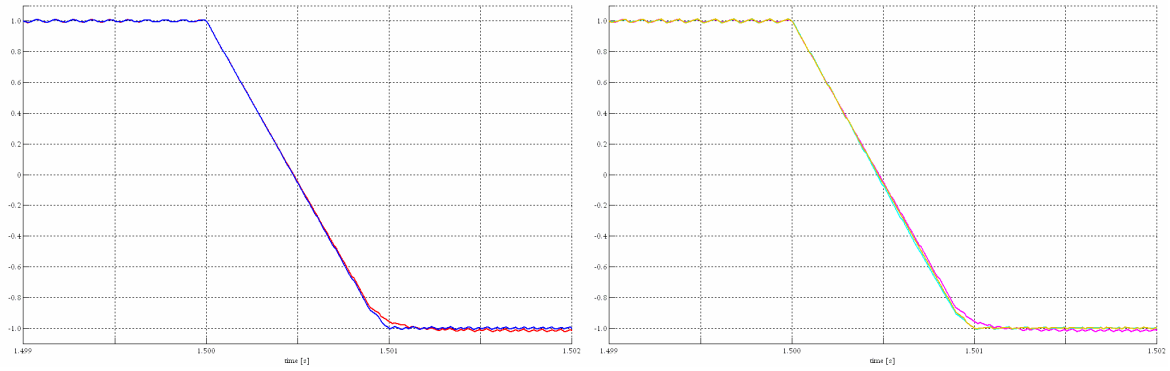

Figure III.32. Torque responses at inversion (in p.u., $T_e^* = 10$ Nm): cases 1b (red), 2b (blue), cases 3b (magenta), 4b (cyan) and 5b (gold).

Finally, all the current trajectories followed during torque inversion are depicted in Fig. III.33, whereas the results referred to all the simulation time are shown from Fig. III.34 through III.37.

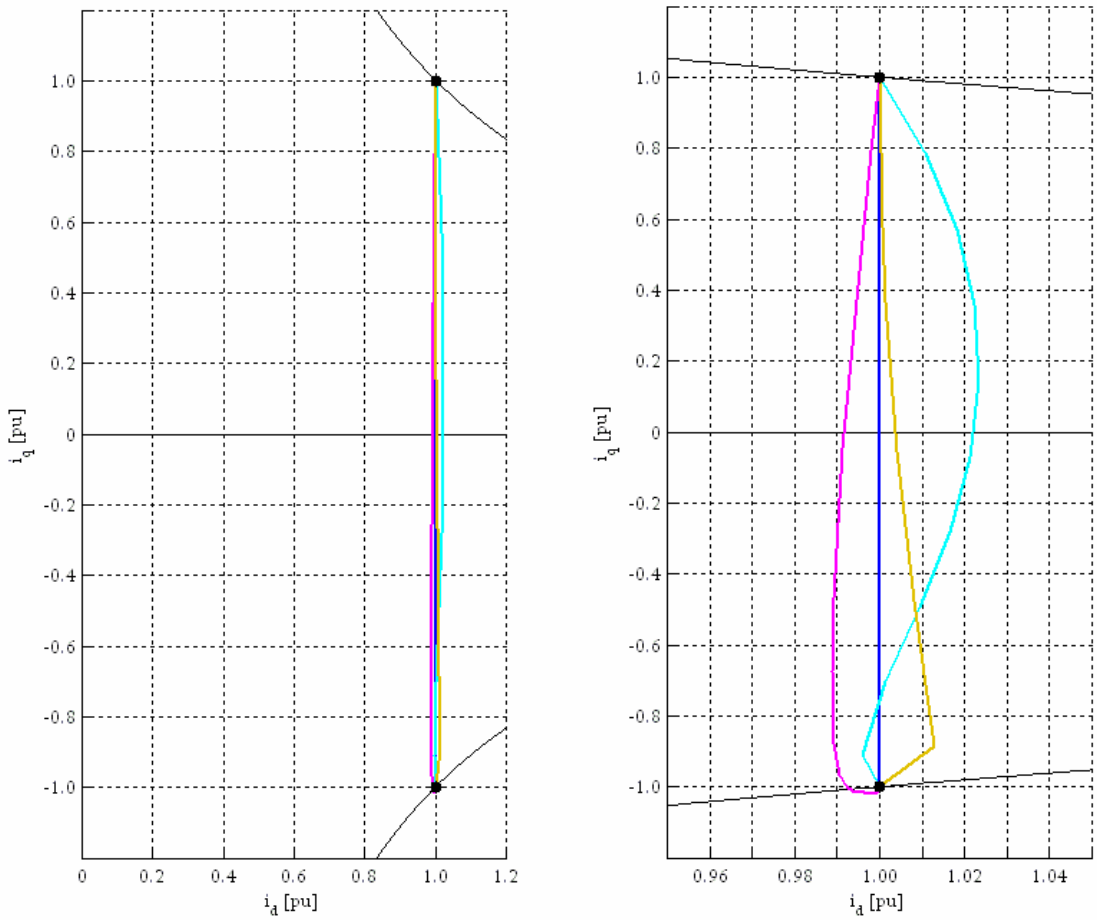

Figure III.33. All current trajectories followed at torque inversion: cases 1b (red), 2b (blue), 3b (magenta), 4b (cyan) and 5b (gold).

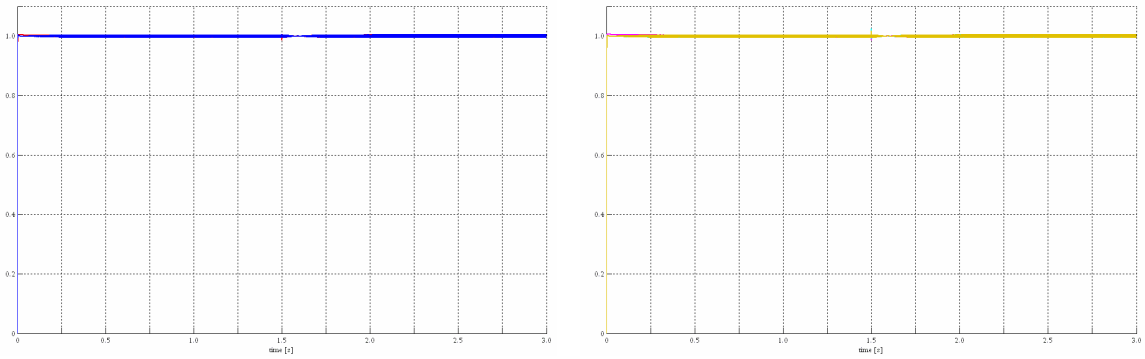

Figure III.34. i_d evolutions (in p.u., $i_d^* \approx 8.46$ A): cases 1b (red), 2b (blue), cases 3b (magenta), 4b (cyan) and 5b (gold).

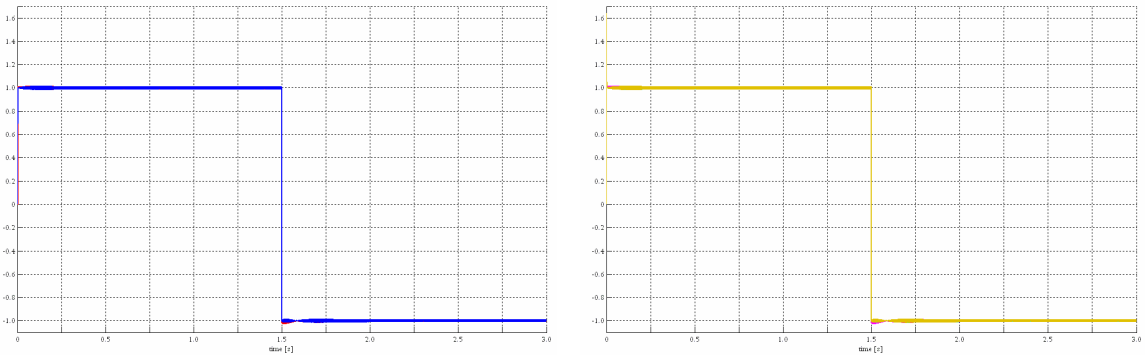

Figure III.35. i_q evolutions (in p.u., $i_q^* \approx 10.94$ A): cases 1b (red), 2b (blue), cases 3b (magenta), 4b (cyan) and 5b (gold).

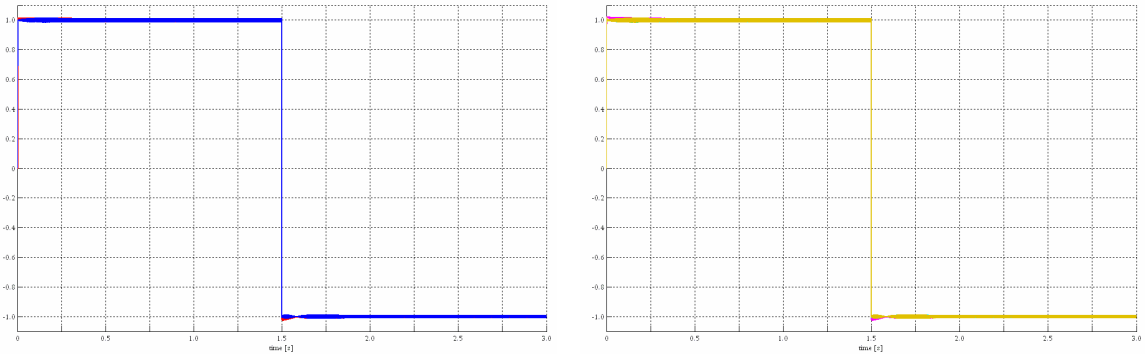

Figure III.36. Torque responses (in p.u., $T_e^* = 10$ Nm): cases 1b (red), 2b (blue), cases 3b (magenta), 4b (cyan) and 5b (gold).

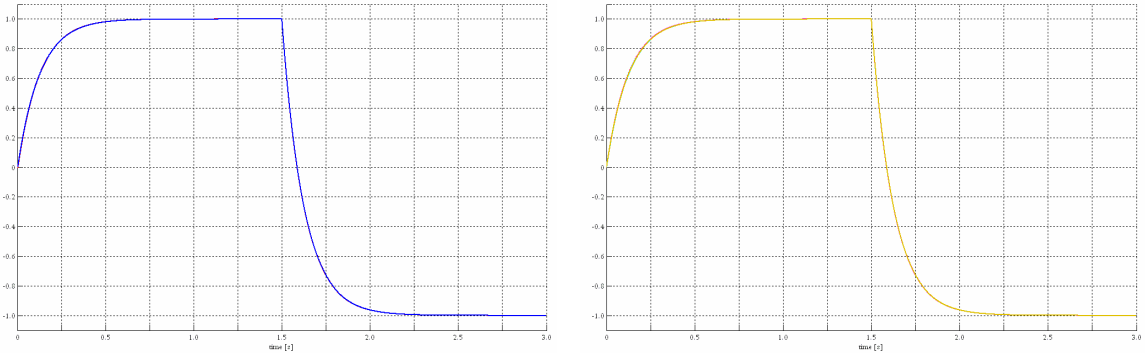

Figure III.37. Speed responses (in p.u., $\omega_m^* \approx 177.9$ rad/s): cases 1b (red), 2b (blue), cases 3b (magenta), 4b (cyan) and 5b (gold).

In conclusion, the last simulation study was conducted introducing the magnetic saturation effects. The drive block scheme employed in the simulations is depicted in Fig. III.38; in particular, the Simulink model of the SRM previously employed was properly modified basing upon Eq. (III.64). The new simulations parameters values are those reported in Table III.4, whereas the inverter switching frequency was set to 10 kHz in all the compared simulations, as usually.

TABLE III.4

PARAMETERS		UNITS
r	1	[Ω]
p	2	[-]
J_m	0.002	[Kgm^2]
D_m	0.04	[Nms]
T_s	100	[μs]
V	250	[V]

The control algorithms employed for this last simulation study are the same of the previous one. In particular, the gains of the PI current regulators employed in cases 1c and 3c were set in the same way as before, basing upon the mean value of L_d and L_q. Furthermore, the predictive algorithms employed in cases 2c, 4c and 5c were properly modified as mentioned in § III.6. Finally, the minimum Joule losses conditions, corresponding to the reference torque values imposed in the simulations, were determined by using an appropriate look-up table.

First of all, the simulations refer to the drive response to a step reference torque of 5 Nm, starting from rest. All the currents and torque responses obtained at the start up of the drive are shown from Fig III.39 through III.41.

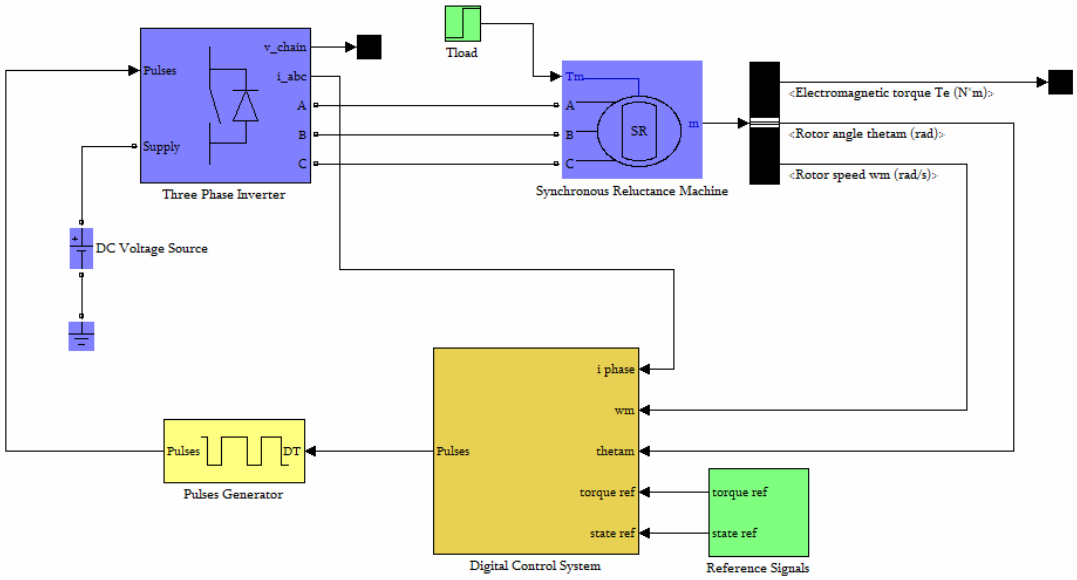

Figure III.38. Block Control Scheme of the Synchronous Reluctance Drive employed for the last simulation study.

Comparing the results achieved with those obtained in the previous simulation study, the most important difference occurs on the responses of case 1c; in fact, the unpredicted variations of both L_d and L_q prevent the control algorithm to keep i_d constant during the i_q transient response, even at zero speed operation. As a consequence, a bigger overshoot on the torque response occurs, compared to that obtained in case 1b.

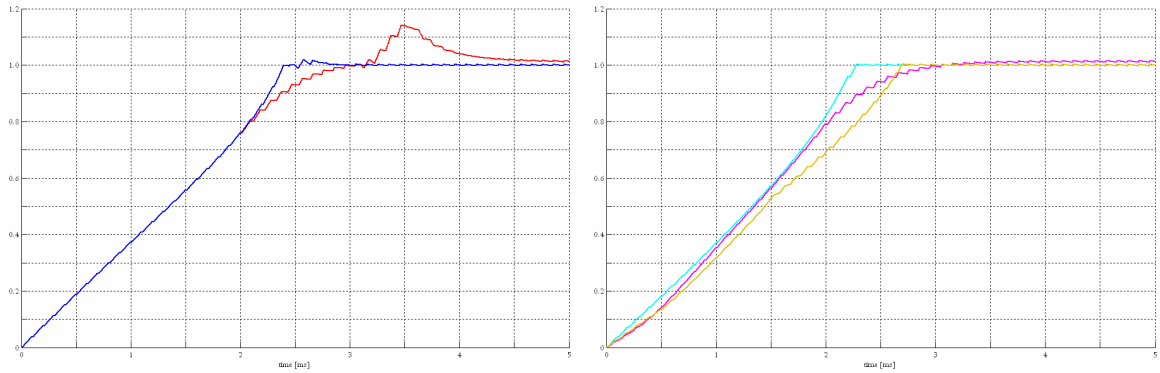

Figure III.39. i_d responses at start up (in p.u., $i_d^* \approx 5.19$ A): cases 1c (red), 2c (blue), 3c (magenta), 4c (cyan) and 5c (gold).

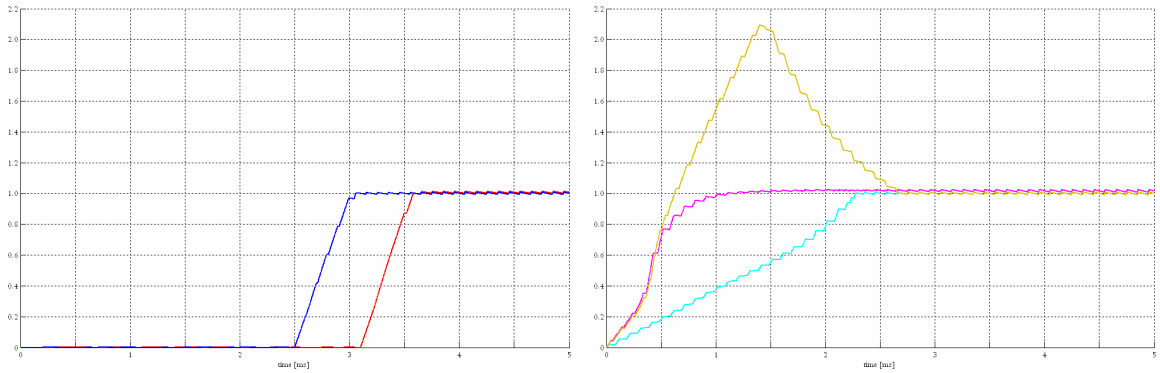

Figure III.40. i_q responses at start up (in p.u., $i_q^* \approx 6.47$ A): cases 1c (red), 2c (blue), 3c (magenta), 4c (cyan) and 5c (gold).

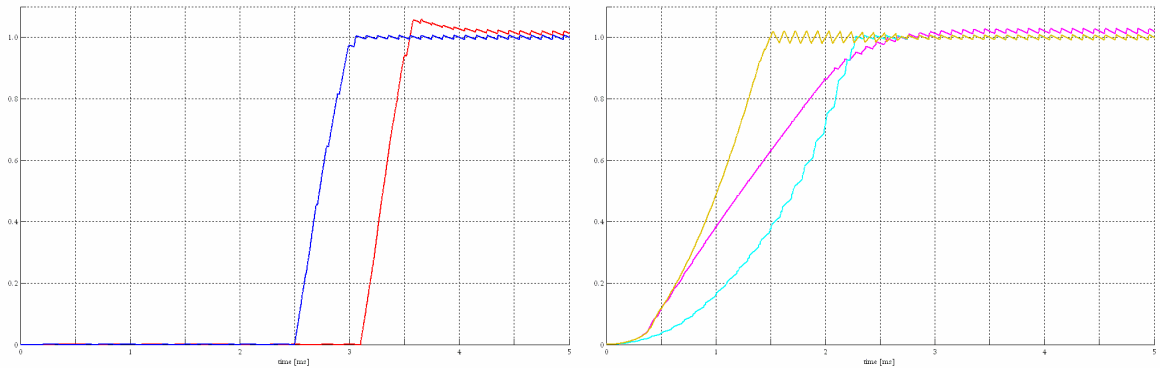

Figure III.41. Torque responses at start up (in p.u., $T_e^* = 5$ Nm): cases 1c (red), 2c (blue), 3c (magenta), 4c (cyan) and 5c (gold).

Otherwise, all the results achieved by the predictive algorithms employed in cases 2c, 4c and 5c are not badly affected by magnetic saturation effects. In fact, these ones can be successfully predicted and, hence, properly compensated. In particular, referring to the current vector trajectories depicted in Fig. III.42, it can be noticed that the tracking of the reference torque curve performed by the POA in case 5c is as good as that achieved in case 5b.

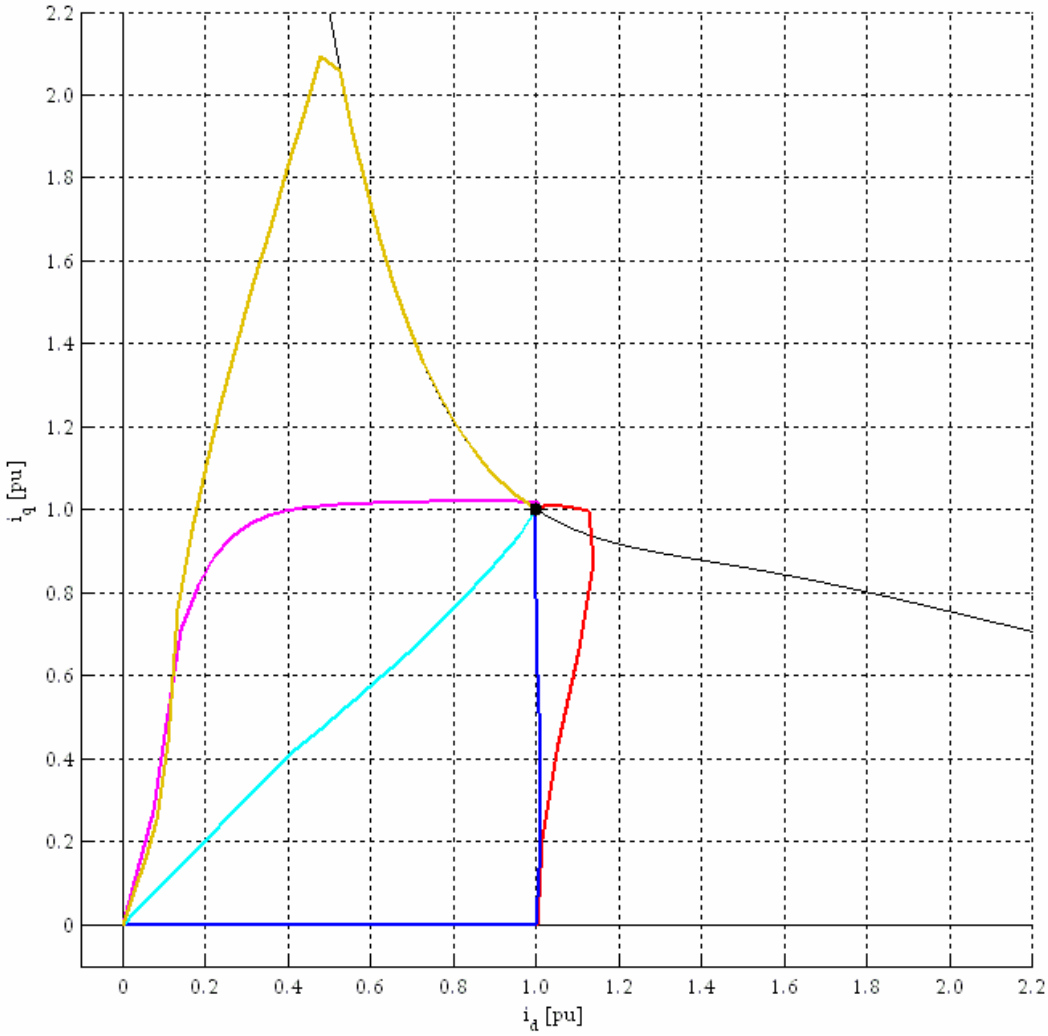

Figure III.42. All current trajectories followed at the start up of the drive: cases 1c (red), 2c (blue), 3c (magenta), 4c (cyan) and 5c (gold).

After 0.5 s, when the steady state speed value of about 75 rad/s is reached, a torque inversion is performed. The corresponding simulations results, depicted from Fig. III.43 through III.46, show that the differences among the simulated cases are less significant than at the start up of the drive, but more evident compared to those achieved in the previous simulation study.

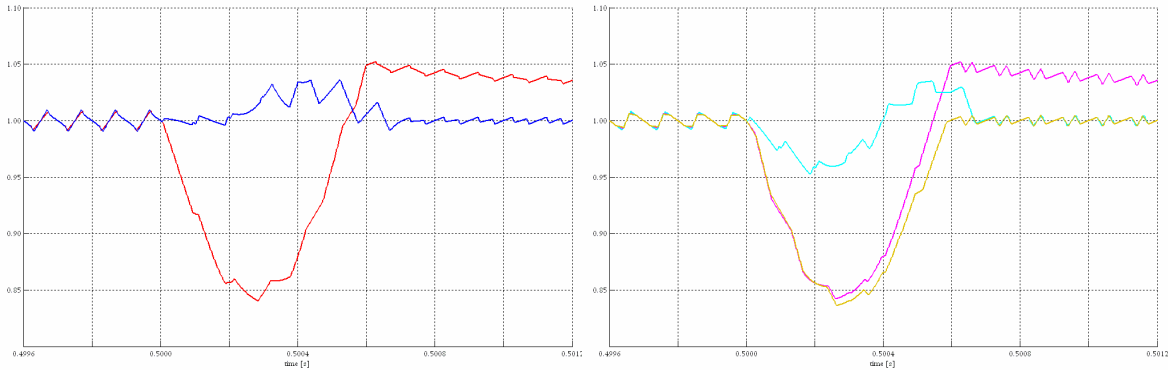

Figure III.43. i_d responses at the first torque inversion (in p.u., $i_d^* \approx 5.19$ A): cases 1c (red), 2c (blue), 3c (magenta), 4c (cyan) and 5c (gold).

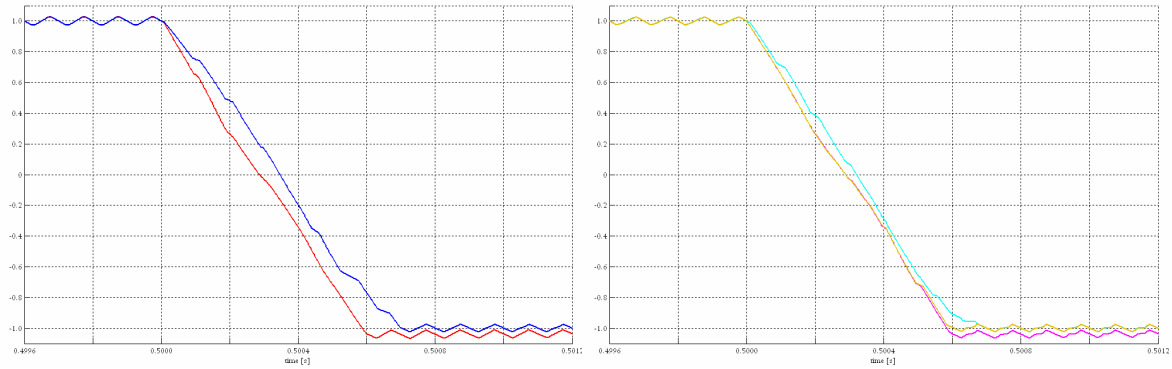

Figure III.44. i_q responses at the first torque inversion (in p.u., $i_q^* \approx 6.47$ A): cases 1c (red), 2c (blue), 3c (magenta), 4c (cyan) and 5c (gold).

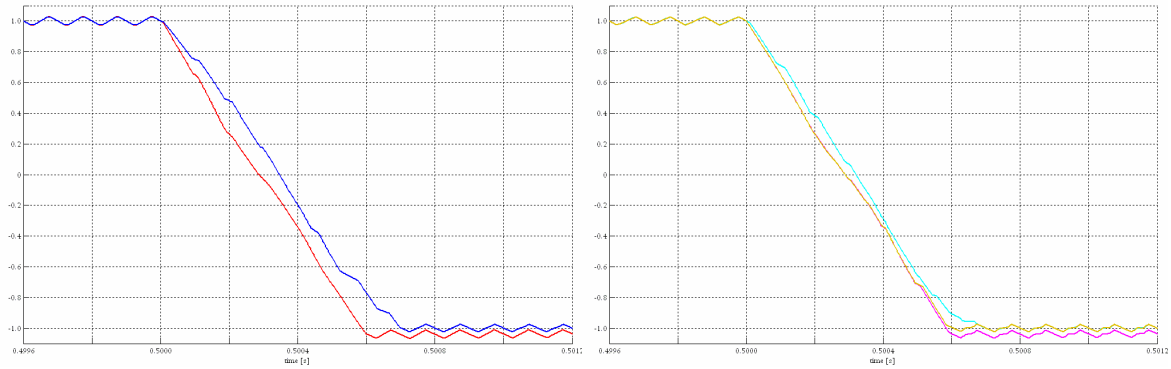

Figure III.45. First torque inversion (in p.u., $T_e^* = 5$ Nm): cases 1c (red), 2c (blue), 3c (magenta), 4c (cyan) and 5c (gold).

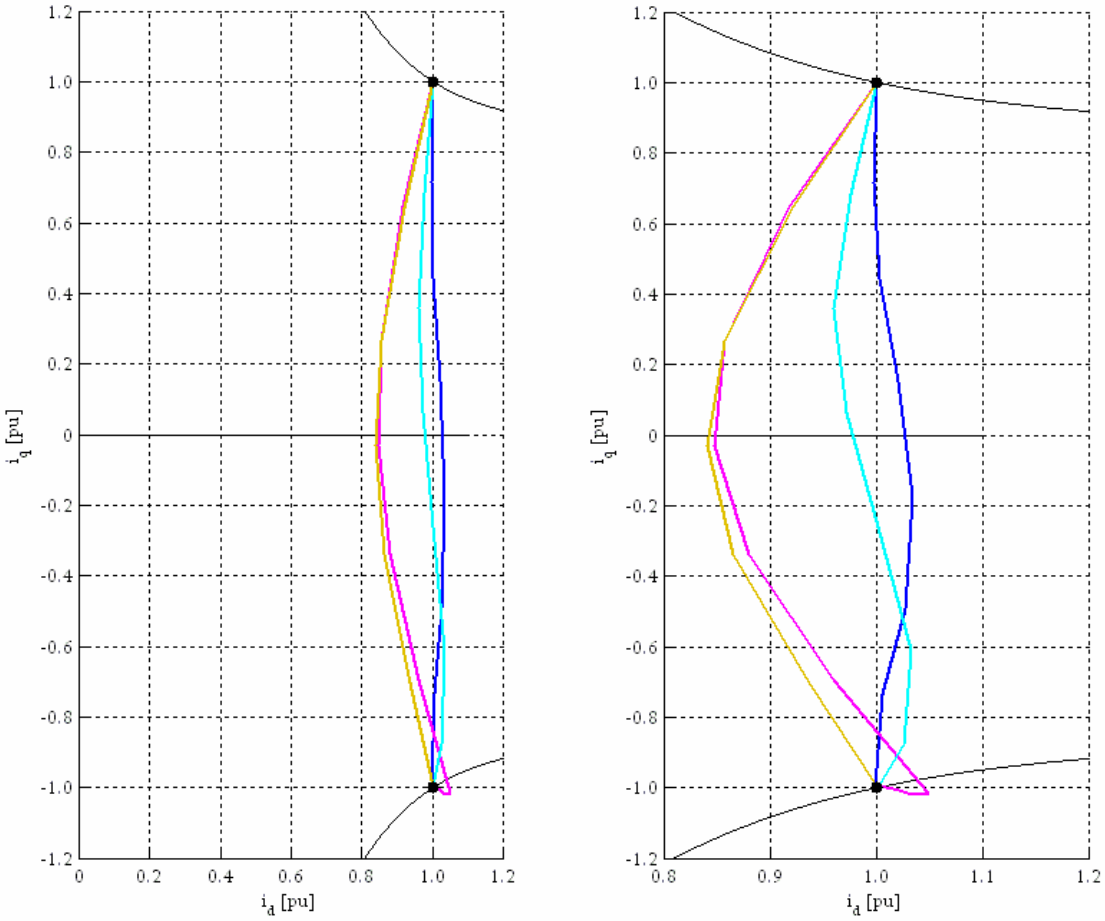

Figure III.46. All current trajectories followed at the first torque inversion: cases 1c (red), 2c (blue), 3c (magenta), 4c (cyan) and 5c (gold).

In particular, the performances achieved in case 2c and 4c become worse than those of cases 1c and 3c. However, these last ones are still affected by little overshoots, which do not occur by employing the predictive control algorithms. Anyway, the best performance is still obtained by employing the POA of case 5c.

After 1.0 s, the reference torque is set to 5 Nm again, in order to achieve the same steady state speed value of 75 rad/s reached at 0.5 s. The corresponding simulations responses, shown from Fig. III.46 through III.49, are very similar to the previous ones, so they are not discussed further.

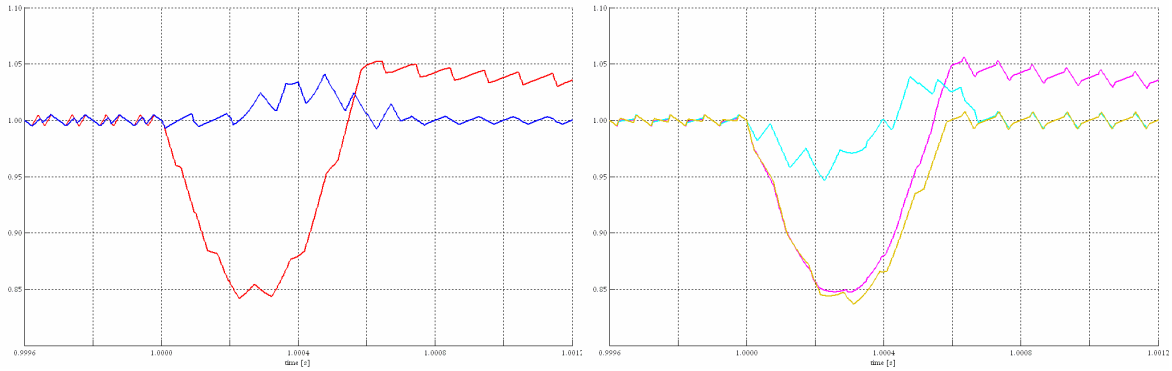

Figure III.47. i_d responses at the second torque inversion (in p.u., $i_d^* \approx 5.19$ A): cases 1c (red), 2c (blue), 3c (magenta), 4c (cyan) and 5c (gold).

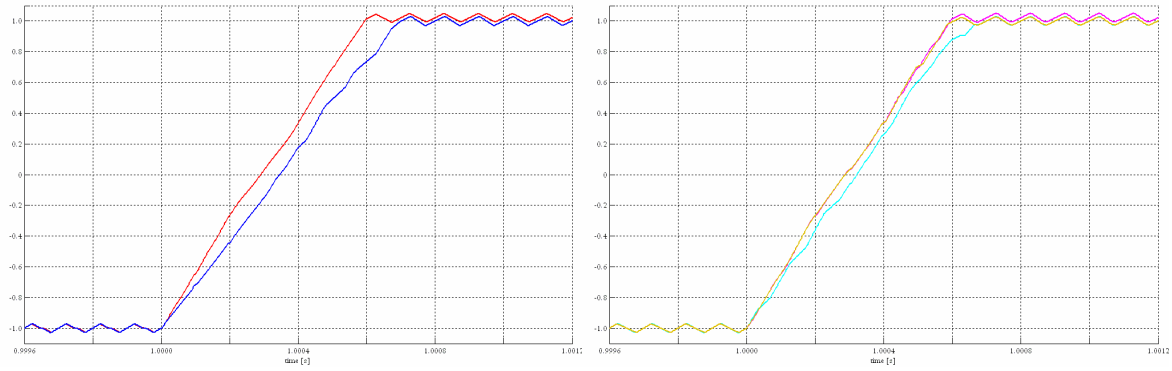

Figure III.48. i_q responses at the second torque inversion (in p.u., $i_q^* \approx 6.47$ A): cases 1c (red), 2c (blue), 3c (magenta), 4c (cyan) and 5c (gold).

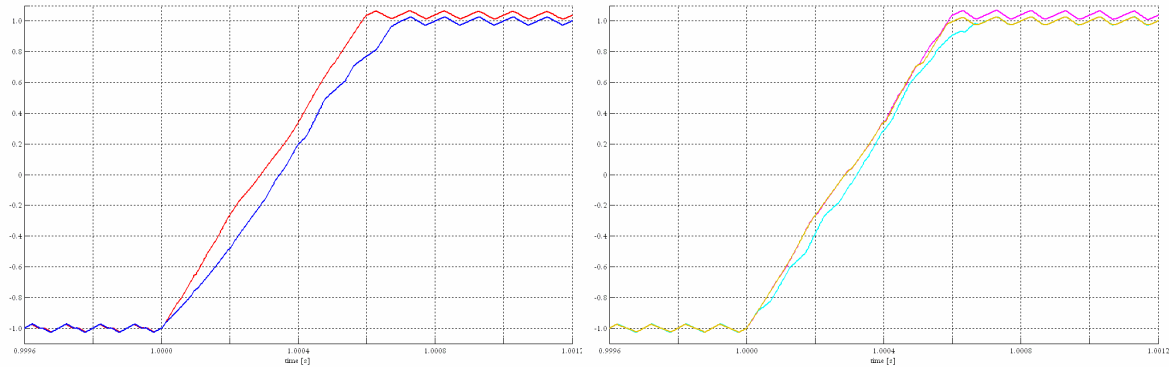

Figure III.49. Second torque inversion (in p.u., $T_e^* = 5$ Nm): cases 1c (red), 2c (blue), 3c (magenta), 4c (cyan) and 5c (gold).

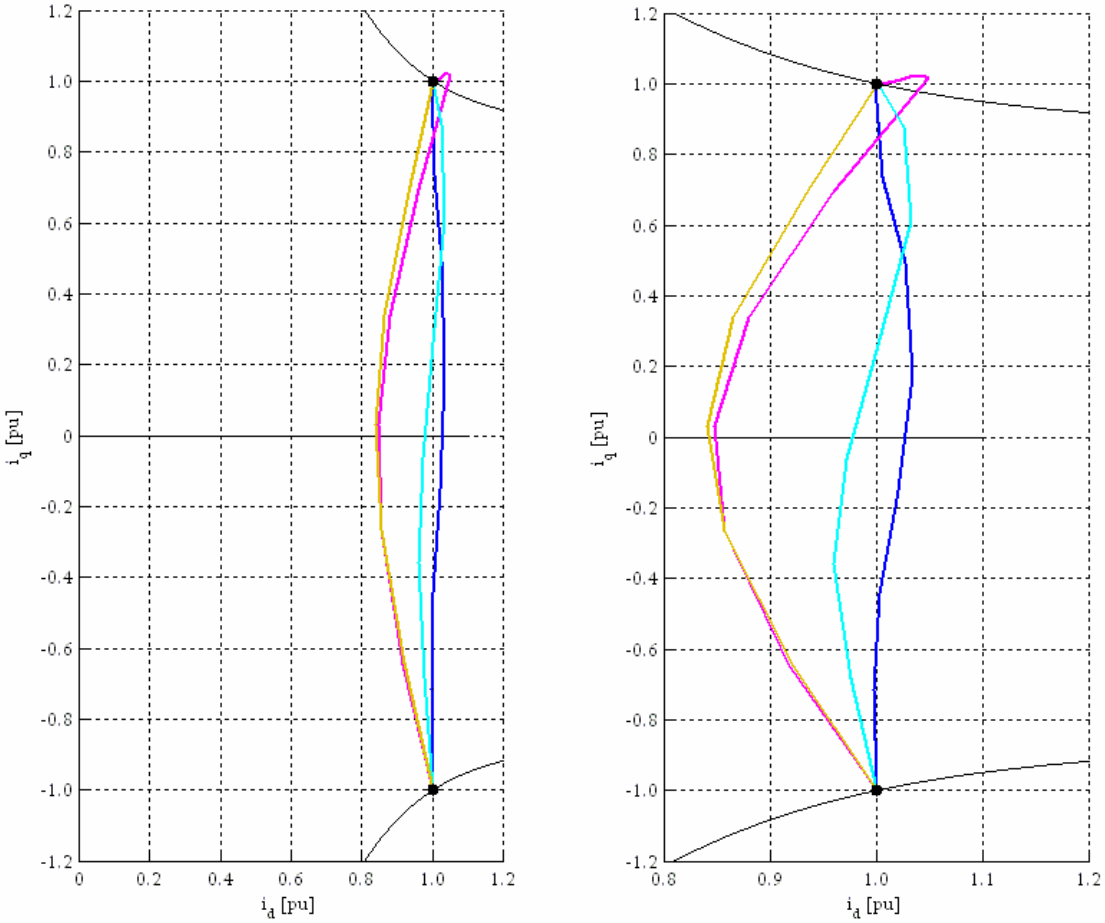

Figure III.50. All current trajectories followed at the second torque inversion: cases 1c (red), 2c (blue), 3c (magenta), 4c (cyan) and 5c (gold).

After 1.5 s, a load torque of 5 Nm is applied and the reference torque value is simultaneously set to 10 Nm. The simulation results obtained are reported from Fig. III.50 through III.53. In cases 1c and 2c, the reference currents values are different from those of the other cases (3c, 4c and 5c), due to the constant i_d constraint imposed by the traditional control strategy; as a consequence, the minimum Joule losses condition cannot be assured further.

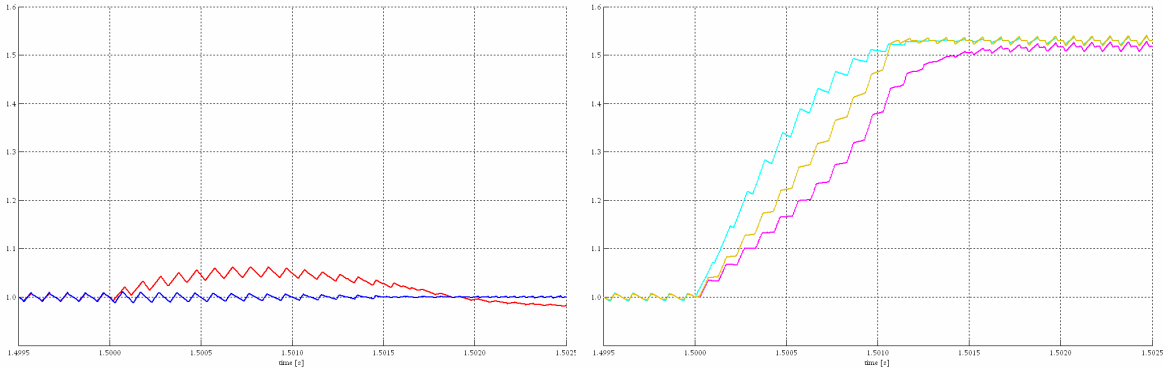

Figure III.51. i_d responses at step reference torque variation (in p.u., $i_d^* \approx 5.19$ A): cases 1c (red), 2c (blue), 3c (magenta), 4c (cyan) and 5c (gold).

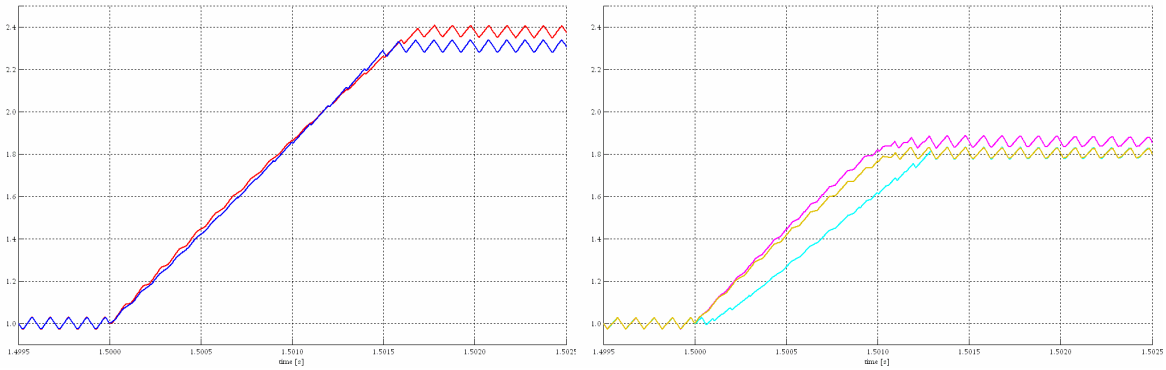

Figure III.52. i_q responses at step reference torque variation (in p.u., $i_q^* \approx 6.47$ A): cases 1c (red), 2c (blue), 3c (magenta), 4c (cyan) and 5c (gold).

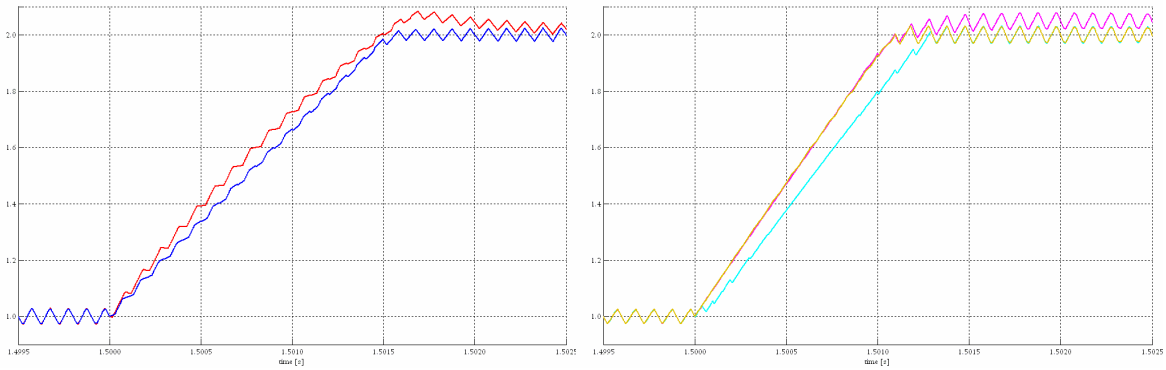

Figure III.53. Torque responses at step reference torque variation (in p.u., $T_e^* = 5$ Nm): cases 1c (red), 2c (blue), 3c (magenta), 4c (cyan) and 5c (gold).

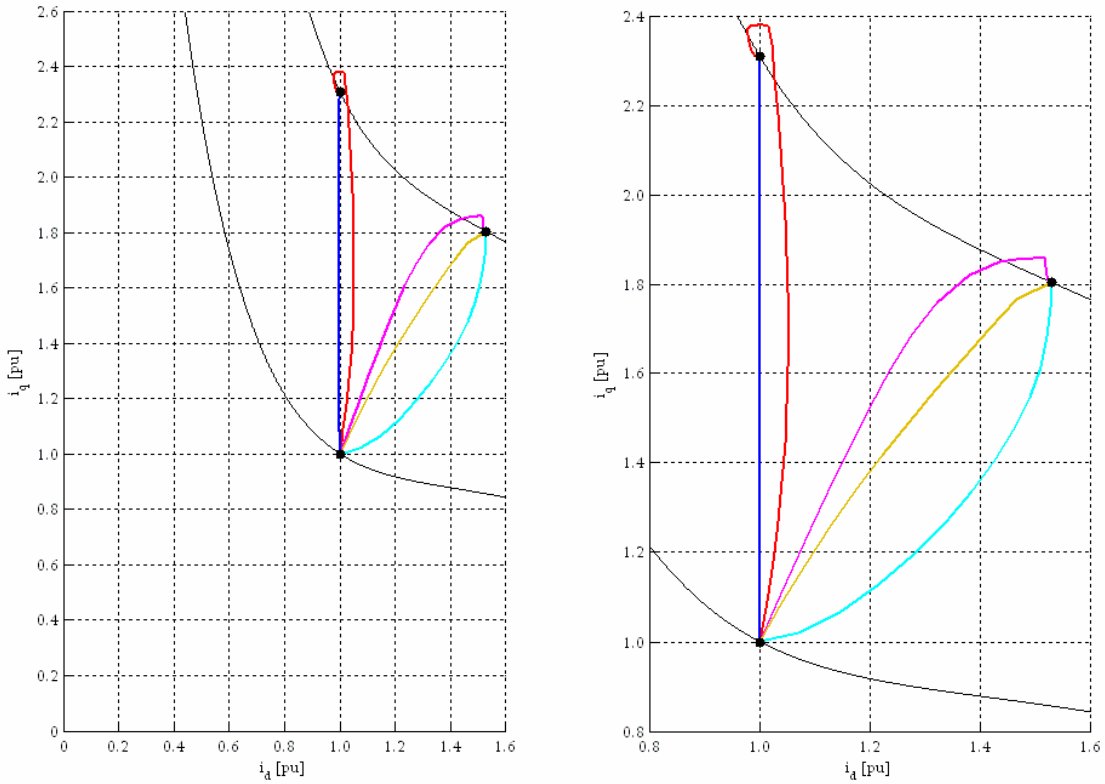

Figure III.54. All current trajectories followed at step reference torque variation: cases 1c (red), 2c (blue), 3c (magenta), 4c (cyan) and 5c (gold).

Furthermore, employing the traditional control strategy, the reference torque value is achieved slower than in the other cases. Moreover, in case 1c and 3c, the currents and torque responses are affected by little overshoot, as usually.

In conclusion, the results referred to all the simulation time are shown from Fig. III.54 through III.56, whereas the speed responses are depicted in Fig. III.57.

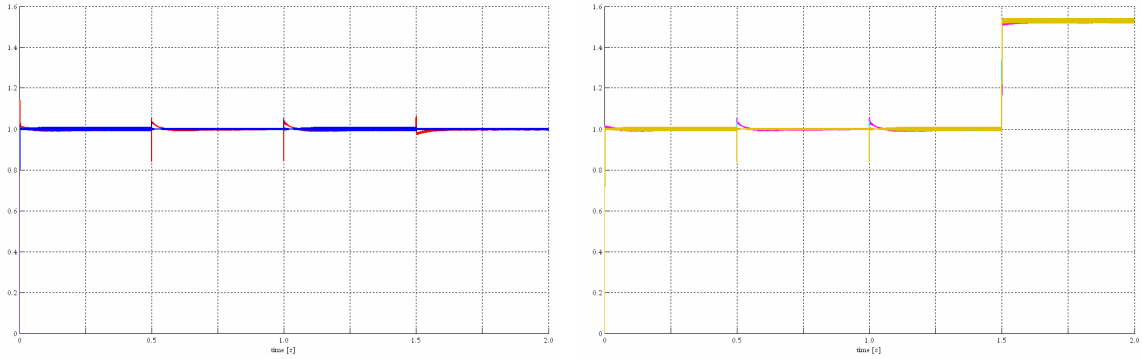

Figure III.55. i_d evolutions (in p.u., $i_d^* \approx 5.19$ A): cases 1c (red), 2c (blue), 3c (magenta), 4c (cyan) and 5c (gold).

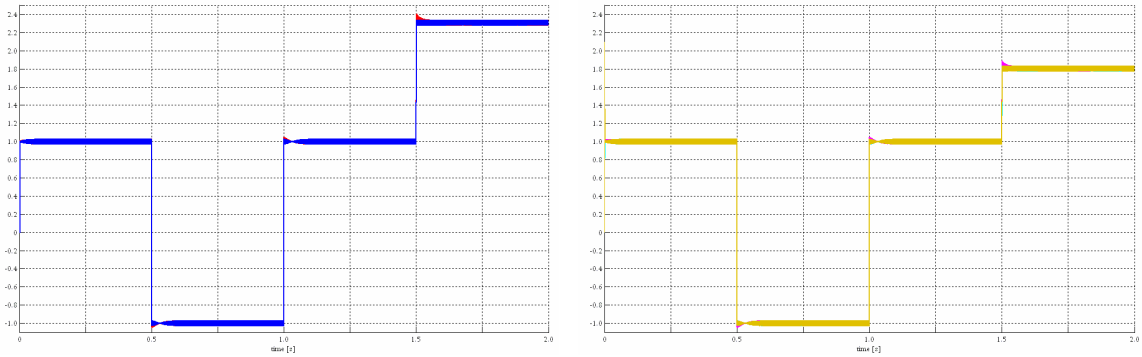

Figure III.56. i_q evolutions (in p.u., $i_q^* \approx 6.47$ A): cases 1c (red), 2c (blue), 3c (magenta), 4c (cyan) and 5c (gold).

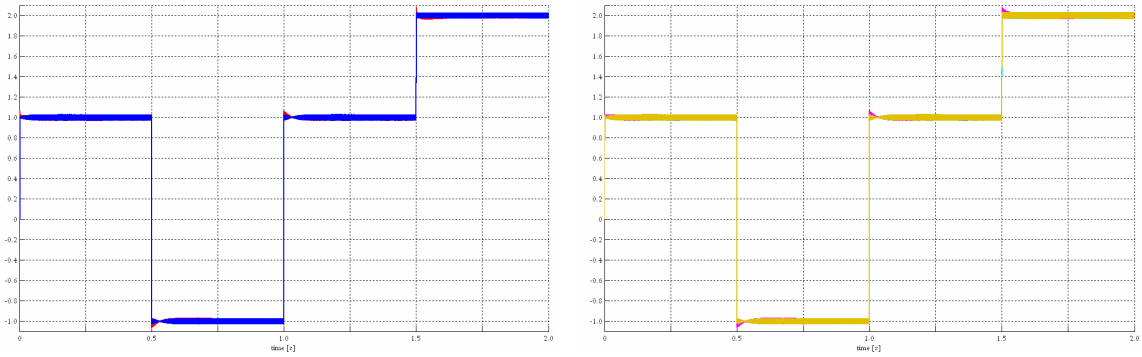

Figure III.57. Torque responses (in p.u., $T_e^* = 5$ Nm): cases 1c (red), 2c (blue), 3c (magenta), 4c (cyan) and 5c (gold).

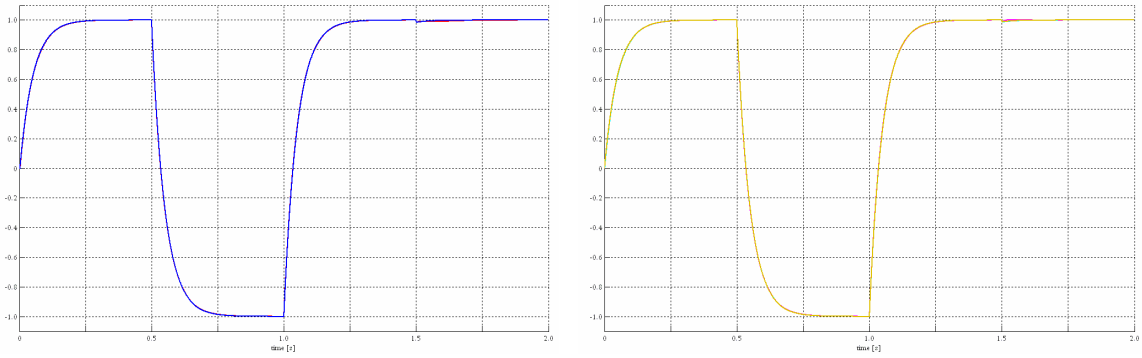

Figure III.58. Speed responses (in p.u., $\omega_m^* = 75$ rad/s): cases 1c (red), 2c (blue), 3c (magenta), 4c (cyan) and 5c (gold).

IV. ASYNCHRONOUS DRIVE

IV.1. Introduction

One of the most widely used actuators in variable speed drives is the asynchronous machine (AM). This is due to its ruggedness, maintenance free operation and many other advantages compared to the other servomotors. High performance asynchronous drives are today obtainable thanks to sophisticated control techniques implementation, such as Field Oriented Control. However, this last one requires the employment of current loops, PI regulators, coordinates transformations and, hence, fast and massive calculations which are performed by means of an appropriate microprocessor board.

A valid alternative is constituted by the Direct Torque Control (DTC) technique, which was firstly proposed in [14] and [15]. In fact, it allows simple and fast control of the AM torque by applying the supply voltages appropriately, without any current loop, PI regulator or coordinates transformation. Hence, this control technique offers advantages mainly due to the simplicity, the digital form of its control method and the reliability against uncertainty and parameters variations.

In the last twenty years, several improvements on the DTC technique have been introduced, so it has received considerable attention even in its application to other kinds of drives. In particular, the stator flux control instability, which occurred at low-speed operation, was overcome by properly modifying the traditional switching look-up table of the control system [16]. Subsequently, the stator voltages were synthesised using several algorithms, which ensure a constant switching frequency and bounded values of torque and stator flux, also maintaining a control structure similar to the traditional one [17-19]. In [20], the discrete time equations of the machine highlight the torque and flux variation at the end of each sampling interval, and the voltage vectors are synthesised by a kind of discrete space vector modulation technique, based on appropriate switching tables.

Usually, the DTC schemes employ stator flux and torque errors in order to choose the voltage vectors by means of the switching look-up table. Nevertheless, a different voltage selection procedure can be used, which avoids the employment of switching tables. It consists in using predictive algorithms, as in [1]. This technique is also employed in [21], where simplified discrete time machine equations, expressed in terms

of stator and rotor flux state variables, are used. Moreover, the achievement procedure of the voltage vector, which guarantees both the required flux and torque variations in each sampling time interval, is shown graphically. In this case too, the space vector modulation is used for the voltage synthesis.

In this work, using stator current and flux vectors as state variables, more rigorous discrete machine equations are assumed, thus a novel predictive DTC algorithm is developed. It directly synthesizes the voltage vector that allows the achievement of both reference stator flux magnitude and torque variations. This is done by finding the existence domain of the state variables in each sampling time interval. Obviously, both voltage saturation and current limitation constraints, which make a part of the existence domain unavailable, are taken into account. The synthesizing procedure adopted by the proposed algorithm is also shown by an interesting graphical representation. A computer simulation study of an asynchronous drive controlled by the proposed algorithm is conducted by using the Matlab Simulink environment. In particular, the comparison with the traditional DTC algorithm is carried out in order to highlight the better performance achieved by the predictive DTC algorithm proposed.

IV.2. Mathematical Models

The electrical equations of the AM can be expressed, in terms of space vectors, as in the following Eq. (IV.1):

$$\begin{aligned} \mathbf{v}^{(s)} &= r_s \cdot \mathbf{i}_s^{(s)} + \frac{d\boldsymbol{\lambda}_s^{(s)}}{dt} \\ 0 &= r_r \cdot \mathbf{i}_r^{(r)} + \frac{d\boldsymbol{\lambda}_r^{(r)}}{dt} \end{aligned} \qquad \text{(IV.1)}$$

being r_s and r_r the stator and the equivalent rotor phase resistance respectively, $v^{(s)}$ the supply voltage space vector and $i_s^{(s)}$ and $i_r^{(r)}$ the stator and the rotor current space vectors, all computable by the following Eq. (IV.2):

$$\mathbf{x}^{(s)} = \frac{2}{3} \cdot \left(x_1 + x_2 \cdot e^{j\frac{2}{3}\pi} + x_3 \cdot e^{j\frac{4}{3}\pi} \right) \quad , \quad \mathbf{x} = \{\mathbf{v}, \mathbf{i}, \boldsymbol{\lambda}\} \qquad \text{(IV.2)}$$

Moreover, $\lambda_s^{(s)}$ and $\lambda_r^{(r)}$, which are the magnetic flux vectors linked with the stator and the rotor winding respectively, can be expressed as follow:

$$\begin{aligned} \boldsymbol{\lambda}_s^{(s)} &= L_s \cdot \mathbf{i}_s^{(s)} + M \cdot \mathbf{i}_r^{(r)} \cdot e^{j\theta} \\ \boldsymbol{\lambda}_r^{(r)} &= M \cdot \mathbf{i}_s^{(s)} \cdot e^{-j\theta} + L_r \cdot \mathbf{i}_r^{(r)} \end{aligned} \quad , \quad \theta = p \cdot \theta_m \qquad \text{(IV.3)}$$

being L_s, L_r and M the equivalent inductance coefficients, p the pole pairs and θ_m the rotor position. Now, expressing all the space vector in the stator reference frame by means of Eq. (IV.4):

$$\mathbf{x}^{(s)} = \mathbf{x}^{(r)} \cdot e^{j\cdot\theta} \quad , \quad \mathbf{x} = \{\mathbf{v}, \mathbf{i}, \boldsymbol{\lambda}\} \qquad \text{(IV.4)}$$

the following result is achieved:

$$\begin{aligned} \mathbf{v}^{(s)} &= r_s \cdot \mathbf{i}_s^{(s)} + \frac{d\boldsymbol{\lambda}_s^{(s)}}{dt} \\ 0 &= r_r \cdot \mathbf{i}_r^{(s)} + \frac{d\boldsymbol{\lambda}_r^{(s)}}{dt} - j\omega \cdot \boldsymbol{\lambda}_r^{(s)} \end{aligned} \quad , \quad \omega = p\omega_m \qquad \text{(IV.5)}$$

being ω_m the rotor speed. Now, since the complex power $\mathcal{A}$ is:

$$\mathcal{A} = \frac{3}{2} \mathbf{v}^{(s)} \cdot \overline{\mathbf{i}}^{(s)} \qquad \text{(IV.6)}$$

the active power balance can be easily achieved from Eq. (IV.1), leading to the following equation:

$$\mathcal{P}_m = \frac{3}{2}\Re\left\{-j\omega\cdot\boldsymbol{\lambda}_r^{(s)}\cdot\overline{\mathbf{i}}_r^{(s)}\right\} = \frac{3}{2}\omega\cdot\Im\left\{\boldsymbol{\lambda}_r^{(s)}\cdot\overline{\mathbf{i}}_r^{(s)}\right\} \tag{IV.7}$$

where $\mathcal{P}_m$ is the electrical power converted into the mechanical one. Therefore, the electromagnetic torque is expressed as:

$$T_e = \frac{\mathcal{P}_m}{\omega_m} = \frac{3}{2}p\cdot\Im\left\{\boldsymbol{\lambda}_r^{(s)}\cdot\overline{\mathbf{i}}_r^{(s)}\right\} \tag{IV.8}$$

In conclusion, the mechanical equations are:

$$\begin{aligned} T_e &= D_m\cdot\omega_m + J_m\cdot\frac{d\omega_m}{dt} + T_{load} \\ \omega_m &= \frac{d\theta_m}{dt} \end{aligned} \tag{IV.9}$$

being J_m the rotor inertia, D_m the damping factor and T_{load} the load torque. So, the continuous time model of the AM is defined by Eq. (IV.3), Eq. (IV.5), Eq. (IV.8) and Eq. (IV.9), in which the state variables are the current and the magnetic flux space vectors, the mechanical speed ω_m and the rotor position θ_m. However, basing upon Eq. (IV.3), the following result can be obtained:

$$\begin{aligned} \mathbf{i}_r^{(s)} &= \frac{1}{M}\cdot\left(\boldsymbol{\lambda}_s^{(s)} - L_s\cdot\mathbf{i}_s^{(s)}\right) \\ \boldsymbol{\lambda}_r^{(s)} &= \frac{L_r}{M}\cdot\left(\boldsymbol{\lambda}_s^{(s)} - \sigma L_s\cdot\mathbf{i}_s^{(s)}\right) \end{aligned} \quad , \quad \sigma = 1 - \frac{M^2}{L_s L_r} \tag{IV.10}$$

being σ the leakage coefficient. Hence, by substituting Eq. (IV.10) in Eq. (IV.5), Eq. (IV.11) is achieved:

$$\begin{aligned} \frac{d\boldsymbol{\lambda}_s^{(s)}}{dt} &= -r_s\cdot\mathbf{i}_s^{(s)} + \mathbf{v}^{(s)} \\ \frac{d\mathbf{i}_s^{(s)}}{dt} &= \frac{1}{\sigma L_s}\left(\frac{r_r}{L_r} - j\omega\right)\cdot\boldsymbol{\lambda}_s^{(s)} - \left(\frac{r_s}{\sigma L_s} + \frac{r_r}{\sigma L_r} - j\omega\right)\cdot\mathbf{i}_s^{(s)} + \frac{1}{\sigma L_s}\mathbf{v}^{(s)} \end{aligned} \tag{IV.11}$$

In conclusion, Eq. (IV.11) becomes:

$$\frac{d\mathbf{x}^{(s)}}{dt} = \mathbf{A}\cdot\mathbf{x}^{(s)} + B\cdot\mathbf{v}^{(s)} \tag{IV.12}$$

where:

$$\mathbf{x}^{(s)} = \begin{bmatrix} \boldsymbol{\lambda}_s^{(s)} \\ \mathbf{i}_s^{(s)} \end{bmatrix} \quad , \quad \mathbf{A} = \begin{bmatrix} 0 & a_{12} \\ \mathbf{a}_{21} & \mathbf{a}_{22} \end{bmatrix} \quad , \quad B = \begin{bmatrix} 1 \\ b_2 \end{bmatrix} \tag{IV.13}$$

being:

$$\begin{aligned} a_{12} &= -r_s \quad , \quad \mathbf{a}_{21} = \frac{1}{\sigma L_s} \cdot \left(\frac{r_r}{L_r} - j\omega \right) \\ b_2 &= \frac{1}{\sigma L_s} \quad , \quad \mathbf{a}_{22} = -\left(\frac{r_r}{\sigma L_r} + \frac{r_s}{\sigma L_s} - j\omega \right) \end{aligned} \tag{IV.14}$$

Moreover, substituting Eq. (IV.10) in Eq. (IV.8), the torque expression becomes:

$$T_e = \frac{3}{2} p \cdot \Im\left\{ \boldsymbol{\lambda}_r^{(s)} \cdot \bar{\mathbf{i}}_r^{(s)} \right\} = -\frac{3}{2} p \cdot \Im\left\{ \boldsymbol{\lambda}_s^{(s)} \cdot \bar{\mathbf{i}}_s^{(s)} \right\} \tag{IV.15}$$

Now, in order to obtain the discrete time model of the AM, only Eq. (IV.12) and Eq. (IV.15) are considered. In fact, it is supposed that the sampling time T_s is chosen sufficiently small in order to consider the rotor speed ω_m constant in each sampling time interval, equal to $\omega_{m,k}$. Hence, referring to the generic kT_s sampling time instant, Eq. (IV.12) becomes:

$$\frac{d\mathbf{x}^{(s)}}{dt} = \mathbf{A}_k \cdot \mathbf{x}^{(s)} + B \cdot \mathbf{v}^{(s)} \quad , \quad \mathbf{A}_k = \mathbf{A}\big|_{\omega=\omega_k} \tag{IV.16}$$

Therefore, the discrete time model of the system, referred to the generic $[kT_s,(k+1)T_s]$ sampling time interval, is:

$$\mathbf{x}_{k+1}^{(s)} = \mathbf{F}_k \cdot \mathbf{x}_k^{(s)} + \mathbf{H}_k \cdot \boldsymbol{\Delta}\mathbf{T}_k^{(s)} \tag{IV.17}$$

where:

$$\mathbf{F}_k = \begin{bmatrix} \mathbf{f}_{11,k} & \mathbf{f}_{12,k} \\ \mathbf{f}_{21,k} & \mathbf{f}_{22,k} \end{bmatrix} = e^{\mathbf{A}_k \cdot T_s} \quad , \quad \mathbf{H}_k = \begin{bmatrix} \mathbf{h}_{1,k} \\ \mathbf{h}_{2,k} \end{bmatrix} = e^{\mathbf{A}_k \cdot \frac{T_s}{2}} \cdot B \cdot V \tag{IV.18}$$

being $\boldsymbol{\Delta}\mathbf{T}_k^{(s)}$ the αβ voltage pulse widths vector. Finally, considering Eq. (IV.15), the torque value reached at the end of the sampling time interval can be expressed as in Eq. (IV.19):

$$T_{e,k+1} = -\frac{3}{2} p \cdot \Im\left\{ \boldsymbol{\lambda}_{s,k+1}^{(s)} \cdot \bar{\mathbf{i}}_{s,k+1}^{(s)} \right\} = \frac{3}{4} p \cdot \Im\left\{ \left(\mathbf{x}_{k+1}^{(s)} \right)^H \cdot J \cdot \mathbf{x}_{k+1}^{(s)} \right\} \tag{IV.19}$$

IV.3. State and Speed Observers

Since the magnetic flux is not directly measurable, a reduced order observer is needed in order to make the state vector value available at the start of each sampling time interval. Therefore, the following expression is employed:

$$\frac{d\hat{\mathbf{x}}^{(s)}}{dt} = \mathbf{A}\cdot\hat{\mathbf{x}}^{(s)} + B\cdot\mathbf{v}^{(s)} + \mathbf{G}\cdot\left(\mathbf{i}_s^{(s)} - \hat{\mathbf{i}}_s^{(s)}\right) \tag{IV.20}$$

being $\hat{\mathbf{x}}^{(s)}$ the observed state and **G** the gain vector, which can be chosen in order to set the observer poles to the required values. Hence, being $\{\mathbf{p}_1,\mathbf{p}_2\}$ the continuous system poles and $\{\hat{\mathbf{p}}_1,\hat{\mathbf{p}}_2\}$ the corresponding observer ones, **G** can be determined by the following Eq. (IV.21):

$$\mathbf{G} = \begin{bmatrix}\mathbf{g}_1\\ \mathbf{g}_2\end{bmatrix} \quad , \quad \begin{cases}\mathbf{g}_1 = \dfrac{1}{\mathbf{a}_{21}}\left(\hat{\mathbf{p}}_1\cdot\hat{\mathbf{p}}_2 - \mathbf{p}_1\cdot\mathbf{p}_2\right)\\ \mathbf{g}_2 = \left(\mathbf{p}_1+\mathbf{p}_2\right) - \left(\hat{\mathbf{p}}_1+\hat{\mathbf{p}}_2\right)\end{cases} \tag{IV.21}$$

In this work, the observer poles were set in accordance with the following Eq. (IV.22):

$$\hat{p}_1 = 3\cdot\Re\{\mathbf{p}_1\} \quad , \quad \hat{p}_2 = 3\cdot\Re\{\mathbf{p}_2\} \tag{IV.22}$$

However, referring to the discrete time model of the AM, a predictive state observer can be also introduced by employing the following Eq. (IV.23):

$$\hat{\mathbf{x}}_k^{(s)} = \mathbf{F}_{k-1}\cdot\hat{\mathbf{x}}_{k-1}^{(s)} + \mathbf{H}_{k-1}\cdot\Delta\mathbf{T}_{k-1} + \mathbf{G}_{k-1}\cdot\left(\mathbf{i}_{s,k-1}^{(s)} - \hat{\mathbf{i}}_{s,k-1}^{(s)}\right) \tag{IV.23}$$

In fact, Eq. (IV.23) allows the prediction of both the flux and the current values in kT_s using only the current error in $(k-1)T_s$. The gain vector $\mathbf{G}_{k-1}$ can be chosen in order to set the observer poles to the required values, as usually. Hence, since the discrete system poles and the observer ones are expressed as in Eq. (IV.24) and in Eq. (IV.25) respectively:

$$\left\{\mathbf{p}_{1,k-1},\mathbf{p}_{2,k-1}\right\} \quad \rightarrow \quad \begin{cases}\mathbf{z}_{1,k-1} = e^{\mathbf{p}_{1,k-1}T_s}\\ \mathbf{z}_{2,k-1} = e^{\mathbf{p}_{2,k-1}T_s}\end{cases} \tag{IV.24}$$

$$\left\{\hat{\mathbf{p}}_{1,k-1},\hat{\mathbf{p}}_{2,k-1}\right\} \quad \rightarrow \quad \begin{cases}\hat{\mathbf{z}}_{1,k-1}=e^{\hat{\mathbf{p}}_{1,k-1}T_s}\\ \hat{\mathbf{z}}_{2,k-1}=e^{\hat{\mathbf{p}}_{2,k-1}T_s}\end{cases} \tag{IV.25}$$

the $\mathbf{G}_{k-1}$ gain vector can be computed by using the following Eq. (IV.26):

$$\mathbf{G}_{k-1}=\begin{bmatrix}\mathbf{g}_{1,k-1}\\ \mathbf{g}_{2,k-1}\end{bmatrix} \quad , \quad \begin{cases}\mathbf{g}_{1,k-1}=\dfrac{1}{\mathbf{f}_{21,k-1}}\left(\hat{\mathbf{z}}_{1,k-1}\hat{\mathbf{z}}_{2,k-1}-\mathbf{z}_{1,k-1}\mathbf{z}_{2,k-1}+\mathbf{f}_{11,k-1}\cdot\mathbf{g}_{2,k-1}\right)\\ \mathbf{g}_{2,k-1}=\left(\mathbf{z}_{1,k-1}+\mathbf{z}_{2,k-1}\right)-\left(\hat{\mathbf{z}}_{1,k-1}+\hat{\mathbf{z}}_{2,k-1}\right)\end{cases} \tag{IV.26}$$

Hence, by setting the observer poles as in Eq. (IV.22), the following expression is obtained:

$$\hat{z}_{1,k-1}=\left|\mathbf{z}_{1,k-1}\right|^3 \quad , \quad \hat{z}_{2,k-1}=\left|\mathbf{z}_{2,k-1}\right|^3 \tag{IV.27}$$

Moreover, in this case a predictive speed observer should be also introduced basing upon Eq. (IV.9), which can be expressed as follow:

$$\frac{d\omega_m}{dt}=-\frac{D_m}{J_m}\cdot\omega_m+\frac{T_e-T_{load}}{J_m} \tag{IV.28}$$

Therefore, referring to the generic $[(k-1)T_s,kT_s]$ sampling time interval, both the electromagnetic and the load torques are assumed constant, so, the following discrete time equation is obtained:

$$\hat{\omega}_{m,k}=f\cdot\hat{\omega}_{m,k-1}+h\cdot\left(T_{e,k-1}-T_{load}\right)+g\cdot\left(\omega_{m,k-1}-\hat{\omega}_{m,k-1}\right) \tag{IV.29}$$

being:

$$f=e^{-\frac{D_m}{J_m}T_s} \quad , \quad h=\frac{1}{D_m}\left(1-e^{-\frac{D_m}{J_m}T_s}\right) \tag{IV.30}$$

Finally, the gain g can be properly chosen as in Eq. (IV.31):

$$g=f-\hat{f} \tag{IV.31}$$

being $\hat{f}$ the required speed observer pole value. In this work, this last one is set as in Eq. (IV.32):

$$\hat{f}=f^3 \tag{IV.32}$$

IV.4. The Direct Torque Control Algorithms

The traditional DTC technique consists in keeping the stator flux magnitude constant, whereas the electromagnetic torque is driven by properly changing the stator flux rotational speed. This is done basing upon the following assumption:

$$r_s \cdot \mathbf{i}_s^{(s)} \cong 0 \qquad \rightarrow \qquad \mathbf{v}^{(s)} \cong \frac{d\boldsymbol{\lambda}_s^{(s)}}{dt} \tag{IV.33}$$

Therefore, assuming Eq. (IV.33), the stator flux vector can be directly driven by the voltage one. As a result, if $\mathbf{v}^{(s)}$ is applied along the flux direction, it varies its magnitude; otherwise, if it is applied orthogonal to the flux direction, it only determines a variation of its rotational speed.

The DTC technique is traditionally performed by employing an appropriate look-up table that directly synthesizes the voltage space vector in order to achieve the required reference values. In particular, referring to Fig. IV.1, firstly employing the reduced order state observer previously mentioned, the stator flux vector can be determined, so it is possible to evaluate both its magnitude and the torque value. These two signals are processed by their corresponding hysteresis regulators, then their output signals φ and τ are both sent to the look-up table in order to select the appropriate voltage vector.

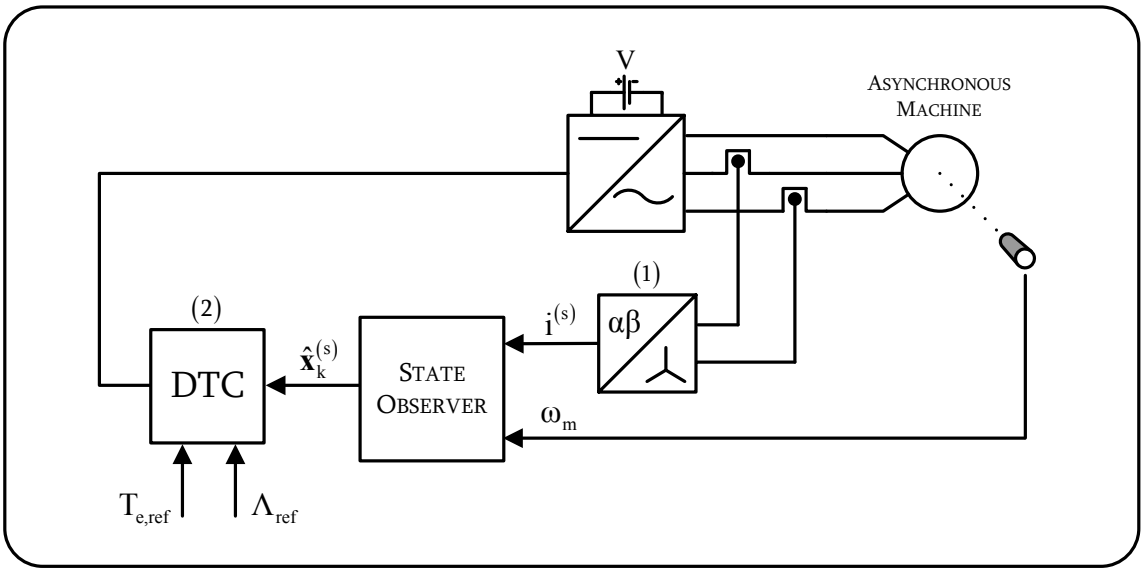

Figure IV.1. Block Control Scheme of the Asynchronous Drive employing the traditional DTC algorithm: (1) phase to α-β transformation; (2) Traditional DTC Algorithm.

The hysteresis regulators and the look-up table are usually modelled as in Fig. IV.2 and IV.3 respectively. However, at the start up of the motor, it is firstly necessary to achieve the reference flux magnitude; hence, only in this case, the hysteresis regulators and the look-up table configurations depicted in Fig. IV.4 and IV.5 can be better employed.

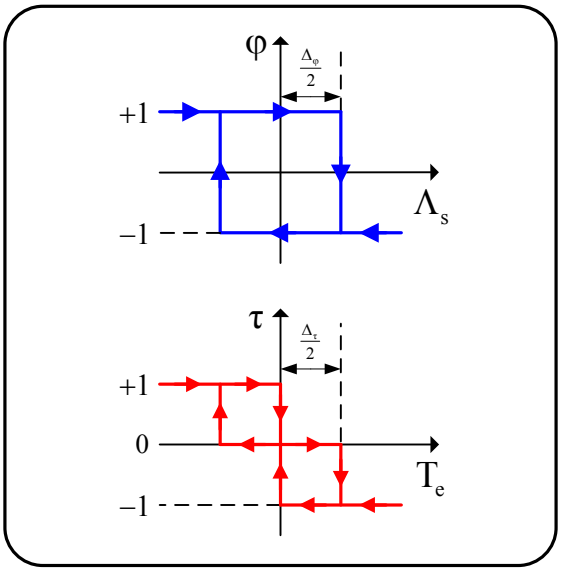

Figure IV.2. Hysteresis Regulators usually employed by traditional DTC algorithm.

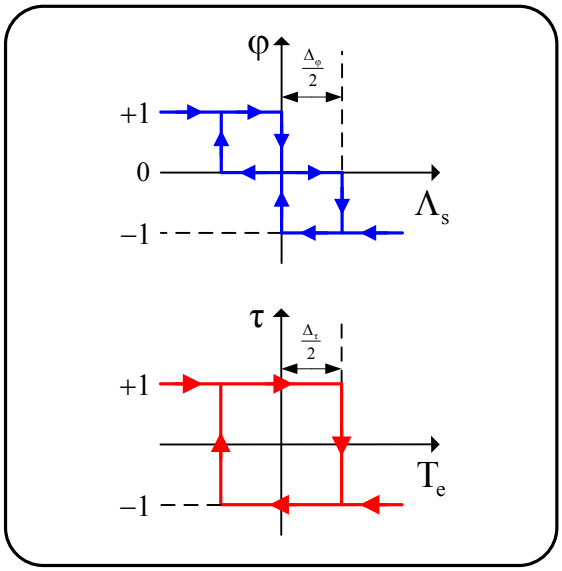

Figure IV.4. Hysteresis Regulators employed at the start up of the drive.

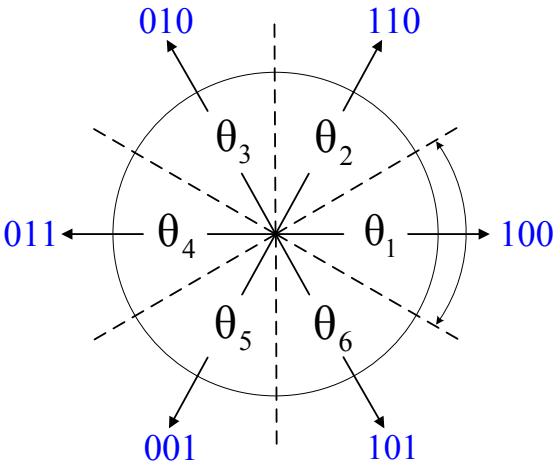

τ \ φ	θ1			θ2			θ3		
	−1	0	+1	−1	0	+1	−1	0	+1
−1	001	000	010	101	111	011	100	000	001
+1	101	111	110	100	000	010	110	111	011

τ \ φ	θ4			θ5			θ6		
	−1	0	+1	−1	0	+1	−1	0	+1
−1	110	111	101	010	000	100	011	111	110
+1	010	000	001	011	111	101	001	000	100

Figure IV.3. Traditional DTC look-up table.

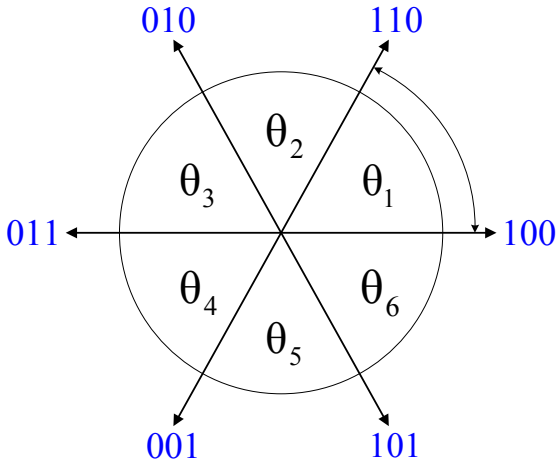

τ \ φ	θ1			θ2			θ3		
	−1	0	+1	−1	0	+1	−1	0	+1
−1	001	000	100	101	111	110	100	000	010
+1	011	111	110	001	000	010	101	111	011

τ \ φ	θ4			θ5			θ6		
	−1	0	+1	−1	0	+1	−1	0	+1
−1	110	111	011	010	000	001	011	111	101
+1	100	000	001	110	111	101	010	000	100

Figure IV.5. DTC Look-up table employed at the start up of the drive.

The proposed predictive algorithm is developed with the aim of improve the performance obtainable by the traditional DTC technique. In fact, this last one is characterized by some drawbacks especially at low speed operation, when Eq. (IV.33) should not be assumed. So, the predictive state and speed observers are introduced in order to successfully postpone the application of the voltage pulse widths vector to the next sampling time intervals, as shown in the equivalent control scheme of the drive depicted in Fig. IV.6. Then, the following state and torque value are introduced:

$$\tilde{\mathbf{x}}_{k+1}^{(s)} = \begin{bmatrix} \tilde{\boldsymbol{\lambda}}_{s,k+1}^{(s)} \\ \tilde{\mathbf{i}}_{s,k+1}^{(s)} \end{bmatrix} = \mathbf{F}_k \cdot \mathbf{x}_k^{(s)} \tag{IV.34}$$

$$\tilde{T}_{e,k+1} = -\frac{3}{2} p \cdot \Im\left\{ \tilde{\boldsymbol{\lambda}}_{s,k+1}^{(s)} \cdot \overline{\tilde{\mathbf{i}}}_{s,k+1}^{(s)} \right\} \tag{IV.35}$$

They represent the values assumed by the corresponding variables in $(k+1)T_s$ if the zero voltage vector is applied in the $[kT_s,(k+1)T_s]$ sampling time interval (unforced evolution). Now, by properly combining Eq. (IV.34) and Eq. (IV.35) with Eq. (IV.17) and Eq. (IV.19), the following linear system can be achieved:

$$\begin{bmatrix} \boldsymbol{\alpha}_{x,k} & \beta_{x,k} & \overline{\boldsymbol{\alpha}}_{x,k} \\ \boldsymbol{\alpha}_{y,k} & \beta_{y,k} & \overline{\boldsymbol{\alpha}}_{y,k} \\ \boldsymbol{\alpha}_{z,k} & \beta_{z,k} & \overline{\boldsymbol{\alpha}}_{z,k} \end{bmatrix} \cdot \begin{bmatrix} \boldsymbol{\Delta T}_k \\ T_k^2 \\ \overline{\boldsymbol{\Delta T}}_k \end{bmatrix} = \begin{bmatrix} \delta_{x,k+1} \\ \delta_{y,k+1} \\ \delta_{z,k+1} \end{bmatrix} \tag{IV.36}$$

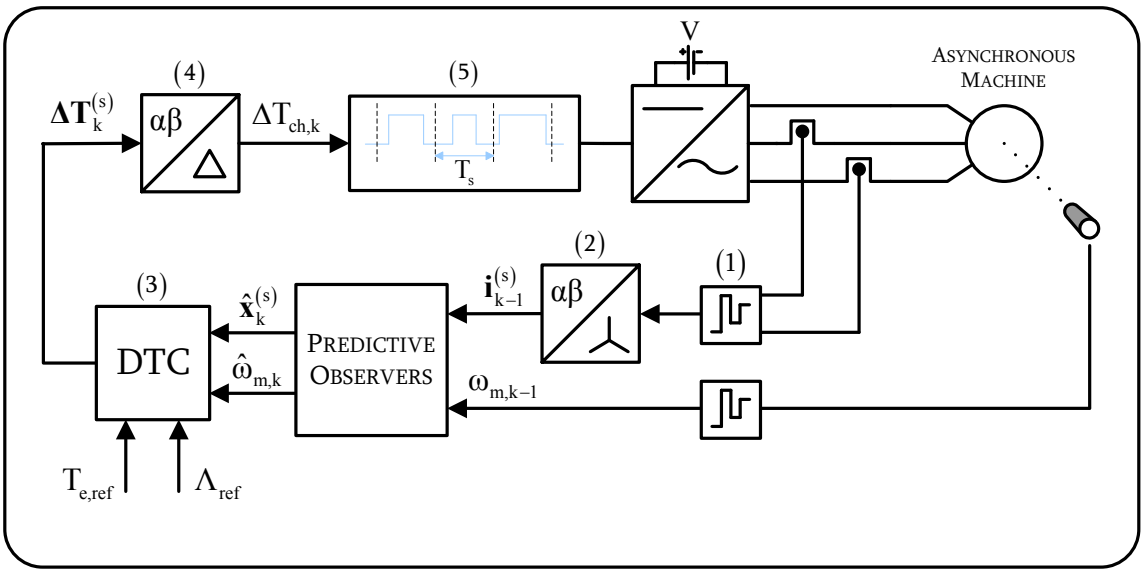

Figure IV.6. Block Control Scheme of the Asynchronous Drive employing the proposed predictive DTC algorithm: (1) sample & hold; (2) phase to α-β transformation; (3) Predictive DTC Algorithm; (4) αβ to chain transformation; (5) symmetrical pulses generator.

being T_k the magnitude of the voltage pulse widths vector and:

$$\begin{cases} \boldsymbol{\alpha}_{x,k} = \mathbf{h}_{1,k} \cdot \overline{\tilde{\boldsymbol{\lambda}}}^{(s)}_{s,k+1} \\ \boldsymbol{\alpha}_{y,k} = j \cdot \left(\mathbf{h}_{1,k} \cdot \overline{\tilde{\mathbf{i}}}^{(s)}_{s,k+1} - \mathbf{h}_{2,k} \cdot \overline{\tilde{\boldsymbol{\lambda}}}^{(s)}_{s,k+1} \right) \\ \boldsymbol{\alpha}_{z,k} = \mathbf{h}_{2,k} \cdot \overline{\tilde{\mathbf{i}}}^{(s)}_{s,k+1} \end{cases} \qquad \begin{cases} \beta_{x,k} = \left| \mathbf{h}_{1,k} \right|^2 \\ \beta_{y,k} = 2 \cdot \Im \left\{ \overline{\mathbf{h}}_{1,k} \cdot \mathbf{h}_{2,k} \right\} \\ \beta_{z,k} = \left| \mathbf{h}_{2,k} \right|^2 \end{cases} \tag{IV.37}$$

$$\begin{cases} \delta_{x,k+1} = \left| \boldsymbol{\lambda}^{(s)}_{s,k+1} \right|^2 - \left| \tilde{\boldsymbol{\lambda}}^{(s)}_{s,k+1} \right|^2 \\ \delta_{y,k+1} = \dfrac{4}{3 \cdot p} \cdot \left(T_{e,k+1} - \tilde{T}_{e,k+1} \right) \\ \delta_{z,k+1} = \left| \mathbf{i}^{(s)}_{s,k+1} \right|^2 - \left| \tilde{\mathbf{i}}^{(s)}_{s,k+1} \right|^2 \end{cases} \tag{IV.38}$$

Hence, solving Eq. (IV.36), both T_k and the phase τ_k of the voltage pulse widths vector can be determined, as in Eq. (IV.39):

$$T_k = \sqrt{\frac{\gamma_{2,k}}{\gamma_{0,k}}} \quad , \quad \tau_k = \operatorname{sign}(j \cdot \gamma_{0,k}) \cdot \frac{\pi}{2} + \measuredangle \left(\gamma_{1,k} \right) \tag{IV.39}$$

where:

$$\begin{aligned} \gamma_{0,k} &= -j \cdot 2 \cdot \sum_{u,v,w} \beta_{u,k} \cdot \Im \left\{ \boldsymbol{\alpha}_{v,k} \cdot \overline{\boldsymbol{\alpha}}_{w,k} \right\} \\ \gamma_{1,k} &= \sum_{u,v,w} \delta_{u,k+1} \cdot \left(\beta_{v,k} \cdot \overline{\boldsymbol{\alpha}}_{w,k} - \beta_{w,k} \cdot \overline{\boldsymbol{\alpha}}_{v,k} \right) \quad (u,v,w) = \left\{ (x,y,z), (y,z,x), (z,x,y) \right\} \\ \gamma_{2,k} &= -j \cdot 2 \cdot \sum_{u,v,w} \delta_{u,k+1} \cdot \Im \left\{ \boldsymbol{\alpha}_{v,k} \cdot \overline{\boldsymbol{\alpha}}_{w,k} \right\} \end{aligned} \tag{IV.40}$$

However, Eq. (IV.36) also imposes the following constraint:

$$\left| \gamma_{1,k} \right|^2 + \gamma_{0,k} \cdot \gamma_{2,k} = 0 \tag{IV.41}$$

Therefore, substituting Eq. (IV.40) in Eq. (IV.41), it becomes:

$$\Delta^T_{k+1} \cdot P_k \cdot \Delta_{k+1} + 2 p^T_k \cdot \Delta_{k+1} = 0 \quad , \quad \Delta_{k+1} = \begin{bmatrix} \delta_{x,k+1} \\ \delta_{y,k+1} \\ \delta_{z,k+1} \end{bmatrix} \tag{IV.42}$$

being:

$$P_k = \begin{bmatrix} p_{xx,k} & p_{xy,k} & p_{zx,k} \\ p_{xy,k} & p_{yy,k} & p_{yz,k} \\ p_{zx,k} & p_{yz,k} & p_{zz,k} \end{bmatrix} \quad , \quad p_k = \begin{bmatrix} p_{x,k} \\ p_{y,k} \\ p_{z,k} \end{bmatrix} \tag{IV.43}$$

Referring to the $(\delta_x,\delta_y,\delta_z)$ space, Eq. (IV.42) corresponds to the elliptic paraboloid P_k shown in Fig. IV.7: it is made up of all the $(\delta_x,\delta_y,\delta_z)$ values reachable at the end of the $[kT_s,(k+1)T_s]$ sampling time interval.

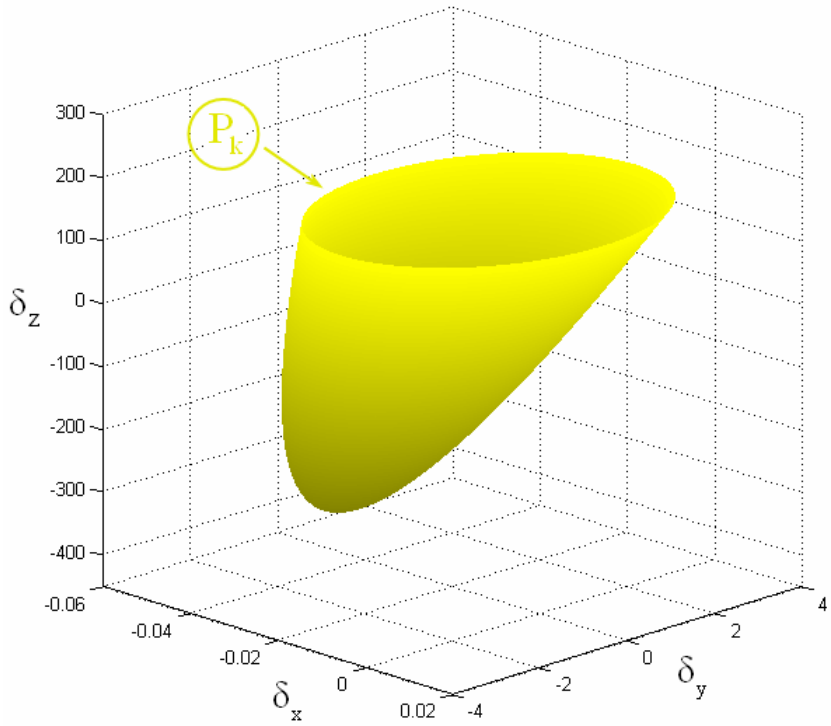

Figure IV.7. The elliptic paraboloid P_k.

Obviously, the inverter current limitation and the voltage saturation constraints must be also taken into account: they can be respectively expressed by the following Eq. (IV.44) and Eq. (IV.45):

$$\left|\mathbf{i}_{s,k+1}^{(s)}\right| \le \Im_{max} \quad \rightarrow \quad \delta_{z,k+1} \le \Im_{max} - \left|\tilde{\mathbf{i}}_{s,k+1}^{(s)}\right|^2 \tag{IV.44}$$

$$T_k \le \frac{T_s}{\sqrt{3}} \quad \rightarrow \quad T_k^2 \le \frac{T_s^2}{3} \quad \rightarrow \quad \gamma_{2,k} \le \gamma_{0,k}\frac{T_s^2}{3} \tag{IV.45}$$

In the $(\delta_x,\delta_y,\delta_z)$ space, these last equations correspond to two different half-spaces, respectively bounded by the following planes:

$$\delta_{z,k+1} = \delta_{z,k+1}^{(max)} \quad , \quad \delta_{z,k+1}^{(max)} = \Im_{max} - \left|\tilde{\mathbf{i}}_{s,k+1}^{(s)}\right|^2 \tag{IV.46}$$

$$\Im\left\{\boldsymbol{\alpha}_{y,k}\cdot\bar{\boldsymbol{\alpha}}_{z,k}\right\}\delta_{x,k+1} + \Im\left\{\boldsymbol{\alpha}_{z,k}\cdot\bar{\boldsymbol{\alpha}}_{x,k}\right\}\delta_{y,k+1} + \Im\left\{\boldsymbol{\alpha}_{x,k}\cdot\bar{\boldsymbol{\alpha}}_{y,k}\right\}\delta_{z,k+1} = j\frac{\gamma_{0,k}}{2}\frac{T_s^2}{3} \tag{IV.47}$$

Therefore, combining Eq. (IV.46) and Eq. (IV.47) with Eq. (IV.42), the following expression are respectively obtained:

$$\begin{bmatrix}\delta_{x,k+1} & \delta_{y,k+1}\end{bmatrix}\cdot\Phi_k\cdot\begin{bmatrix}\delta_{x,k+1}\\ \delta_{y,k+1}\end{bmatrix}+2\varphi_k^T\cdot\begin{bmatrix}\delta_{x,k+1}\\ \delta_{y,k+1}\end{bmatrix}+\varphi_{0,k}=0 \tag{IV.48}$$

$$\begin{bmatrix}\delta_{x,k+1} & \delta_{y,k+1}\end{bmatrix}\cdot\mathfrak{E}_k\cdot\begin{bmatrix}\delta_{x,k+1}\\ \delta_{y,k+1}\end{bmatrix}+2\varepsilon_k^T\cdot\begin{bmatrix}\delta_{x,k+1}\\ \delta_{y,k+1}\end{bmatrix}+\varepsilon_{0,k}=0 \tag{IV.49}$$

being:

$$\Phi_k=\begin{bmatrix}\varphi_{xx,k} & \varphi_{xy,k}\\ \varphi_{xy,k} & \varphi_{yy,k}\end{bmatrix}\quad,\quad \varphi_k=\begin{bmatrix}\varphi_{x,k}\\ \varphi_{y,k}\end{bmatrix} \tag{IV.50}$$

$$\mathfrak{E}_k=\begin{bmatrix}\varepsilon_{xx,k} & \varepsilon_{xy,k}\\ \varepsilon_{xy,k} & \varepsilon_{yy,k}\end{bmatrix}\quad,\quad \varepsilon_k=\begin{bmatrix}\varepsilon_{x,k}\\ \varepsilon_{y,k}\end{bmatrix} \tag{IV.51}$$

In particular, both Eq. (IV.46) and Eq. (IV.48) define the ellipse E_k, which is obtained by the intersection of the elliptic paraboloid P_k with the plane defined by Eq. (IV.46). In the same way, Eq. (IV.47) and Eq. (IV.49) define the ellipse $\mathfrak{E}_k$, which represents the intersection of P_k with the plane defined by Eq. (IV.47). Both these curves and the elliptic paraboloid P_k are shown in Fig. IV.8.

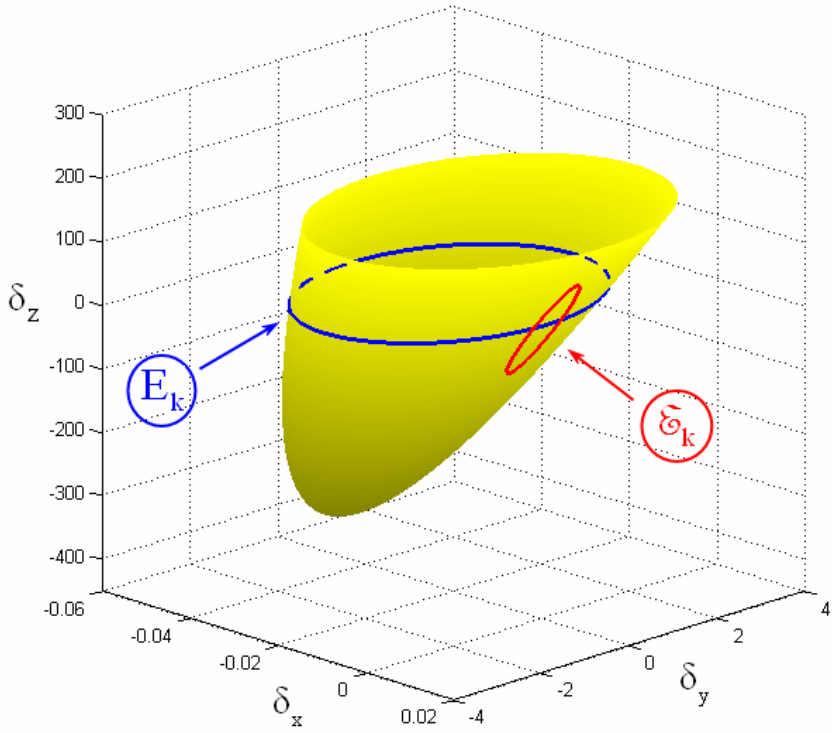

Figure IV.8. The elliptic paraboloid P_k (gold) and the two ellipses E_k and $\mathfrak{E}_k$.

Now, since the reference quantities are:

$$\begin{aligned}\delta_{x,k+1}^{(ref)} &= \Lambda_{ref}^2 - \left|\tilde{\lambda}_{s,k+1}^{(s)}\right|^2 \\ \delta_{y,k+1}^{(ref)} &= \frac{4}{3\cdot p}\cdot\left(T_{e,ref} - \tilde{T}_{e,k+1}\right)\end{aligned} \tag{IV.52}$$

it is necessary to project the elliptic paraboloid and the two ellipses previously determined on the (δ_x,δ_y) plane in order to find all the points available. Therefore, by firstly imposing the existence condition of only one solution for $\delta_{z,k+1}$ in Eq. (IV.42), Eq. (IV.53) and Eq. (IV.54) are obtained:

$$p_{zx,k}\cdot\delta_{x,k+1} + p_{yz,k}\cdot\delta_{y,k+1} + p_{zz,k}\cdot\delta_{z,k+1} + p_{z,k} = 0 \tag{IV.53}$$

$$\begin{bmatrix}\delta_{x,k+1} & \delta_{y,k+1}\end{bmatrix}\cdot Q_k \cdot \begin{bmatrix}\delta_{x,k+1}\\ \delta_{y,k+1}\end{bmatrix} + 2q_k^T \cdot \begin{bmatrix}\delta_{x,k+1}\\ \delta_{y,k+1}\end{bmatrix} + q_{0,k} = 0 \tag{IV.54}$$

being:

$$Q_k = \begin{bmatrix}q_{xx,k} & q_{xy,k}\\ q_{xy,k} & q_{yy,k}\end{bmatrix} \quad , \quad q_k = \begin{bmatrix}q_{x,k}\\ q_{y,k}\end{bmatrix} \tag{IV.55}$$

Always referring to the $(\delta_x,\delta_y,\delta_z)$ space, both Eq. (IV.53) and Eq. (IV.54) correspond to the parabola $\mathcal{P}_k$ shown in Fig. IV.9.

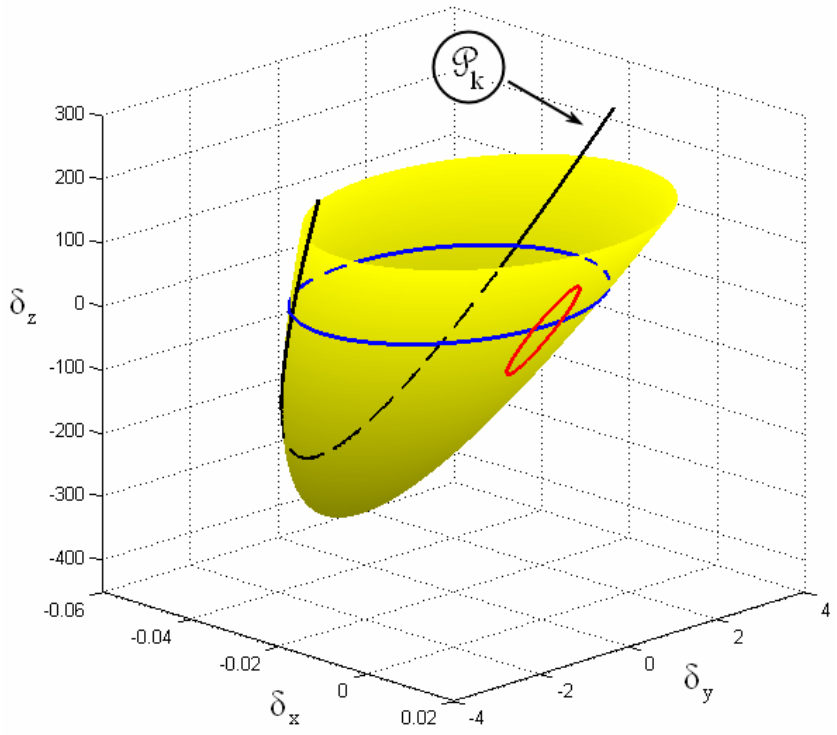

Figure IV.9. The elliptic paraboloid P_k (gold), the two ellipses E_k (blue) and $\mathcal{E}_k$ (red) and the parabola $\mathcal{P}_k$.

Therefore, Eq. (IV.54) corresponds to the projection of $\mathcal{P}_k$ on the (δ_x,δ_y) plane, whereas Eq. (IV.48) and Eq. (IV.49) respectively correspond to the projection of E_k and $\mathcal{E}_k$ on the same plane. All these projections allow the determination of all the (δ_x,δ_y) values available at the end of the $[kT_s,(k+1)T_s]$ sampling time interval, which constitute the plane region $\mathcal{D}_k$ highlighted in Fig. IV.10 and in Fig. IV.11.

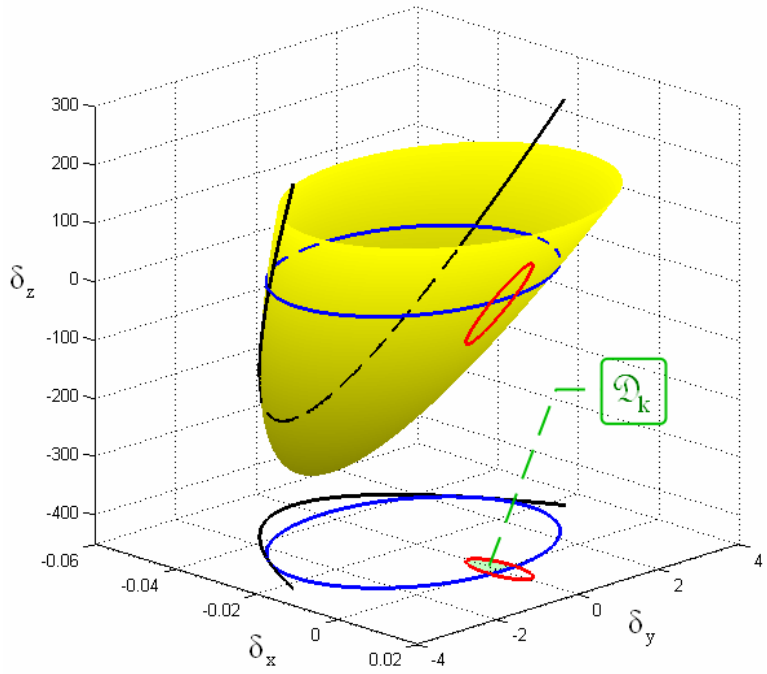

Figure IV.10. The plane region $\mathcal{D}_k$ bounded by the projection of $\mathcal{P}_k$ (black), E_k (blue) and $\mathcal{E}_k$ (red).

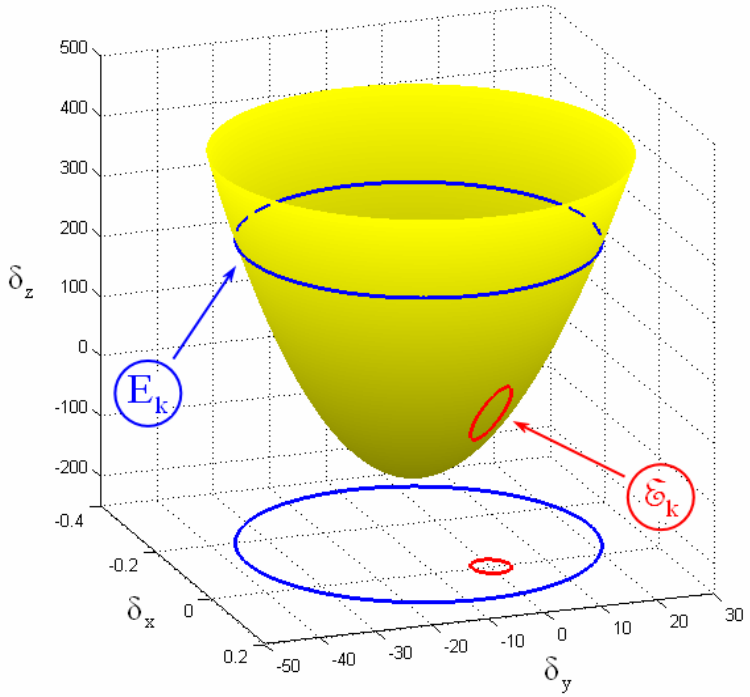

Figure IV.11. P_k, E_k and $\mathcal{E}_k$ when $\Lambda_{k+1} = \Lambda_{ref}$ and $T_e \neq T_{e,ref}$.

Summarizing, the reference values expressed by Eq. (IV.52) can be achieved only if they belong to $\mathfrak{D}_k$. Otherwise, two different events can occur: in the first one, when the reference flux magnitude Λ_{ref} cannot be reached, the maximum available variation of δ_x is imposed, meaning the achievement of the point A shown in Fig. IV.12. In the second case, when the Λ_{ref} value is already achieved, the maximum available variation of δ_y is imposed, in order to reach the torque reference value as fast as possible. Referring to Fig. IV.13, this condition is satisfied by reaching the point B.

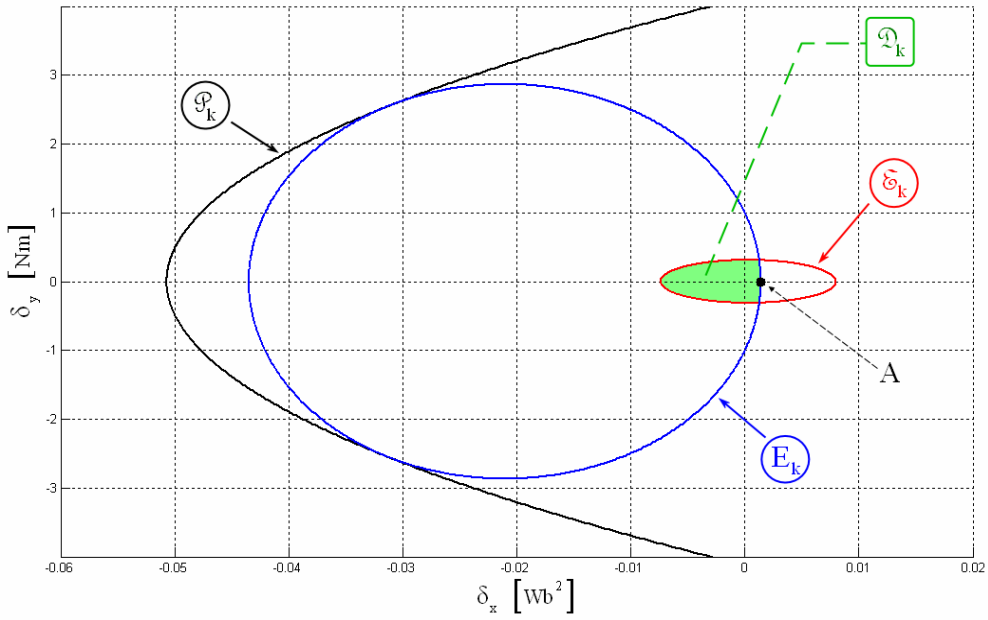

Figure IV.12. The plane region $\mathfrak{D}_k$ bounded by the projection of $\mathfrak{P}_k$, E_k and $\mathfrak{E}_k$: $\Lambda_{k+1} \neq \Lambda_{ref}$ and $T_e = 0$.

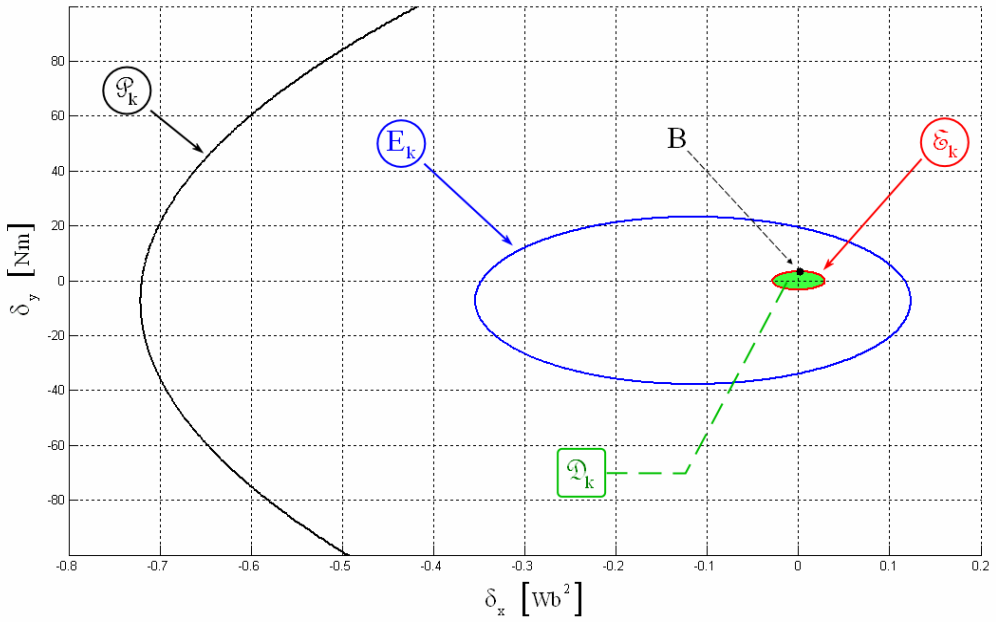

Figure IV.13. The plane region $\mathfrak{D}_k$ bounded by the projection of $\mathfrak{P}_k$, E_k and $\mathfrak{E}_k$: $\Lambda_{k+1} = \Lambda_{ref}$ and $T_e \neq T_{e,ref}$.

In conclusion, all the coefficients of Eq. (IV.43), Eq. (IV.50), Eq. (IV.51) and Eq. (IV.55) are:

$$p_{xx,k} = \left| \beta_{y,k}\boldsymbol{\alpha}_{z,k} - \beta_{z,k}\boldsymbol{\alpha}_{y,k} \right|^2$$
$$p_{yy,k} = \left| \beta_{z,k}\boldsymbol{\alpha}_{x,k} - \beta_{x,k}\boldsymbol{\alpha}_{z,k} \right|^2$$
$$p_{zz,k} = \left| \beta_{x,k}\boldsymbol{\alpha}_{y,k} - \beta_{y,k}\boldsymbol{\alpha}_{z,k} \right|^2$$
$$p_{xy,k} = -\beta_{x,k}\beta_{y,k}\left|\boldsymbol{\alpha}_{z,k}\right|^2 - \beta_{z,k}^2 \cdot \Re\left\{\boldsymbol{\alpha}_{x,k}\overline{\boldsymbol{\alpha}}_{y,k}\right\} + \beta_{z,k} \cdot \Re\left\{\beta_{x,k}\overline{\boldsymbol{\alpha}}_{y,k}\boldsymbol{\alpha}_{z,k} + \beta_{y,k}\overline{\boldsymbol{\alpha}}_{z,k}\boldsymbol{\alpha}_{x,k}\right\}$$
$$p_{yz,k} = -\beta_{y,k}\beta_{z,k}\left|\boldsymbol{\alpha}_{x,k}\right|^2 - \beta_{x,k}^2 \cdot \Re\left\{\boldsymbol{\alpha}_{y,k}\overline{\boldsymbol{\alpha}}_{z,k}\right\} + \beta_{x,k} \cdot \Re\left\{\beta_{y,k}\overline{\boldsymbol{\alpha}}_{z,k}\boldsymbol{\alpha}_{x,k} + \beta_{z,k}\overline{\boldsymbol{\alpha}}_{x,k}\boldsymbol{\alpha}_{y,k}\right\}$$
$$p_{zx,k} = -\beta_{z,k}\beta_{x,k}\left|\boldsymbol{\alpha}_{y,k}\right|^2 - \beta_{y,k}^2 \cdot \Re\left\{\boldsymbol{\alpha}_{z,k}\overline{\boldsymbol{\alpha}}_{x,k}\right\} + \beta_{y,k} \cdot \Re\left\{\beta_{z,k}\overline{\boldsymbol{\alpha}}_{x,k}\boldsymbol{\alpha}_{y,k} + \beta_{x,k}\overline{\boldsymbol{\alpha}}_{y,k}\boldsymbol{\alpha}_{z,k}\right\}$$
$$p_{x,k} = -j\gamma_{0,k} \cdot \Im\left\{\boldsymbol{\alpha}_{y,k}\overline{\boldsymbol{\alpha}}_{z,k}\right\}$$
$$p_{y,k} = -j\gamma_{0,k} \cdot \Im\left\{\boldsymbol{\alpha}_{z,k}\overline{\boldsymbol{\alpha}}_{x,k}\right\}$$
$$p_{z,k} = -j\gamma_{0,k} \cdot \Im\left\{\boldsymbol{\alpha}_{x,k}\overline{\boldsymbol{\alpha}}_{y,k}\right\}$$

$$\varphi_{xx,k} = p_{xx,k} \qquad \varepsilon_{xx,k} = \left|\boldsymbol{\alpha}_{y,k}\right|^2$$
$$\varphi_{xy,k} = p_{xy,k} \qquad \varepsilon_{xy} = -\Re\left\{\boldsymbol{\alpha}_{x,k}\overline{\boldsymbol{\alpha}}_{y,k}\right\}$$
$$\varphi_{yy,k} = p_{yy,k} \qquad \varepsilon_{yy} = \left|\boldsymbol{\alpha}_{x,k}\right|^2$$
$$\varphi_{x,k} = p_{x,k} + p_{zx,k} \cdot \delta_{z,k+1}^{(max)} \qquad \varepsilon_{x,k} = \frac{T_s^2}{3}\frac{q_{x,k}}{2}$$
$$\varphi_{y,k} = p_{y,k} + p_{yz,k} \cdot \delta_{z,k+1}^{(max)} \qquad \varepsilon_{y,k} = \frac{T_s^2}{3}\frac{q_{y,k}}{2}$$
$$\varphi_{0,k} = \left(2p_{z,k} + p_{zz,k} \cdot \delta_{z,k+1}^{(max)}\right) \cdot \delta_{z,k+1}^{(max)} \qquad \varepsilon_{0,k} = \left(p_{zz,k} \cdot \frac{T_s^2}{3} + q_{0,k}\right) \cdot \frac{T_s^2}{3}$$

$$q_{xx,k} = \beta_{y,k}^2$$
$$q_{xy} = -\beta_{x,k}\beta_{y,k}$$
$$q_{yy} = \beta_{x,k}^2$$
$$q_{x,k} = -2\left(\beta_{x,k}\left|\boldsymbol{\alpha}_{y,k}\right|^2 - \beta_{y,k} \cdot \Re\left\{\boldsymbol{\alpha}_{x,k}\overline{\boldsymbol{\alpha}}_{y,k}\right\}\right)$$
$$q_{y,k} = -2\left(\beta_{y,k}\left|\boldsymbol{\alpha}_{x,k}\right|^2 - \beta_{x,k} \cdot \Re\left\{\boldsymbol{\alpha}_{x,k}\overline{\boldsymbol{\alpha}}_{y,k}\right\}\right)$$
$$q_{0,k} = -4 \cdot \Im\left\{\boldsymbol{\alpha}_{x,k}\overline{\boldsymbol{\alpha}}_{y,k}\right\}^2$$

IV.5. Simulations and Results

In order to highlight the better performance obtainable by the proposed predictive DTC algorithm, a simulation study was carried out in the MATLAB Simulink environment. The drive block scheme employed in the simulations is depicted in Fig. IV.14: as usually, the DC voltage source, the inverter and the AM were modelled by using the SimPowerSystem Library, whereas all the other control blocks were realized by means of the Simulink Library. The simulations parameters values are those reported in Table IV.1, whereas the switching frequency was set to 10 kHz in all the simulations performed.

TABLE IV.1

PARAMETERS		UNITS
r_s	0.8	[Ω]
r_r	0.9	[Ω]
L_s	76	[mH]
L_r	76	[mH]
M	72	[mH]
p	2	[-]
J_m	0.016	[Kgm^2]
D_m	0.2	[Nms]
T_s	100	[μs]
V	297	[V]

The traditional DTC technique with constant switching frequency is firstly employed. However, two different look-up tables are used: the first one, already shown in Fig. IV.5, is employed at the start-up of the drive, with the aim of reaching the reference stator flux magnitude as fast as possible. Then, the conventional look-up table depicted in Fig. IV.3 is introduced. Furthermore, the bandwidths of the torque and the flux hysteresis regulators employed were set both to 5% of their reference values, whereas the observer poles are set in accordance with Eq. (IV.22).

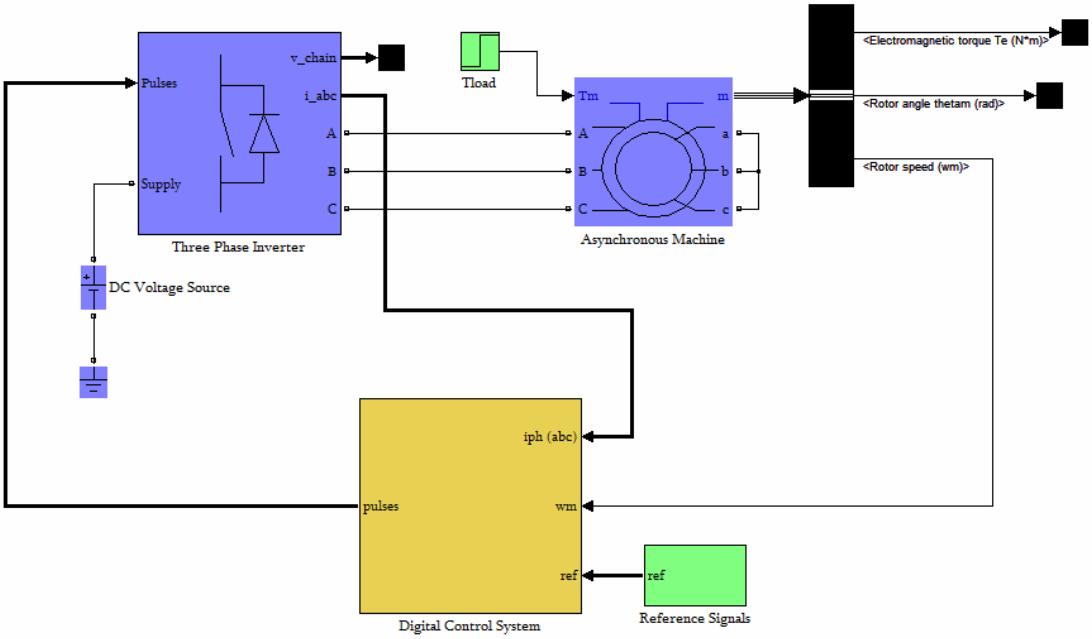

Figure IV.14. Block Control Scheme of the Asynchronous Drive employed for the simulations.

Otherwise, considering the application of the predictive DTC algorithm proposed, both predictive state and speed observers are employed, whose poles are set in accordance with Eq. (IV.27) and Eq. (IV.32) respectively.

First of all, the simulation study concerns the start up of the drive, starting from rest. Regardless of the control algorithms employed, the achievement of the reference magnitude of the stator flux vector (0.85 Wb) is imposed firstly. Then, as soon as it is achieved, a step reference torque of 6 Nm is applied in order to reach the low steady state speed value of 30 rad/s. The corresponding simulation results obtained by the traditional DTC technique and by the proposed predictive DTC algorithm are depicted from Fig. IV.15 through Fig. IV.20.

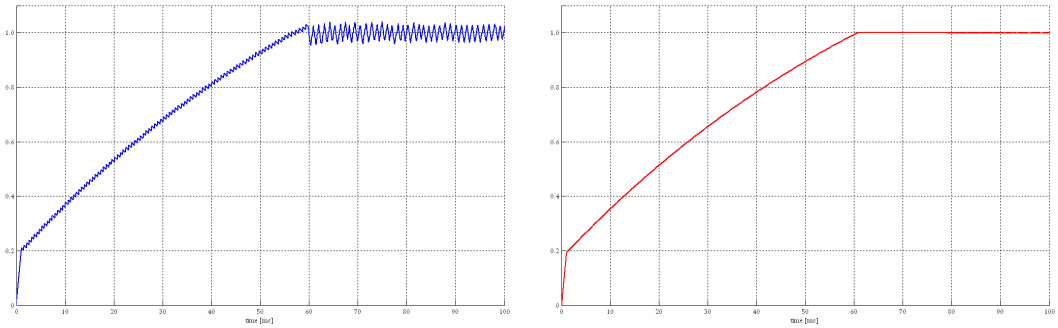

Figure IV.15. Stator Flux Vector Magnitude responses at start up (in p.u., $\Lambda^* = 0.85$ Wb): traditional DTC (on the left) and predictive DTC (on the right).

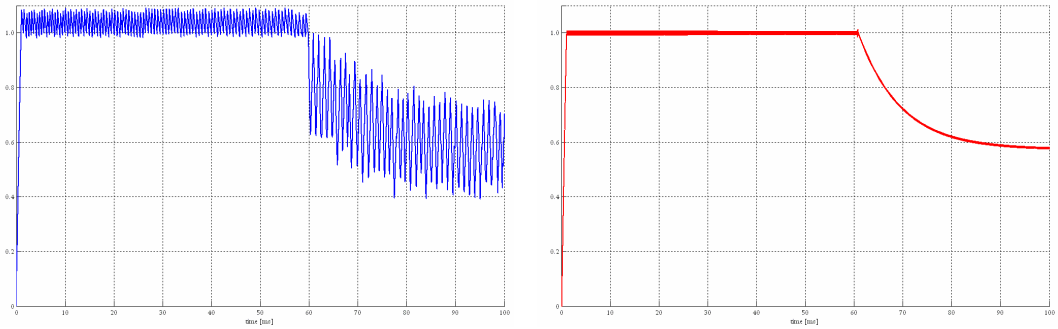

Figure IV.16. Stator Current Vector Magnitude responses at start up (in p.u., $\mathcal{S}^* = 20$ A): traditional DTC (on the left) and predictive DTC (on the right).

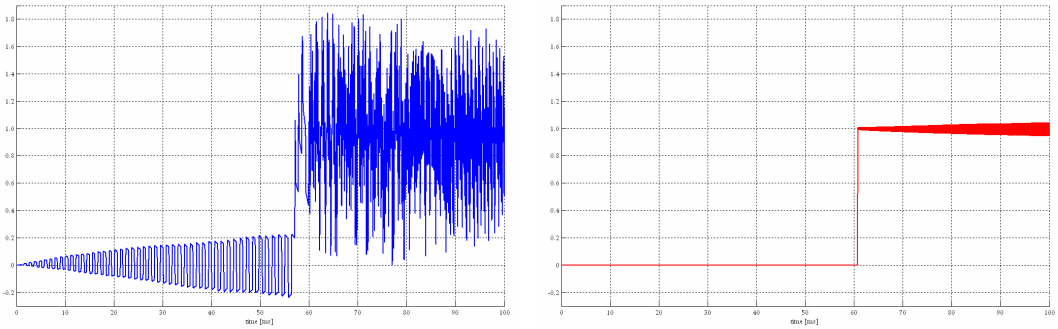

Figure IV.17. Torque responses at start up (in p.u., $T_e^* = 6$ Nm): traditional DTC (on the left) and predictive DTC (on the right).

It can be seen in both cases that the variation of the flux magnitude is constrained by voltage saturation firstly. Then, when the magnitude of the current vector reaches its maximum value of 20 A, the variation of the stator flux magnitude becomes slower than before, due to the current limitation imposed. After the achievement of the reference stator flux magnitude, which occurs in about 60 ms, the torque reference value is quickly achieved, while the magnitude of the current vector is gradually reduced. However, by employing the predictive DTC algorithm, all the variables are affected by very low ripples, compared to those of the traditional DTC.

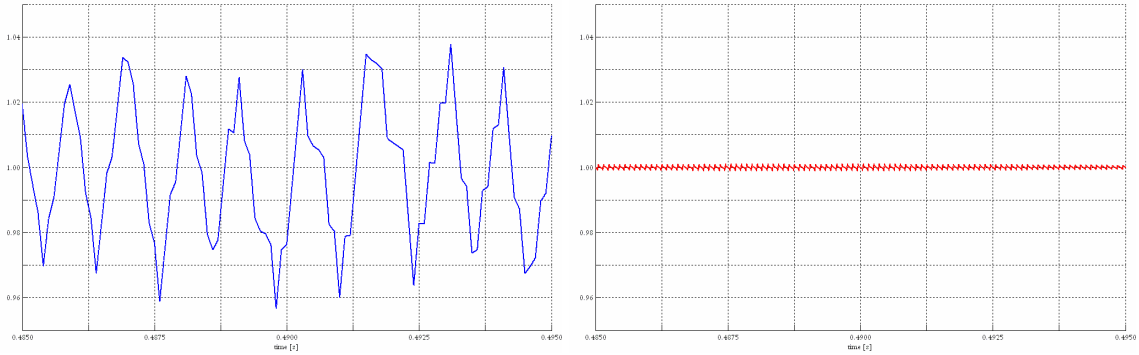

Figure IV.18. Stator flux vector magnitude at low speed operation (in p.u., $\Lambda^* = 0.85$ Wb): traditional DTC (in on the left) and predictive DTC (on the right).

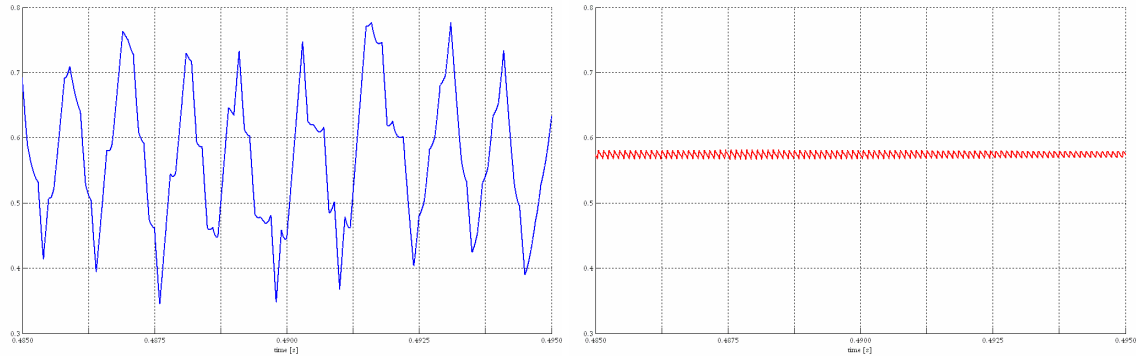

Figure IV.19. Stator current vector magnitude at low speed operation (in p.u., $\Im^* = 20$ A): traditional DTC (on the left) and predictive DTC (on the right).

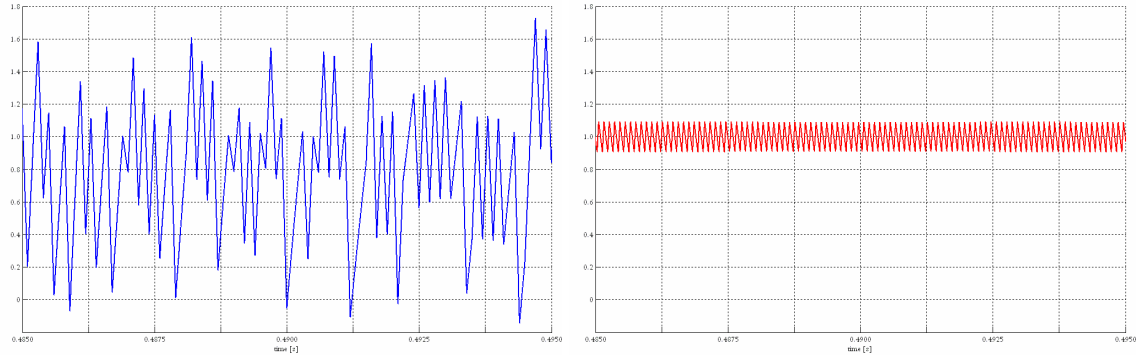

Figure IV.20. Torque responses at low speed operation (in p.u., $T_e^* = 6$ Nm): traditional DTC (on the left) and predictive DTC (on the right).

This is well highlights from Fig. IV.18 through Fig. IV.20, which are all referred to the low steady state speed operation. As a consequence, the torque mean value achieved by the traditional DTC algorithm is smaller than the reference one, whereas this drawback does not occur by employing the predictive DTC algorithm proposed.

After 0.5 s, the reference torque value is increased from 6 Nm to 18 Nm in order to achieve the higher steady state speed value of 90 rad/s. The corresponding simulation results are shown from Fig. IV.21 through IV.26.

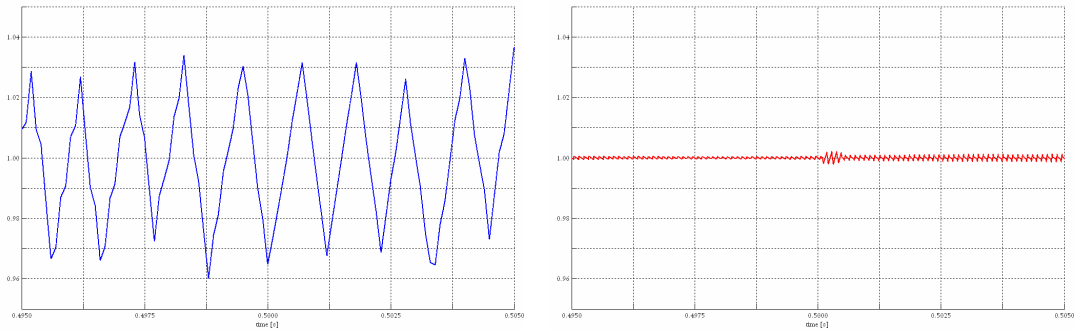

Figure IV.21. Stator flux vector magnitude responses during torque transient (in p.u., $\Lambda^* = 0.85$ Wb): traditional DTC (on the left) and predictive DTC (on the right).

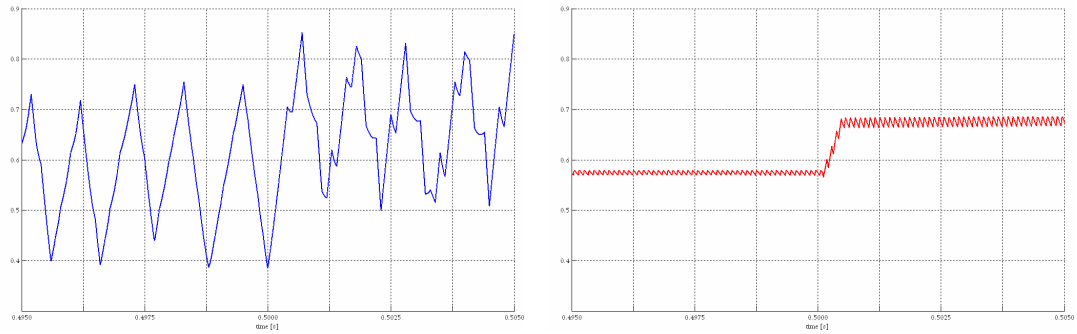

Figure IV.22. Stator current vector magnitude responses during torque transient (in p.u., $\Im^* = 20$ A): traditional DTC (on the left) and predictive DTC (on the right).

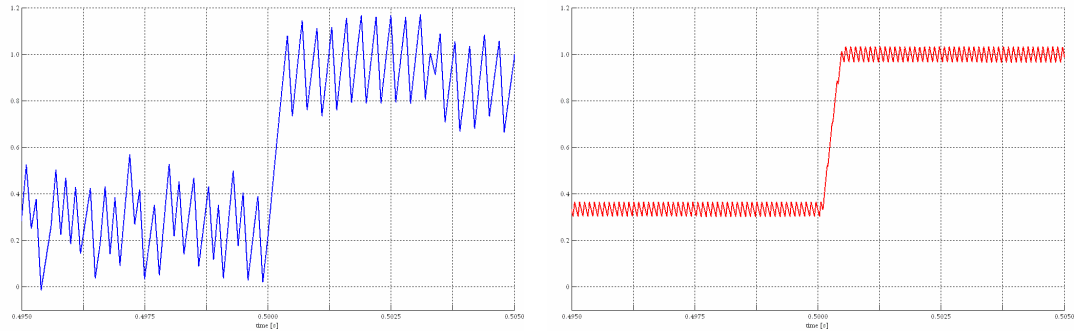

Figure IV.23. Torque responses (in p.u., $T_e^* = 18$ Nm): traditional DTC (on the left) and predictive DTC (on the right).

Referring to the traditional DTC, the torque mean value reduction still occurs, although the variables ripple becomes smaller than that achieved at low speed operation. However, it is still higher than that obtained by the predictive DTC algorithm proposed.

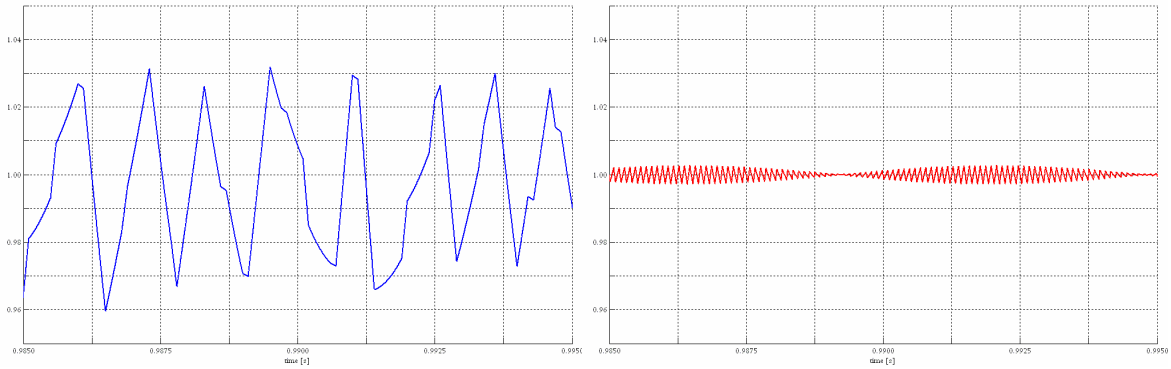

Figure IV.24. Stator flux vector magnitude at high speed operation (in p.u., $\Lambda^* = 0.85$ Wb): traditional DTC (on the left) and predictive DTC (on the right).

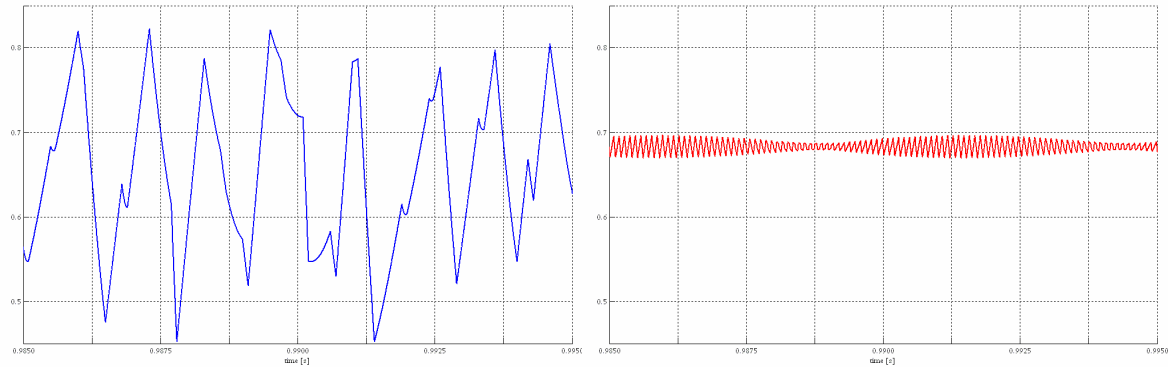

Figure IV.25. Stator current vector magnitude at high speed operation (in p.u., $\mathcal{I}^* = 20$ A): traditional DTC (on the left) and predictive DTC (on the right).

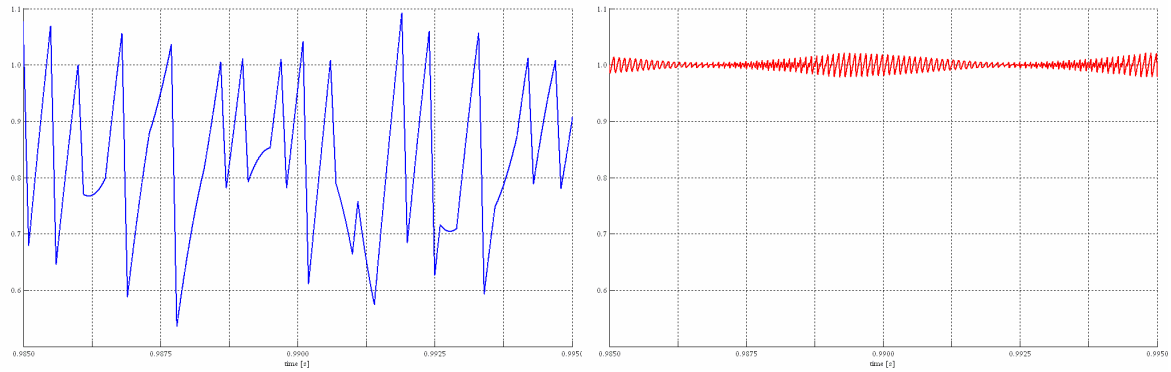

Figure IV.26. Torque responses at high speed operation (in p.u., $T_e^* = 18$ Nm): traditional DTC (on the left) and predictive DTC (on the right).

After 1 s, the torque inversion is performed from 18 Nm to -18 Nm. The corresponding simulation results, depicted from Fig. IV.27 through Fig. IV.29, highlight the better performance obtainable by the proposed predictive DTC algorithm again.

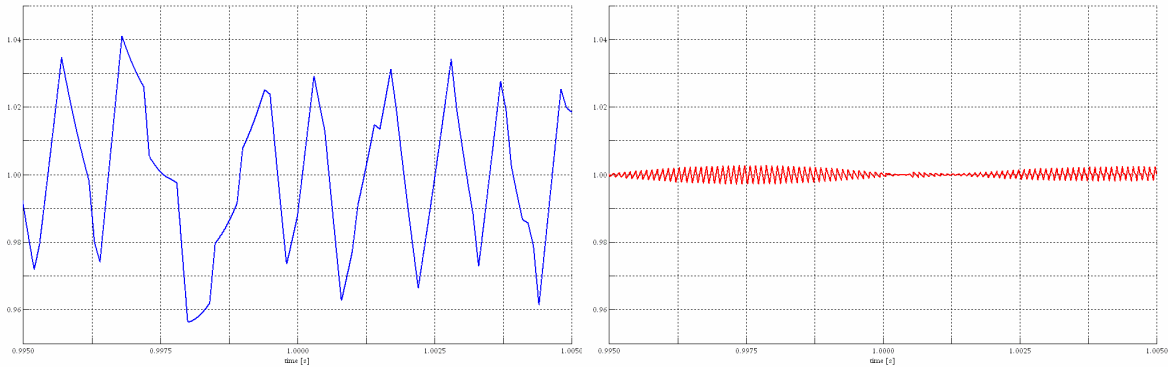

Figure IV.27. Stator flux vector magnitude responses during torque inversion (in p.u., $\Lambda^* = 0.85$ Wb): traditional DTC (on the left) and predictive DTC (on the right).

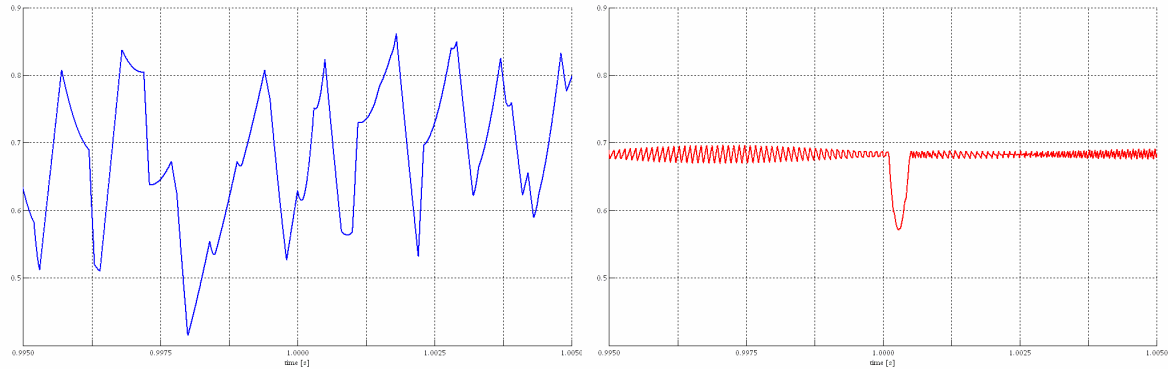

Figure IV.28. Stator current vector magnitude responses during torque inversion (in p.u., $\Im^* = 20$ A): traditional DTC (on the left) and predictive DTC (on the right).

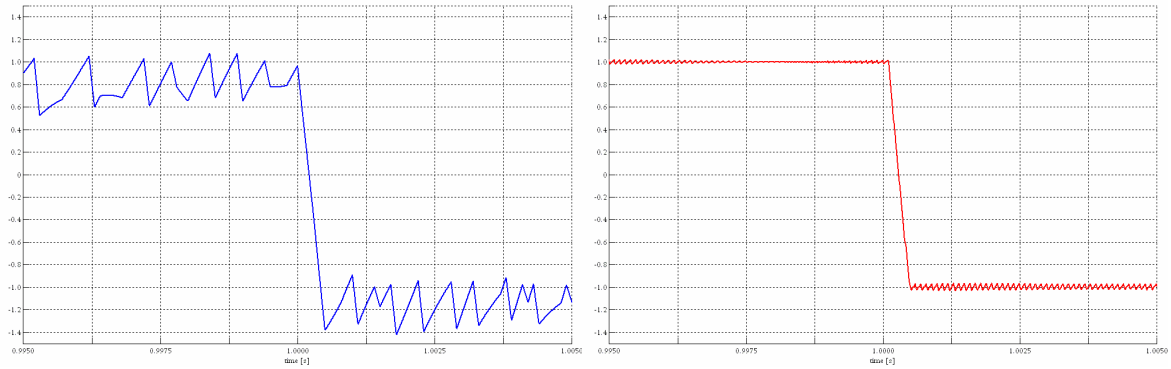

Figure IV.29. Torque inversions (in p.u., $T_e^* = 18$ Nm): traditional DTC (on the left) and predictive DTC (on the right).

In conclusion, the flux evolutions referred to all the simulation time of 1.5 s are shown in Fig. IV.30, whereas the rotor speed responses are depicted in Fig. IV.31. It can be seen that, applying the predictive DTC algorithm, it is possible to reach steady state speed values higher than those obtainable by the traditional DTC. This is due to the lower ripple and no mean torque value reduction which both characterizing the employment of the predictive DTC algorithm proposed.

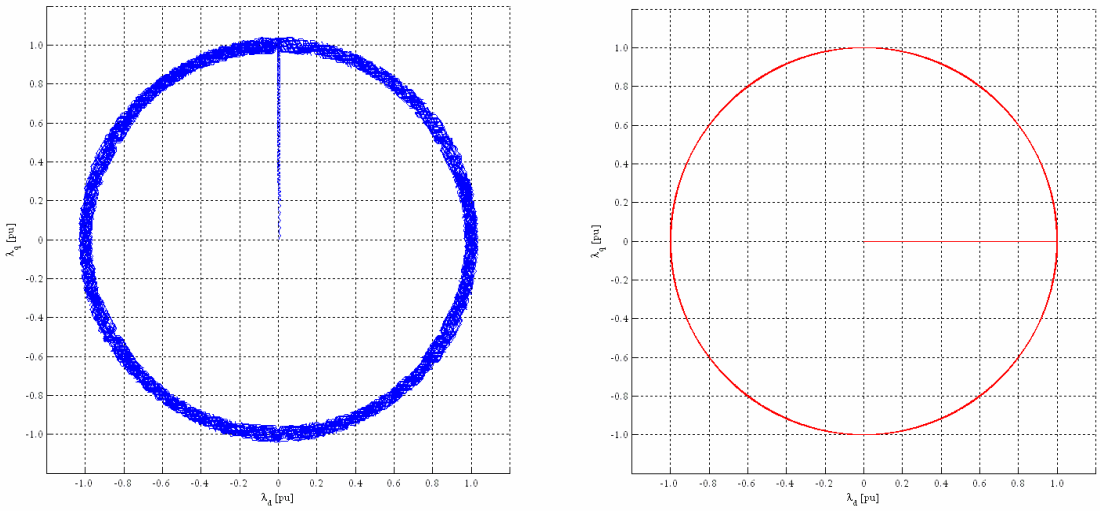

Figure IV.30. Stator Flux polar graphs (in p.u., $\Lambda^* = 0.85$ Wb): traditional DTC (on the left) and predictive DTC (on the right.

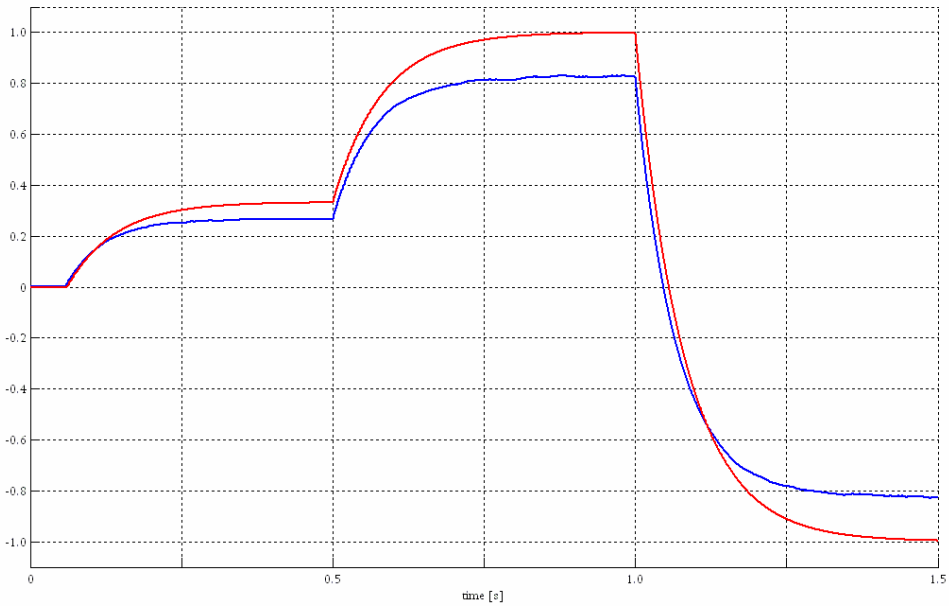

Figure IV.31. Speed responses (in p.u., $\omega_m^* = 90$ rad/s): traditional DTC (in blue) and predictive DTC (in red).

CONCLUSIONS

In this work, the application of the Predictive Control Technique (PCT) to the electrical drives has been considered and discussed, especially in comparison with the employment of the traditional control techniques. In particular, several predictive algorithms have been developed and applied to control different kinds of electrical drive (Brushless DC, Synchronous Reluctance and Asynchronous drive), with the aim of improving their performances. The effectiveness of all the proposed algorithms has been properly tested by appropriate simulation studies, performed in the Matlab Simulink environment. The corresponding results have highlighted how the employment of the PCT allows better performances compared to those achievable by the traditional control techniques.

However, the PCT is characterized by some drawbacks, such as its low robustness against parameters variations. In fact, all the predictive algorithms are based upon the discrete time model of the drive, which is employed in order to successfully computed the voltage pulse widths vector. So, if parameters variations occur, the effectiveness of the predictive control algorithms cannot be assured further. In order to avoid this, some solutions can be adopted; one of them consists in employing more rigorous mathematical model of the controlled system, as carried out for the SRM by taking into account the magnetic saturation phenomena. However, since this last solution cannot always be performed, predictive adaptive algorithms should be employed in order to periodically update the parameters values: this last solution should guarantee the quickly convergence of the estimated parameters values to those of the drive. Obviously, this can be done by means of a high computational cost of the predictive control algorithms, which is already quite higher compared to that of the traditional ones. Anyway, this last drawback can be overcome by employing very fast processor units, like FPGA (Field Programmable Gate Array), or introducing predictive observers in order to postpone the application of the input signals to the next sampling time intervals, as pointed out in this work.

REFERENCES

[1] A. Kawamura, R. Churayapratip, T. Haneyoshi: *"Deadbeat control of PWM inverter with modified pulse patterns for uninterruptible power supply"*, IEEE Transactions on Industrial Electronics, May 1988, Vol. 35, Issue 2, pp. 295 – 300.

[2] R. Carlson, M. Lajoie-Mazenc, J.C. dos S. Fagundes: *"Analysis of torque ripple due to phase commutation in brushless DC machines",* IEEE Transactions on Industry Applications, May-June 1992, Volume 28, Issue 3, pp. 632 – 638.

[3] J. Cros, J.M. Vinassa, S. Clenet, S. Astier, M. Lajoie-Mazenc: *"A novel current control strategy in trapezoidal EMF actuators to minimize torque ripples due to phases commutations"*, Fifth European Conference on Power Electronics and Applications, Brighton (UK), September 13-16 1993, vol. 4, pp. 266 – 271.

[4] Joong-Ho Song, Ick Choy: *"Commutation torque ripple reduction in brushless DC motor drives using a single DC current sensor"*, IEEE Transactions on Power Electronics, March 2004, Volume 19, Issue 2, pp. 312 – 319.

[5] Byoung-Hee Kang, Choel-Ju Kim, Hyung-Su Mok, Gyu-Ha Choe: *"Analysis of torque ripple in BLDC motor with commutation time"*, IEEE International Symposium on Industrial Electronics – ISIE 2001, June 12-16 2001, Volume 2, pp. 1044 – 1048.

[6] S. Bobbio, A. Del Pizzo, F. Marignetti, E. Pagano: *"Eddy current iron losses in axially laminated brushless motors"*, IEE Proceedings – Electric Power Applications, May 1995, Volume 142, Issue 3, pp. 183 – 190.

[7] A. Fratta, A. Vagati: *"A reluctance motor drive for high dynamic performances applications"*, IEEE Transaction on Industry Applications, July-Aug. 1992, Volume 28, Issue 4, pp. 873 – 879.

[8] T. Matsuo, T.A. Lipo: *"Rotor design optimization of synchronous reluctance machines"*, IEEE Transaction on Energy Conversion, June 1994, Volume 9, Issue 2, pp. 359 – 365.

[9] I. Boldea: *"Reluctance Synchronous Machines and Drives"*, Oxford Univ. Press, London (UK), 1996.

[10] T. Matsuo, T.A. Lipo: *"Field oriented control of synchronous reluctance machine"*, The 24th Annual IEEE Power Electronics Specialists Conference – PESC '93 Record, June 20-24 1993, pp. 425 – 431.

[11] M. Pacas, R. Morales: *"A predictive torque control for the synchronous reluctance machine taking into account the magnetic cross saturation"*, The 31st Annual Conference of IEEE Industrial Electronics Society – IECON 2005, Nov. 6-10 2005, pp.1419 – 1424.

[12] T. Yokoyama, M. Horiuchi, S. Shimogata: *"Instantaneous deadbeat control for PWM inverter using FPGA based hardware controller"*, The 29th Annual

Conference of the IEEE Industrial Electronics Society – IECON '03, Nov. 2-6 2003, Volume 1, pp. 180 – 185.

[13] S. Yamamoto, T. Ara, K. Matsuse: *"A Method to Calculate Transient Characteristics of Synchronous Reluctance Motors Considering Iron Loss and Cross-Magnetic Saturation"*, IEEE Transactions on Industry Applications, Jan.-Feb. 2007, Volume 43, Issue 1, pp. 47 – 56.

[14] I. Takahashi, T. Noguchi: *"A New Quick Response and High efficiency Control Strategy of an Induction Motor"*, IEEE Transaction on Industry Applications, Sept.-Oct. 1986, Vol. 22, Issue 5, pp. 820 – 827.

[15] M. Depenbrock: *"Direct self-control (DSC) of inverter-fed induction machine"*, IEEE Transactions on Power Electronics, Oct. 1988, Vol. 3, Issue 4, pp. 420 – 429.

[16] A. Damiano, G. Gatto, I. Marongiu, A. Perfetto: *"An Improved Look-up Table for Zero Speed control in DTC Drives"*, Proceedings of the 8th European Conference on Power Electronics and Applications – EPE '99, Lausanne (Switzerland), Sept. 7-9 1999.

[17] T.G. Habetler, F. Profumo, M. Pastorelli, L.M. Tolbert: *"Direct torque control of induction machines using space vector modulation"*, IEEE Transactions on Industry Applications, Sept-Oct. 1992, Vol. 28, Issue 5, pp. 1045 – 1053.

[18] C. Attaianese, A. Damiano, I. Marongiu, A. Perfetto, G. Tomasso: *"Direct Torque and Flux Control of Induction Motor Drives"*, Proceedings of the Second International Conference on Power Electronics and Drive Systems – IEEE PEDS '97, Singapore, May 26-29 1997, vol. 2, pp. 642 – 648.

[19] G. Buja, D. Casadei, G. Serra: *"Direct stator flux and torque control of an induction motor: theoretical analysis and experimental results"*, Proceedings of the 24th Annual Conference of the IEEE Industrial Electronics Society – IECON '98, Aachen (Germany), Aug. 31-Sept. 4 1998, Vol. 1, pp. T50 – T64.

[20] D. Casadei, G. Serra, A. Tani: *"Improvement of direct torque control performance by using a discrete SVM technique"*, The 29th Annual IEEE Power Electronics Specialists Conference – PESC '98 Record, May 17-22 1998, Vol. 2, pp. 997-1003.

[21] B.H. Kenny, R.D. Lorenz: *"Stator and rotor flux based deadbeat direct torque control of induction machines"*, The 2001 IEEE Industry Applications Conference – The 36th IAS Annual Meeting, Sept. 30-Oct. 4 2001, Vol. 1, pp. 133 – 139.

PUBLICATIONS

1. G. Gatto, I. Marongiu, A. Perfetto, A. Serpi: *"Performance Improvement of Brushless DC Motor Drive Controlled by a Predictive Algorithm"*, The 18th International Symposium on Power Electronics, Electrical Drives, Automation and Motion – SPEEDAM 2006, Taormina - CT (Italy), May 23–26 2006, pp. 1034-1038.
2. G. Gatto, I. Marongiu, A. Perfetto, A. Serpi: *"Three-Phase Operation of Brushless DC Motor Drive Controlled by a Predictive Algorithm"*, The 32nd Annual Conference of the IEEE Industrial Electronics Society – IECON 2006, Paris (France), November 7–10 2006, pp. 1166-1170.
3. G. Gatto, I. Marongiu, A. Perfetto, A. Serpi: *"Predictive Control of Synchronous Reluctance Motor Drive"*, IEEE International Symposium on Industrial Electronics – ISIE 2007, Vigo (Spain), June 4–7 2007, pp. 1147-1152.
4. G. Gatto, I. Marongiu, A. Perfetto, A. Serpi: *"A Predictive Optimal Torque Control of Synchronous Reluctance Motor Drive"*, The 10th International Workshop on Advanced Motion Control – AMC '08, Trento (Italy), March 26-28 2008, pp. 382-386.
5. G. Gatto, I. Marongiu, A. Perfetto, A. Serpi: *"A Predictive Direct Torque Control of Induction Machines"*, The 19th International Symposium on Power Electronics, Electrical Drives, Automation and Motion – SPEEDAM 2008, Ischia (Italy), June 11-13 2008, pp. 1103-1108.
6. G. Gatto, I. Marongiu, A. Perfetto, A. Serpi: *"Optimal Torque Control of Synchronous Reluctance Motor Drive by Predictive Algorithm"*, The 39th IEEE Power Electronics Specialists Conference – PESC08, Rhodes (Greece), June 15-19 2008, pp. 844-850.